Mn DOPED $(Cu_{0.5}Tl_{0.5})$ $Ba_2Ca_2Cu_3O_{10-\delta}$ SUPERCONDUCTORS

A dissertation submitted to the department of physics, Quaid-i-Azam University Islamabad, in the partial fulfillment of the requirement for the degree of

Master of Philosophy

In

Physics

By

QURAT-UL-AIN

Department of Physics
Quaid-i-Azam University
Islamabad, Pakistan.
©2009-2011

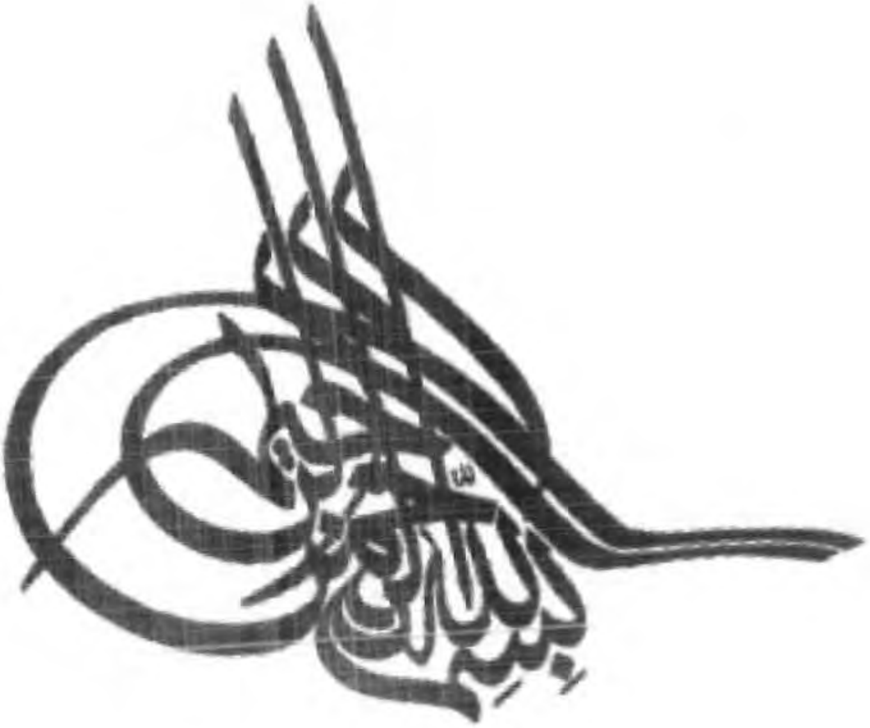

Certificate

This is to certify that Ms. Qurat-ul-Ain has carried out the experimental work in this dissertation under my supervision in Materials Science Laboratory and is accepted in its present form by the Department of Physics, Quaid-i-Azam University Islamabad as satisfying the dissertation requirement for the degree of Master of Philosophy in Physics

Supervisor

2-2-2011

Dr. Nawazish Ali Khan
Department of Physics
Quaid-I-Azam University
Islamabad, Pakistan

Submitted through

Hasanain

Chairman
Prof. Dr. S.K. Hasanain
Department of Physics
Quaid-I-Azam University
Islamabad, Pakistan

DEDICATED TO MY AMA

ABA JEE

ACKNOWLEDGEMENTS

It gives me great pleasure and satisfaction to acknowledge the endowment of the creator of the universe, Allah Almighty, the most gracious, compassionate and beneficent to His creature, who enabled me to complete my research work successfully. I offer my humblest and sincere words of thanks to The Holy Prophet Muhammad (P.B.U.H) who is forever a source of guidance and knowledge for humanity.

This work would have not been possible without the invaluable contributions of many individuals. First and foremost, I wish to thank my reverend supervisor *Assistant Prof.* Dr. Nawazish Ali Khan for all of his support, advice, and guidance during the whole period of my study.

I am thankful to chairman, department of physics, for the provision of all possible facilities and full cooperation. I would like to pay lots of appreciations to all my teachers who blessed me with knowledge and guidance.

I am indebted to my many colleagues who supported me and working with them has truly been a delight. I owe my deepest gratitude to Rehan Safdar for his help and support.

This thesis is dedicated to my parents, who have given me the opportunity of an education from the best institutions and support throughout my life. My sincerest gratitude to them and to my siblings' noor, zoha, abdulrahman, zia-ur-rahman for all they have done. I could not wish for a more supportive, loving family.

Last but not least I am also thankful to all my friends' sobia, sana, sadia, humaira who encouraged me during research work and thesis writing

Quratulain
QURAT-UL-AIN

Abstract

Mn-doped $Cu_{0.5}Tl_{0.5}Ba_2(Ca_{2-y}Mn_y)Cu_3O_{10-\delta}$ (y=0, 0.15, 0.25, 0.35, 0.5, 0.75, 1.0) samples synthesized at room temperature employing solid state reaction method and their superconducting properties are studied. In these experiments, it is expected that the multiple oxidation states of doped Mn (more than +2) at the Ca site would enhance the inter-plane coupling and enhance the magnitude the superconductivity. Contrary to our expectation, the $T_c(R=0)$ and magnitude of superconductivity are systematically suppressed with increased Mn-doping. The suppression of superconductivity is explained in terms of decreased density of mobile carriers associated with possible localization of the carriers at the Mn sites. It is most likely that the suppressed density of the mobile carriers in the conducting CuO_2 plane may increase the anti-ferromagnetic alignment of the spins of Cu atoms which decrease the magnitude of superconductivity. The doping of Mn at the intrinsic sites of the unit cell is verified by Fourier Transform Infrared Spectroscopy (FTIR) measurements. From the FTIR absorption measurements it observed that the CuO_2 planar oxygen mode is hardened whereas the apical oxygen mode of $Cu(1)-O_A-Cu(2)$ is softened with increased Mn-doping. The optimization of the carriers in the conducting CuO_2 planes is brought about by carrying out self-doping experiments in oxygen atmosphere. After-post annealing in oxygen, the $Cu(1)-O_A-Cu(2)$ mode is softened with increased Mn-doping, which lead us to believe that doped Mn atoms alter the charge state of Cu atoms and hence possibly the spin alignment of Cu atoms in the CuO_2 planes.

Contents

1. Introduction to superconductors

2. Literature Review

3. Experimental Techniques

4. RESULTS AND DISCUSSION

List of Figures

INTRODUCTION TO SUPERCONDUTORS

1.1 Superconductivity:

Superconductivity is a phenomenon in which some materials lose all electrical resistance at very low temperatures. For example if Lead is gradually cooled its resistance steadily decreases (this is common for most conductors). But if cooled below 7.2 degrees Kelvin, its resistance suddenly drops to zero. In this state a ring made of lead is able to conduct a current that cycles for years (creating magnetic fields) without any observed decay. Perfect superconductor is a material which exhibit two characteristic properties as shown in figure 1.1

(a) Vanishing of electrical resistivity below a critical temperature (T_c)

(b) Expulsion of magnetic flux blow a critical field (H_c)

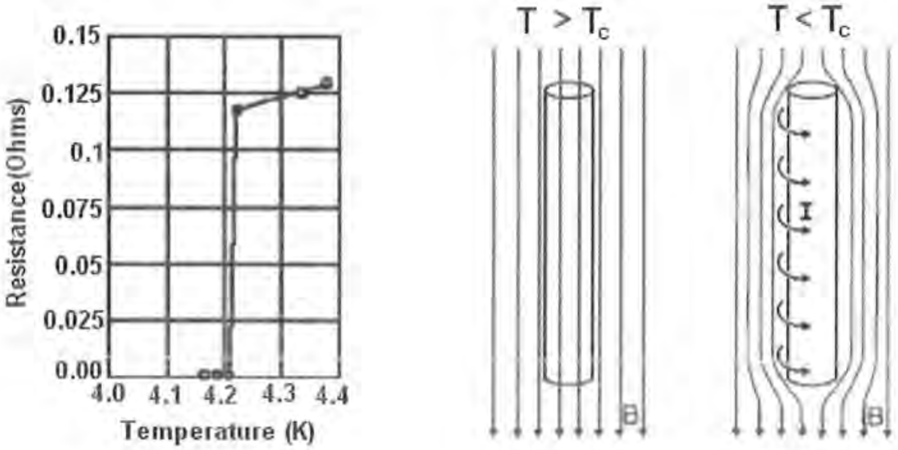

(a) Vanishing resistance

(b) Meissner effect

Fig.1.1: (a) Vanishing of electrical resistivity and (b) Meissner effect.

At higher temperatures it is normal metal and ordinary and is not a very good conductor for example lead, tin became superconductor while copper, silver which are much better conductors do not superconduct.

1.2 Brief History:

In 1908, H. kamerlingh Onnes initiated the field of low temperature physics by liquefying helium in his laboratory at Leiden. Three years later he found that below 4.15K the dc resistance of mercury dropped to zero (Onnes, 1911) [1]. With that finding the field of superconductivity was born. The next year Onnes discovered that the application of the sufficiently strong axial magnetic field restored the resistance to its normal value. One year later, in 1913, the element lead was found to be superconducting at 7.2K (Onnes,

1913) [2]. Another 17 years were to pass before this record was surpassed, by the element niobium ($T_{c} = 9.2K$).

A considerable amount of time went by before physicists became aware of the second distinguishing characteristic of a superconductor namely, its perfect diamagnetism. In 1933, Meissner and Ochsenfeld found that when a sphere is cooled below its transition temperature in a magnetic field, it excludes the magnetic flux. The report of the Meissner effect led the London brothers, Fritz and Heinz, to propose equations that explain this effect and predicts how far a static external magnetic field can penetrate in to a superconductor. The next theoretical advancement came in 1950 with the theory of Ginzburg and Landau which describes superconductivity in terms of an order parameter and provided a deviation from the London equations. Both of these theories are macroscopic in character.

In the same year it was predicted theoretically by H. Frohlich (1950) that the transition temperature would decrease as the average isotropic mass increases. This effect called the isotope effect was observed experimentally the same year. The isotope effect provided support for the electron-phonon interaction mechanism of superconductivity. Our present theoretical understanding of the nature of superconductivity is based on the BCS microscopic theory proposed by J. Bardeen, L. Cooper, and J. R. Schrieffer in 1957 [3]. In this theory it is assumed that bound electron pairs that carry the super-current are formed and that an energy gap between the normal and superconductive states is created. The Ginzburg- Landau (1950) and London (1950) theories fit well into the BCS formalism. Much of the present theoretical debate centers on how well the BCS theory explains the properties of new high temperature superconductors.

Alloys and compounds have been extensively studied, especially the so-called A15 compounds, such as Nb_3Sn, Nb_3Ga, and Nb_3Ge, which held the record of the highest transition temperature from 1954 to 1986. Many other type of compounds have been studied in recent years particularly the so called heavy fermions system. Organic superconductors have shown a dramatic rise in transition temperatures during the past decade.

On April 17, 1986, a brief article, entitled "possible high T_c superconductor in the Ba-La-Cu-O system", written by J. G. Bednorz and K. A. Muller initiating the new era of high temperature superconductivity.

When the article appeared in print later that year, it met with initial skepticism. Sharp drop in resistance attributed to "high T_c" superconductor had appeared from time to time over the years, but when examined they had always failed to show the required diamagnetic response or were otherwise unsubstantiated. It was only when a Japanese group [4] and Chu's group in the United States [5] reproduced the original results that the results found by Bednorz and Muller began to be taken seriously. Soon many of the researchers became active, and the recorded transition temperature begins to rise.

By the beginning of 1987, scientist had fabricated the Lanthanum compound, which went superconducting close to 40K at atmospheric pressure [6] and at up to 52K under high pressure [7]. Soon thereafter, the Yttrium-barium system, which went superconducting around 90K was discovered. In early 1988, the superconductivity with $T_c(R=0)$ around 110K was achieved with the discovery of BiSrCaCuO system and with $T_c(R=0)$ around 120-125K in TlBaCaCuO system. This rapid pace of change and improvement in superconductor's transition temperature is plotted in Fig.1.2. For 56 years the element niobium and its compounds had dominated the field of superconductivity. Not only providing the highest Tc values, niobium compounds such as NbTi and Nb_3Sn are also optimal magnet materials: for NbTi, H_{c2} = 10T and for Nb_3Sn H_{c2} = 22T at 4.2K, where H_{c2} is the upper critical field of a type II superconductors, in the sense that it sets a limit on the magnetic field attainable by the magnet. Thus applications of an applied magnetic field in excess of Hc_2 drive a superconductor normal. The period from 1930 to 1986 can be called the Niobium Era of superconductivity. The new period that began in 1986 becomes the Copper Oxide Era because the presence of copper and oxygen has, with rare expectations, been found essential for T_c above 40K. It is also interesting to observe that Hg was the first known superconductor, and now century later mercury compounds have become the best.

In the spring of 2008, a new fascinating family of superconductors came into focus containing an iron pnictide/chalcogenide layer of anti-PbO structure as the superconducting component, so far with transition temperatures up to about 50K.

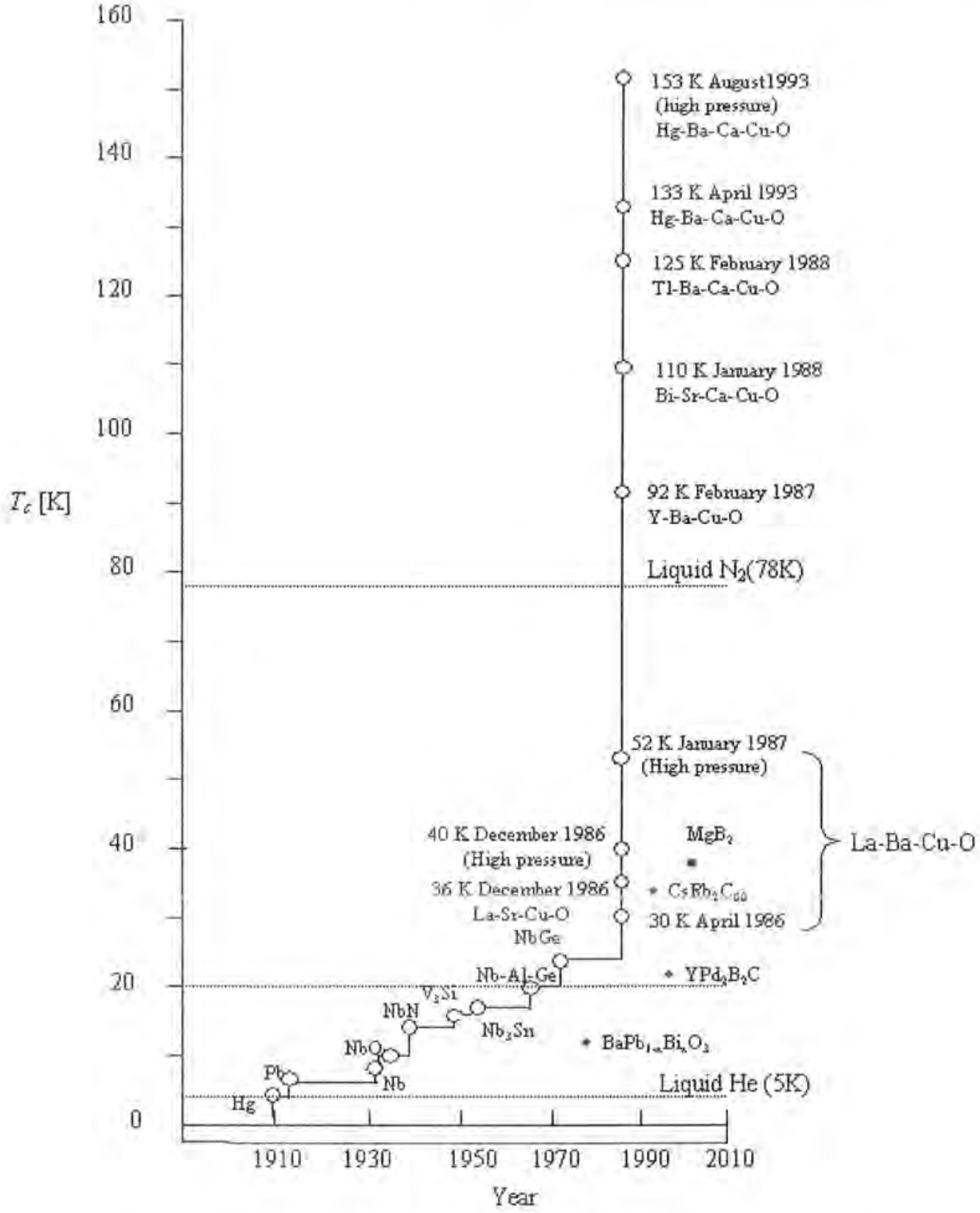

Fig. 1.2: Increase of the transition temperature over the years.

1.3 Basic Concept:

The electrical resistivity of all metals and ceramic materials decreases when they are cooled. To understand it, one must know about the possible source of resistance in a conductor [8].

The current in a conductor is carried by conduction electrons which are free to move through the material. Electrons have a wave like nature and while traveling through a metal can be represented by a plane wave progressing in the direction of motion. A conductor (such as metal) has a crystalline structure with the atoms lying on a regular repetitive lattice sites, and it is a property of a plane wave that it can pass through a perfectly periodic structure without being scattered into other directions. In other words, if a current passed through a perfect crystal it will experience no resistance.

However, any fault in a periodicity of the crystal will scatter the electron wave and introduce some resistance. There are two effects which can introduce some resistance. First is a lattice vibration in which atoms are vibrating about their equilibrium position. The second effect is unintentional introduction of defects in compound during growth of material. Both the thermal vibration and imperfection scatter the moving conduction electron and give rise to electrical resistance.

For perfectly pure metal, where the electron's motion is impeded only by the thermal vibration of the lattice, the resistivity should approach to zero as the temperature is reduced towards zero Kelvin. Any real specimen of metal cannot be perfectly pure and will contain some impurities. Therefore, the electrons not only being scattered by thermal vibrations of the lattice atoms but are also scattered by impurities and the impurities scattering is more or less independent of temperature. As a result there is a certain "residual resistivity" (Fig 1.3) that remains even at the lowest temperatures. The more the metal, the larger be its residual resistivity.

Certain metals, however, show a very remarkable behavior, when they are cooled their electrical resistance decreases in a usual way, but on reaching a temperature few degrees above zero they suddenly lose their electrical resistance. They are then said to be in superconducting state.

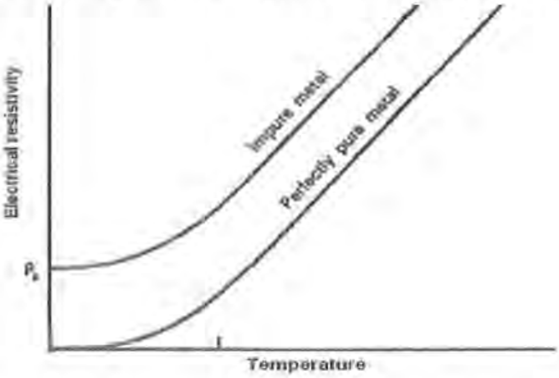

Fig. 1.3: Variation of electrical resistivity of metals with temperature.

The magnetic properties of a superconductor are as dramatic as their electrical properties. When a superconductor is placed inside a magnetic field and then cooled through the transition temperature, the field will be completely pushed out from the material. In other words, the material becomes fully diamagnetic in superconducting state. This is called the Meissner effect and was found to be an intrinsic property of superconductors. It has been widely used for testing the superconducting state [9].

1.4 (CuTl) Based Superconductors:

Since the discovery of superconductivity in both $CuBa_2Ca_nCu_{n+1}$ and $TlBa_2Ca_nCu_{n+1}$ systems, such as Cu-12n(n+1) and Tl-12n(n+1) systems, their extensive characterization have been carried out. Both of these systems are iso-structural except the position of oxygen in the charge reservoir layer. Optimizing the carrier concentration could enhance the superconducting properties of these compounds. The carrier concentration could be control by cation substitution, by varying oxygen contents and by applying external pressure [10,11]. The substitution of Tl in Cu-12(*n*-1)*n* compounds results in emergence of a new subfamily $Cu_{1-x}Tl_x$-12(*n*-1)*n* which is close derivative of these compounds. These compounds are prepared under high as well as normal pressure and have superconducting properties very close to Cu-based compounds [12,13-16]. The members of this family have semi-insulating $Cu_{1-x}Tl_xBa_2O_{4-\delta}$ charge reservoir layer that slightly increases the anisotropy of these superconductors but the anisotropy remains lower than that of Tl-based compounds. A comparison of the anisotropy parameter and technological critical temperature for superconductors of different families is shown in Fig.1.4. The $Cu_{1-x}Tl_xBa_2Ca_2Cu_3O_{10-\delta}$ ($Cu_{1-x}Tl_x$-1223) superconductor of this family has highest critical temperature [T_c (R=0) =130K] and higher critical current density [17]. This compound with anisotropy parameter around $\gamma=5$, has $Cu_{1-x}Tl_xBa_2O_{4-\delta}$ charge reservoir layer and three conducting CuO_2 planes in the unit cell as shown in the Fig.1.5 [18]. It follows P4/mmm space group and has tetragonal structure [19]. The two Ca atoms in the unit cell separate CuO_2 planes from each other. The superconducting CuO_2 plane connected with Ba atom, in the unit cell is pyramid type and is called p-plane. While a plane sandwiched between the p-planes is connected by Ca atoms with the outer-planes and is called central plane or s-plane. The p-planes are over-doped with the carriers while s-planes are optimally doped.

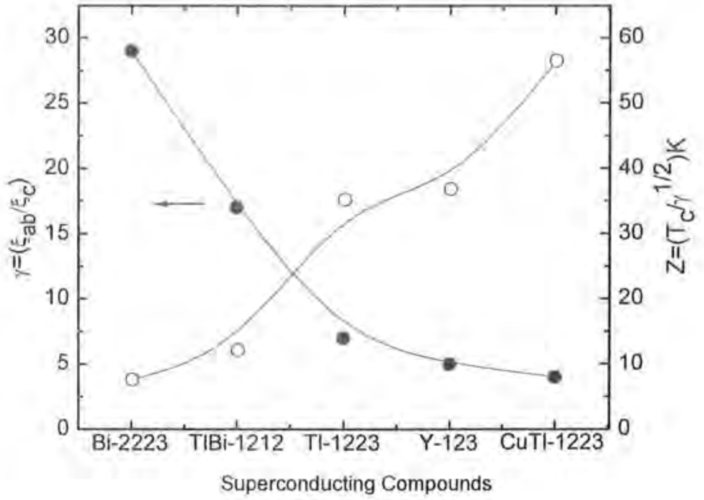

Fig. 1.4: Comparison of anisotropy and technological critical temperature of high temperature superconductors.

The p-planes also serve as a bridge for the supply of the carriers from charge reservoir layer to s-plane. The Cu atoms in the s-plane are named as Cu(2) and the oxygen atom in this plane is named as O(4). The oxygen atom bridging the $Cu_{1-x}Tl_xBa_2O_{4-\delta}$ charge reservoir layer and p-plane is apical oxygen atom and is named as O(2) atom. This atom practically controls the charge transport mechanism. The oxygen atom at the center of $Cu_{1-x}Tl_xBa_2O_{4-\delta}$ charge reservoir layer is named as O_3 atom or O_δ atom.

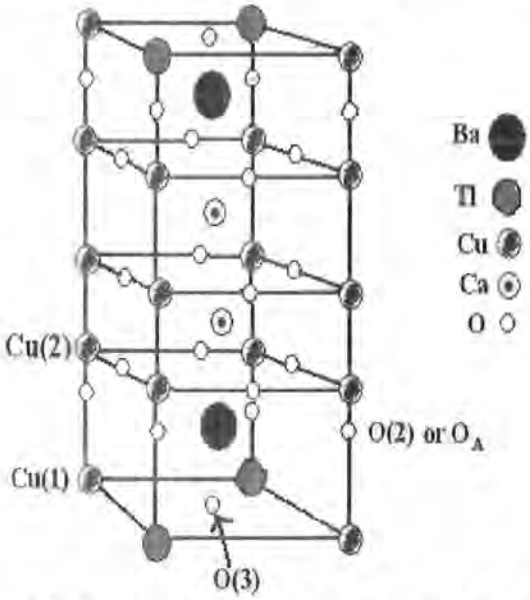

Fig 1.5: Crystal structure of CuTl-1223 unit cell.

1.5 BCS Theory:

In BCS theory of superconductivity, the mechanism of superconductivity is attributed to an attractive interaction between two electrons through electron-phonon interaction [20]. The attractive interaction between electrons can be understood in the following way: one electron interacts with a positive ion in the lattice and deforms the lattice whereas a second electron of compatible momentum value interacts with the ion in the distorted lattice so as to minimize the energy. The interacting electrons are said to form a pair. The electrons of a pair have equal and opposite momentum (i.e. one with +k and other with –k), with the one in spin up state and the other in spin down state, so that the total spin of a pair is zero. These electron pairs are called Cooper pairs. The size of a Cooper pair in a superconductor is known as the *coherence length* (ξ). The important feature of Cooper pairs is that excitation can take place in only pairs of electrons i.e. if the state with +k and spin up (↑) is occupied, the corresponding state with –k and spin down (↓) is also occupied and if the state of +k is vacant, the state of –k is also vacant.

The cooper pairs have net zero spin and are able to condense into quantum mechanical ground state with long range order. One consequence of this is the existence of small energy gap near Fermi surface E_F. The formation of cooper pairs results in the minimization of the total energy of the system and leads to a small energy gap Δ near the Fermi energy E_F. Most of the special characteristics of a superconductor can be understood as a consequence of the existence of this small energy gap [21].

1.6 Zero Resistivity:

In superconductors the resistivity, ρ becomes zero and so the conductivity σ appears to become infinite below Tc. To be consistent with the constitutive relation, Equation 1.1 must always have zero electric field,

$$\rho = 0 \qquad (1.1)$$

at all points inside a superconductor. In this way the current J can be finite. So we have current flow without electric field. The change from finite to zero resistivity at the superconducting critical temperature T_c is very sudden, as shown in Fig. 1.6.

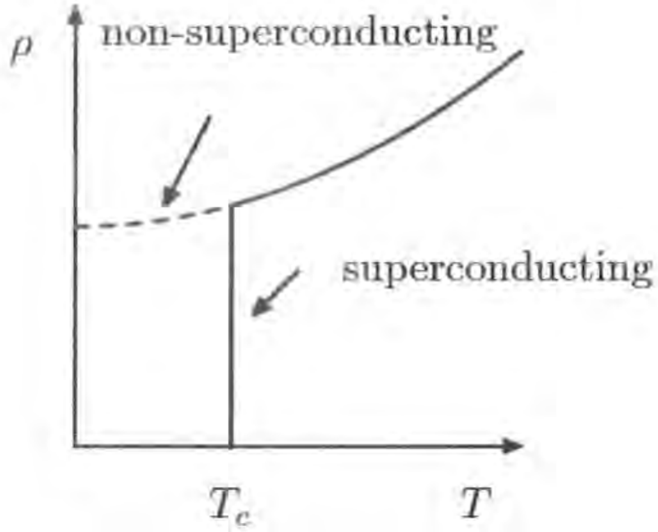

Fig. 1.6: Resistivity of a typical metal as a function of temperature. If it is a non-superconducting metal (such as copper or gold) the resistivity approaches a finite value at zero temperature, while for a superconductor (such as lead, or mercury) all signs of resistance disappear suddenly below a certain temperature, T_c.

This represents a thermodynamic phase transition from one state to another. As for other phase transitions, such as from liquid to gas, the properties of the phases on either side of the transition can be completely different. The change from one to the other occurs sharply at a fixed temperature rather than being a smooth cross-over from one type of behaviour to another. Here the two different phases are referred to as the "normal state" and the "superconducting state". In the normal state the resistivity and other properties behaves similarly to a normal metal, while in the superconducting state many physical properties including resistivity are quite different [22].

1.7 London Penetration Depth (λ):

In 1935, Fritz and Heinz London theoretically explained the Meissner effect by positing two groups of electrons in a superconducting material, the superconducting electrons and the normal state electrons. They employed the Maxwell equations to develop a set of electrodynamics equations, called the London equations [23]. According to the London equations, the magnetic field exponentially falls off with increasing distance from the surface of a superconducting sample. If B(0) is the field at the plane boundary, then field inside at any depth will be

$$B(x) = B(0) \exp(-x/\lambda_L) \qquad (1.2)$$

$$\lambda_L = (m_e / \mu_0 n_s e^2)^{1/2} \qquad (1.3)$$

where m_e and e is the mass and charge of electron respectively where n_s is the number density of super-electrons.

In short, London penetration depth is the distance inside the surface over which an external magnetic field is screened out to zero, given that B=0 in the bulk, and is approximately equal to 60 nm for n_s about 10^{22} cm $^{-3}$ [24].

1.8 Coherence Length (ξ):

Three physicists at the University of Illinois in Urbana John Bardeen, Leon Cooper and Robert Schrieffer presented a theoretical explanation for the superconducting state. This theory was widely accepted and is well known as the *BCS theory*. Based on this theory (despite the Coulomb repulsive forces between the electrons) due to distortion in the crystal structure (phonon mediation), a slight attraction between pair of electrons located near the Fermi surface leads to the production of bonded pair of electrons, called the Cooper pair [25]. The size of a Cooper pair in a superconductor is known as the coherence length (ξ)

$$\xi = \hbar v_f / \pi\Delta \qquad (1.4)$$

Where $2\Delta = E_g$ is the super conducting electron gap, and v_f is the Fermi velocity.

1.9 Meissner Effect:

In 1933, Walther Meissner and his student Robert Ochsenfeld discovered an important magnetic property of superconductors. They observed that a magnetic field lower than H_c was suddenly expelled by superconductor specimen on cooling below T_c. In other words, the material becomes fully diamagnetic in the superconducting state. This is called the *Meissner effect* and was found to be an intrinsic property of superconductors [26]. It has been widely used for the testing the superconducting state. Due to the Meissner effect, if an external magnetic field is applied to a sample which is in the superconducting state, an electric current is produced near the surface of sample, in such a way as to create a magnetic field that exactly cancels the external magnetic field.

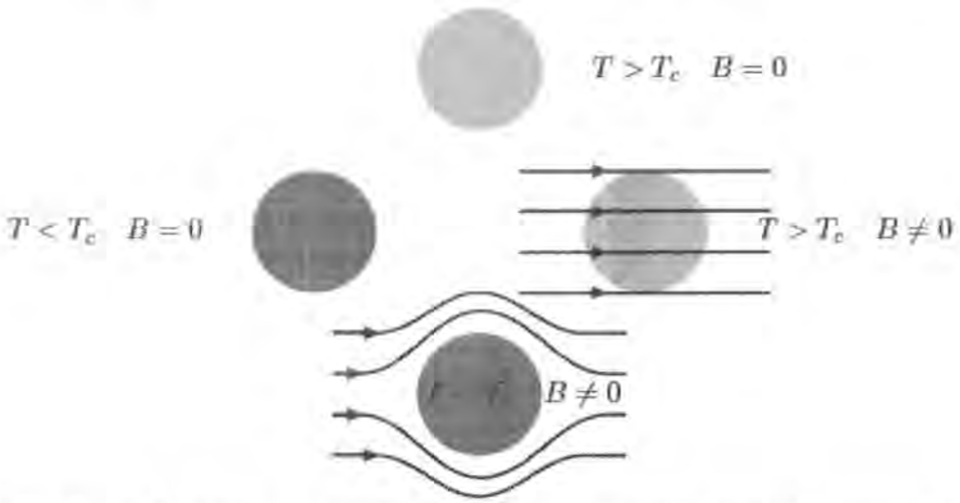

Fig. 1.7: The Meissner-Ochsenfeld effect in superconductors. If a sample initially at high temperature and in zero magnetic field (top) is first cooled (left) and then placed in a magnetic field (bottom), then the magnetic field cannot enter the material (bottom). This is a consequence of zero resistivity. On the other hand a normal sample (top) can be first placed in a magnetic field (right) and then cooled (bottom). In the case the magnetic field is expelled from the system.

1.10 Type I and Type II Superconductors:

As the field becomes stronger it turns out that either one of two possible things can happen. The first case, called a type I superconductor, is that the B field remains zero inside the superconductor until suddenly the superconductivity is destroyed. The field where this happens is called the critical field "H_c". The way the magnetization M changes with H in a type I superconductor is shown in Fig. 1.8a. As shown, the magnetization obeys

$$M = -H \qquad \text{(SI)} \qquad (1.5)$$

for all fields less than H_c, and then becomes zero (or very close to zero) for fields above H_c. Many superconductors behave differently [27]. In a type II superconductor there are two different critical fields, denoted "H_{c1}" the lower critical field, and "H_{c2}" the upper critical field. For small values of applied field H the Meissner-Ochsenfeld effect again leads to M = -H and there is no magnetic flux density inside the sample, B = 0. However, in a type II superconductor once the field exceeds H_{c1}, magnetic flux starts to enter the superconductor and hence $B \neq 0$.

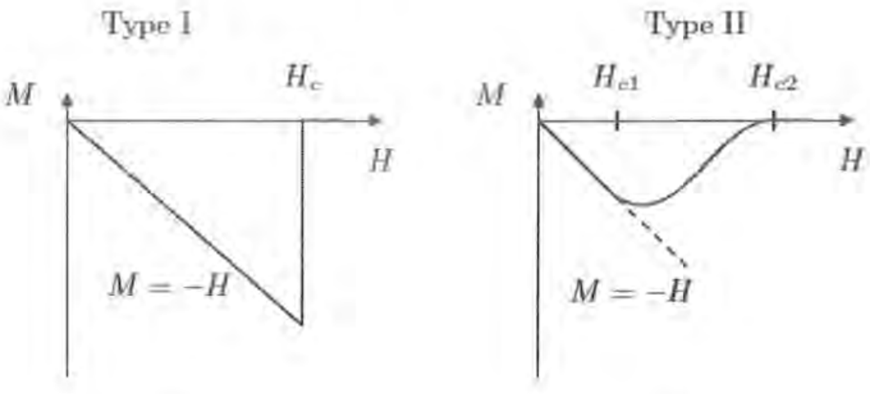

(a) (b)

Fig. 1.8: The magnetization M as a function of H in type I and type II superconductors. For type I perfect Meissner diamagnetism is continued until Hc, beyond which superconductivity is destroyed. For type II materials perfect diamagnetism occurs only below H_{c1}. Between H_{c1} and H_{c2} Abrikosov vortices enter the material, which is still superconducting.

Upon increasing the field H further the magnetic flux density gradually increases inside the superconductor until finally at H_{c2} the superconductivity is destroyed and M = 0. This behaviour is sketched in Fig. 1.8b. As a function of the temperature the critical fields vary, and they all approach zero at the critical temperature T_c. The typical phase diagrams of type I and type II superconductors, as a function of H and T are shown in Fig. 1.9.

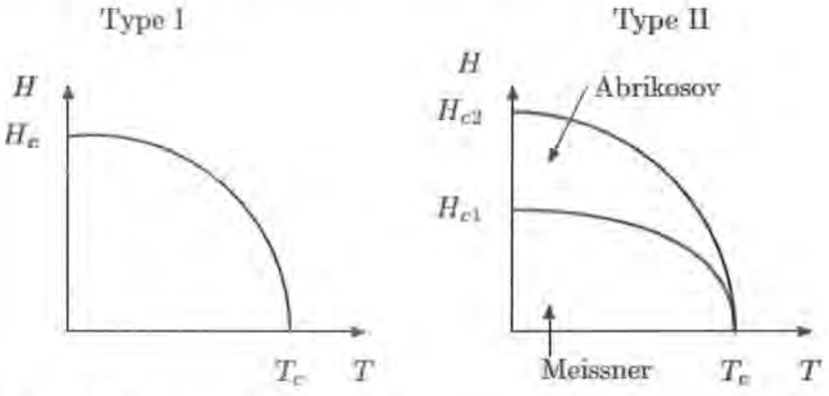

Fig. 1.9: The H - T phase diagram of type I and type II superconductors. In type II superconductors the phase below H_{c1} is normally denoted as the Meissner state, while the phase between H_{c1} and H_{c2} is the Abrikosov or mixed state.

The physical explanation of the thermodynamic phase between H_{c1} and H_{c2} was given by Abrikosov. He showed that the magnetic field can enter the superconductor in the form of vortices and each vortex consists of a region of circulating supercurrent around a small central core which has essentially become normal metal. The magnetic field is able to pass through the sample inside the vortex cores, and the circulating currents serves to screen out the magnetic field from the rest of the superconductor outside the vortex [22].

1.11 Important Factors For Superconducting State:

The superconducting state is defined by three very important factors: critical temperature (T_c), critical field (H_c), and critical current density (J_c). Each of these parameters is very dependant on the other two properties present. Maintaining the superconducting state requires that both the magnetic field and the current density as well as the temperature remain below the critical values, all of which depend on the intrinsic properties of a material. The phase diagram in Figure 1.10 demonstrates relationship between T_c, H_c, and J_c. The highest values for H_c and J_c occur at zero K, while the highest value for T_c occurs when H and J are zero. When considering all three parameters, the plot represents a critical surface. From this surface, and moving toward the origin, the material is superconducting. Regions outside this surface the material is normal or in a lossy mixed state. When electrons form Cooper pairs, they can share the same quantum wave-function or energy state.

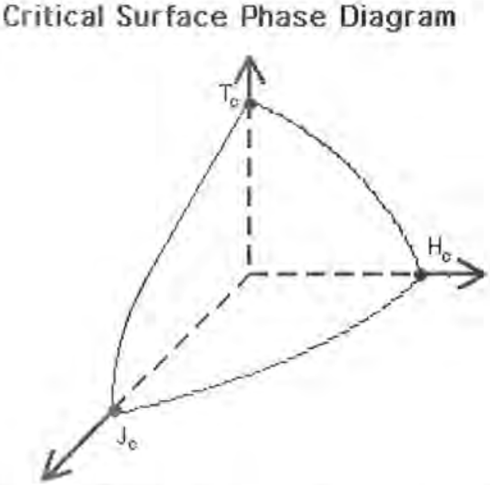

Fig. 1.10: The phase diagram in demonstrates relationship between T_c, H_c, and J_c.

This results in a lower energy state of the superconductor. T_c and H_c are values where it becomes favorable for the electron pairs to break apart. The current density larger than the critical value is forced to flow through normal material. This flow through normal material of the mixed state is connected with motion of magnetic field lines past pinning sites. For most practical applications, superconductors must be able to carry high currents and withstand high magnetic field without reverting to its normal state [28].

Higher H_c and J_c values depend upon two important parameters which influence energy minimization, penetration depth and coherence length. Penetration depth is the characteristic length of the fall off of a magnetic field due to surface currents. Coherence length is a measure of the shortest distance over which superconductivity may be established. The ratio of penetration depth to coherence length is known as the Ginzburg-Landau parameter. If this value is greater than 0.7, complete flux exclusion is no longer favorable and flux is allowed to penetrate the superconductor through cores known as vortices.

1.12 Uses Of Superconductors:

Magnetic-levitation is an application where superconductors perform extremely well. Transport vehicles such as trains can be made to "float" on strong superconducting magnets, virtually eliminating friction between the train and its tracks. Not only would conventional electromagnets waste much of the electrical energy as heat, they would have to be physically much larger than superconducting magnets. A landmark for the commercial use of MAGLEV technology occurred in 1990 when it gained the status of a nationally-funded project in Japan. In December 2003, the MLX01 test vehicle attained an incredible speed of 361mph (581kmph).

An area where superconductors can perform a life-saving function is in the field of biomagnetism. Doctors need a non-invasive means of determining what's going on inside the human body. By impinging a strong superconductor-derived magnetic field into the body, hydrogen atoms that exist in the body's water and fat molecules are forced to accept energy from the magnetic field. They then release this energy at a frequency that can be detected and displayed graphically by a computer. Magnetic Resonance Imaging (MRI) was actually discovered in the mid 1940's. But the first MRI examination on a human being was not performed until July 3, 1977. And it took almost five hours to produce one image. Today's faster computers process the data in much less time.

Probably the one event, more than any other, that has been responsible for putting "superconductors" into the American lexicon was the

Superconducting Super-Collider project planned for construction in Ellis County, Texas. Though Congress cancelled the multi-billion dollar effort in 1993, the concept of such a large, high-energy Collider would never have been viable without superconductors. High-energy particle research hinges on being able to accelerate sub-atomic particles to nearly the speed of light. Superconductor magnets make this possible. CERN, a consortium of several European nations, is doing something similar with its Large Hadron Collider (LHC) recently inaugurated along the Franco-Swiss border.

Electric generators made with superconducting wire are far more efficient than conventional generators wound with copper wire. In fact, their efficiency is above 99% and their size about half that of conventional generators. These facts make them very lucrative ventures for power utilities.

General Electric has estimated the potential worldwide market for superconducting generators in the next decade at around $20-30 billion dollars. Late in 2002 GE Power Systems received $12.3 million in funding from the U.S. Department of Energy to move high-temperature superconducting generator technology toward full commercialization.

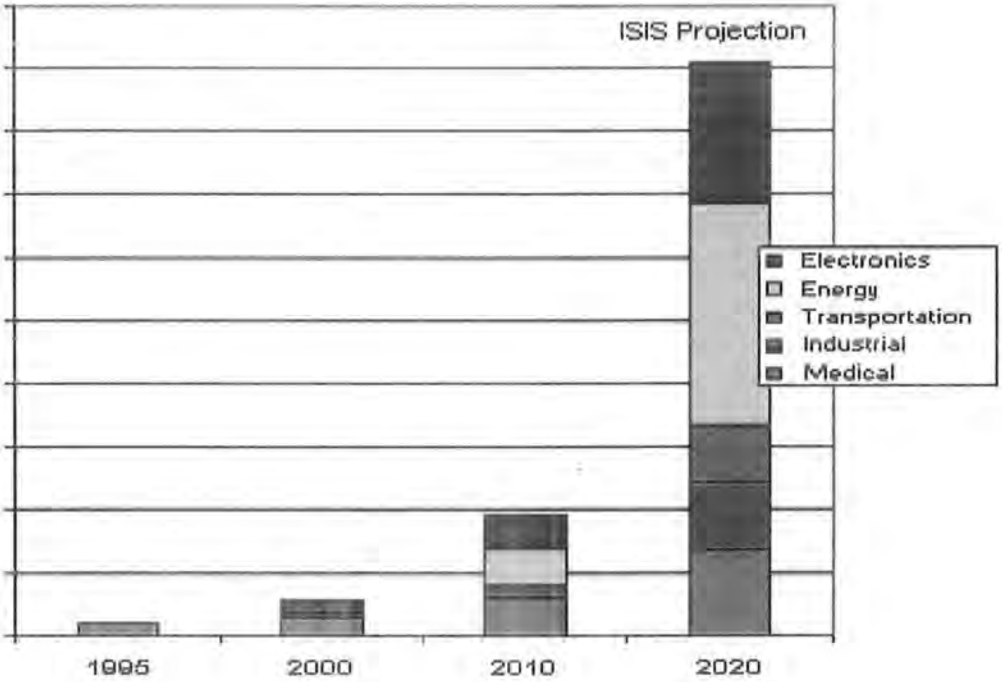

Fig. 1.11: comparison of commercial uses of superconductivity over the years.

Reference:

1. H. Kamerlingh Onnes, Comm. Physical Lab. Univ Leiden 122 and 124 (1911)1226
2. H. Kamerlingh Onnes, Comm. Physical Lab. Leiden 133d (1913) 51
3. J. Bardeen, L. Cooper and J. R. Schrieffer Phys. Rev. 108, 1175 (1975)
4. S. Uchida, T. Ido, H. Takagi, T. Arima, Y. Tokura and S. Tajima Phys. Rev. B 43, 7942 (1991)
5. C. W. Chu, P. H. Hor, R. L. Meng, L. Gao and Z. J. Huang Science 225, 567 (1987)
6. R. J. Cava, A. Santoro, D. W. Johnson and W. W. Rhodes Phys. Rev. B 35,6716 (1987)
7. C. W. Chu, P. H. Hor, R. L. Meng, L. Gao, Z. J. Huang and Y. Q. Wang Phys. Rev. Lett. 58, 405 (1987)
8. Charles Kittles Introduction to Solid State Physics, 7th Edition
9. M. A. Omar Elementary Solid State Physics, 3rd Edition, (2007)
10. B. Morison, D. S. Ginley, J. E. Schirber and E. L. Venturini Physica C 156 (1988) 587
11. C. Martin, C. Michel, A. Maignan, M. Hervieu and B. Raveau C. R. Acad. Sci. Ser 2, vol 307, (1988) 27
12. H. Ihara, K. Tokiwa, H. Ozawa, M. Hirabayashi, A. Negishi, H. Matuhata and Y. S. Song Jpn. J. Appl. Phys. 33 (1994) L503
13. K. Tokiwa, H. Aota, C. Kunugi, K. Tanaka, Y. Tanaka, A. Iyo, H. Ihara and T. Watanabe Physica B 284 (2000) 1077
14. K. Tanaka, A. Iyo, N. Terada, K. Tokiwa, S. Miyashita, Y. Tanaka, T. Tsukamoto, S. K. Agarwal, T. Watanabe and H. Ihara Phys. Rev. B 63 (2001) 064508
15. T. Shibata, T. Tatsucki, S. Adachi, K. Tanabe, S. Fujihara and T. Kimura Physica C 353 (2001) 200
16. N. A. Khan, Y. Sekita, H. Ihara and A. Maqsood Physica C 377 (2002) 43
17. H. Ihara, K. Tanaka, Y. Tanaka, A. Iyo, N. Terada, M. Tokumoto, M. Ariyama, I. Hase, A. Sundaresan, N. Hamada, S. Miyashita, K. Tokiwa and T. Watanabe Physica C 341 (2000) 487

18. K. Tanaka, A. Iyo, Y. Tanaka, K. Tokiwa, M. Tokumoto, M. Ariyama, T. Tsukamoto, T. Watanabe and H. Ihara Physica B 284 (2001) 1081
19. N. A. Khan, M. Mazhar and Asghari Maqsood Supercond. Sci. technol. 15 (2002) 577
20. Solid State Physics An Introduction to Theory and Experiment, Harald Ibach, Hans Luth, 3rd Ed (2003)
21. M. S. Vijaya and G Rangarajan Materials Science, Tata McGraw Hill (2003)
22. James F. Annett superconductivity, superfluids and condensates Oxford univ press. May (2003)
23. F. London and H. London Proc. Roy. Soc. A 149 (1935) 71-88
24. V.V Schmidt, (Eds) P. Muller, A. V. Ostinov, The Physics of Superconductors (1997)
25. L. Cooper Physical Review 104 (1956) 1189-1190
26. W. Meissner and R. Ochsenfeld Naturwissenschaften 21 (1933) 787-788.
27. A. A. Abrikosov Soviet Physics JETP 5 (1957) 1174-1182.
28. S.O.Pillai Solid State Physics, 5th Edition, 2002, New Age International (p) Limited Publishers

LITERATURE REVIEW

2.1 LITERATURE REVIEW:

H. M. Zhou et al [1] studied $Nd_{1.85}Ce_{0.15}Cu_{1-x}Mn_xO_4$ samples with Mn doping up to 30%. They studied the effects of Mn substitution on crystal structure by X-ray diffraction, superconductivity and normal-state magnetic properties. Mn dopants do not induce any crystal structure transition in this system unlike its effect on LSCO and YBCO but an O–T transition in NCCO, shows a different role of Mn. An orthorhombic-to-tetragonal structure transition takes place due to Mn doping in NCCO and significantly suppresses the superconductivity for both T_c and Meissner volume. As it is known that the effective magnetic moment per isolate Mn^{2+} ion is 5.9μB for S = (5/2), which is much greater than 1.9μB for Cu^{2+}. Therefore, the increased Δμ in Mn-doped NCCO can be related to a larger magnetic moment of Mn^{2+} than that of Cu^{2+}. However, deep study reveals that Δμ is apparently larger than the stoichiometric contribution of the Mn^{2+} ion magnetic moment. The phenomena can be contributed to the magnetic correlation between Mn ions and other elements (Nd, Ce, Cu) because this correlation enhances the lattice cell magnetic moment. With increasing Mn content the effective magnetic moment per lattice cell increases and as a result we get antiferromagnetic correlation at high doping levels and a complete destruction of superconductivity. These unique features are the evidence that the response of superconductivity to the magnetic impurities in NCCO is intrinsically different from that in LSCO and YBCO system.

H. Wu and S. Tan [2] studied the effect of Mn substitution for Cu in Mn doped $La_{1.85-(4/3)x}Sr_{0.15+(4/3)x}Cu_{1-x}Mn_xO_4$ (x=0.06) by performing electric resistivity, magnetization and electron spin resonance experiments. In cuprate superconductors, the super exchange interaction through pd's hybridization causes the AF correlation between the Cu^{2+} spins. Because the hybridization strength between Mn^{3+} and O^{2+} states is quite different from that between Cu^{3+} and O^{2+}, it is less possible that the correlation between Mn and Cu can be established. So, when Mn ions with mixed valence are doped into the CuO_2 planes, it can be expected that the super exchange interaction between Mn^{3+} and Mn^{4+} will form and lead to ferromagnetism. The super exchange ferromagnetism of Mn ions cannot usually exist for a homogeneous distribution and for the particular concentration of Mn ions (x=0.06). The ESR spectra study reveals that the distribution of Mn ions in $La_{1.77}Sr_{0.23}Cu_{0.94}Mn_{0.06}O_4$ is inhomogeneous microscopically and there are two kinds of steric states of Mn ions in the CuO_2 planes. The first state are the one which are randomly distributed and isolated Mn ions which are in paramagnetic state and the other corresponds to the Mn ions which have other Mn ions in their neighborhood and form clusters. These clusters exhibit ferromagnetism, which coexists with the superconductivity. Both $(La,Sr)_2CuO_4$ and $(La,Sr)_2MnO_4$ have the same K_2NiF_4 structure and can exist independently and are responsible for the phenomena. When prepared by the conventional solid-state reaction method, it is much possible for the $(La,Sr)_2MnO_4$ to exist independently in the $(La,Sr)_2CuO_4$, so the Mn–O–Mn and Cu–O–Cu can exist in the same plane. The superconductivity coexists with ferromagnetism originating from the Mn^{3+}–O–Mn^{4+} super-exchange interaction in mixed-valence Mn doped $La_{1.85-(4/3)x}Sr_{0.15+(4/3)x}Cu_{1-x}Mn_xO_4$ (x=0.06).

The magnetic state in the $La_{1.85-2x}Sr_{0.15+2x}Cu_{1-x}Mn_xO_4$ ($0 \le x \le 0.5$) system has been studied by C. Zhang et al [3]. The doping of Mn at the Cu site generates interesting phenomena. The un-doped compound La_2CuO_4 is an insulating antiferromagnet where the spin moments on adjacent Cu^{2+} ions are antiparallel. By doping Sr^{2+} the super-exchange interaction of Cu^{2+}-O-Cu^{2+} depresses and as a result it destroys the long-range AFM correlation. In the $La_{1.85-2x}Sr_{0.15+2x}Cu_{1-x}Mn_xO_4$ samples, the T_c value remains at 37K for $x \le 0.06$ samples, this shows that the doping of Mn ions does not lead to magnetic pair-breaking effects. Within a broad doping level $0.1 \le x \le 0.32$ the doping of Mn ions induces a compensated state on some length scale which leads to the formation of AFM correlation which suppresses the superconductivity. The superconducting phase and the AFM phase coexist in these samples. In a high-temperature superconductor AFM phase can be induced by an applied magnetic field. There is a competition between the SC (diamagnetism) phase and AFM phases. At a low doping level, i.e. $x \le 0.06$ the diamagnetism leads the AFM correlation. Thus these samples exhibit a superconducting transition. With increasing doping concentration more and more AFM regions are introduced into the lattice and the Meissner volume continue to decrease. A

Mn-O-Mn double exchange interaction exists at $x \geq 0.32$ and the paramagnetism observed is compatible with double exchange.

A. Chainani et al [4] studied the electronic structure of $La_{1-x}Sr_xMnO_{3+\delta}$ x =0, 0.1, 0.2, 0.3 and 0.4 across the semiconductor metal transition, using various electron spectroscopy techniques. For x≥0.2 an unusual semiconductor-metal transition was observed from the negligible intensity seen at E_F using ultraviolet photoemission spectroscopy and Bremsstrahlung Isochronal Spectroscopy (BIS) and this is consistent with the resistivity data. The BIS spectra showed that the doped holes states develop about 1.4eV above E_F. Auger electron spectroscopy gives an estimate of the intra-atomic coulomb energy in the O 2p manifold to be about 6.8eV. The Mn 2p core-level spectra for different x values appear to be very similar, with peak position identical in all cases. The Mn 2p core level spectra from $LaMnO_3$ and $SrMnO_3$ are approximately similar and this might be the reason for the absence of pronounced changes in the Mn 2p spectra for different x values. They found that there is small increase in the full width at half maxima (FWHM) with increasing x thus for the $2p_{3/2}$ core-level spectra, the FWHM is 4.1eV for $LaMnO_3$, 4.3eV for $La_{0.9}Sr_{0.1}MnO_3$ and about 4.5eV for x ≥0.2. In all these spectra, the $2p_{3/2}$ core-level binding energy appears at about 653.6eV. A broad weak intensity satellite is also observed at about 665.3eV binding energy. The Mn 2p core-level spectrum of $LaMnO_3$ gives parameter values of the charge transfer energy 5.0eV, the hybridization strength between Mn 3d and O 2p states, t=3.8eV and the on-site coulomb energy in Mn 3d states U_{dd} =4.0eV, suggesting a mixed character for the ground state of $LaMnO_3$.

D. Berardan et al [5] reported the study on the electrical transport properties of the Mn-doped $LaFe_{1-x}Mn_xAsO$ oxypnictides system. They have partially substituted iron by manganese in the FeAs layer of LaFeAsO. The increase in the lattice parameters is strongly connected to an increase of the Fe–As bond length determined by Rietveld refinement. The Fe–As bond length increases by almost 1% as Mn fraction increases from x=0 to x= 0.1.This behaviour is in agreement with the Mn–As bond length being much larger in manganese oxypnictides than in iron oxypnictides. La–O bond length almost remains unchanged with Mn doping. With an increase of both *a* and *c* lattice parameters, an increase in the Fe–As and Fe–Fe bond lengths and an evolution of the angles of the $FeAs_4$ tetrahedron that becomes more regular are observed. The temperature of the structural transition observed in LaFeAsO is gradually decreased with Mn doping and it eventually vanishes. The density of state of LaMAsO compounds depends on the shift of the Fermi level toward the top of the valence band with addition of electrons from M=Mn to M= Ni. Therefore, they expected a symmetric effect of Mn doping. The suppression of the structural transition does not lead to the emergence of superconductivity, and a metal–semiconductor transition is observed with Mn doping around $x = 0.03$. This transition corresponds to the opening of a small gap in the vicinity of the Fermi level. Hole doping using strontium and electron doping using fluorine shows symmetric behaviour of the doping in the LaO layer, but in the FeAs layer the electronic structure reveals to be quite sensitive to the substitutions on the transition metal site.

A study has been made on the effect of Mn substitution on the thermo-power of MgB_2 superconducting compounds involving 0%, 0.5%, 1.0%, 1.5% and 2% Mn content by A. Rao [6]. For the pure compound of MgB_2 the transition temperature has been found to be very sharp and the transition width increases with Mn content. For small values of Mn content, the thermo-power S(T) increases which suggests that the hole density increases. But with further increase in Mn content, a small decrease in S(T) is observed. For all the compounds, the expected linear region at low temperatures is observed. There is no systematic trend in the slopes of dS/dT with Mn content.

A. K. Shikov et al [7] reported on the addition of manganese in elements of matrix for internal-tin Nb_3Sn strands. 1.8 wt% Mn in elements of matrix before reaction heat treatment and 1 wt% Mn in matrix after reaction have been fabricated by internal-tin method. One of the produced strands had reinforced stabilizer from CuNb nano-composite alloy. They determine the growth rate of Nb_3Sn layer in superconductor's filaments of manganese doped strands. Microstructures of Nb_3Sn filaments after reaction heat treatment were investigated by SEM and TEM microscopes. The critical current density in magnetic fields up to 20T, hysteresis losses, critical temperature and mechanical characteristics were measured. The increase of critical current density in internal-tin Nb_3Sn strands with manganese doped matrix and the formation of fine microstructure Nb_3Sn layers were revealed. Reinforced multifilamentary Nb_3Sn internal-tin strand with CuNb nanocomposite reinforcing element and external Nb barrier was designed and fabricated. The strands mechanical strength has been increased more than 30% and the introduction of outer Nb diffusion barrier prevented the degradation of RRR in Cu stabilization. The increase of Nb_3Sn layer growth rate in superconductor's filaments of manganese doped strands was observed. For reinforced strand the critical current density in 12T was equal to 1030 A/mm^2 and in 18T attained 170 A/mm^2.

P. Shah et al [8] studied the Temperature dependent Mössbauer measurements of $La_{1-x}Ca_xMn_{1-y}Fe_yO_3$ with $x = 0.0$ and 0.25; $y = 0.01$. Iron substitutes Mn as a trivalent ion. X-ray diffraction patterns of both the samples of $La_{1-x}Ca_xMn_{0.99}Fe_{0.01}O_3$ $x = 0.0$ and 0.25 show that the samples are in single phase. Resistivity measurement of the sample with $x = 0.25$ show the typical metal–insulator transition around 175K. For $x = 0.0$ composition the sample remains insulating up to 10K and both the second order Doppler shift and recoilless fraction exhibit a Debye behavior in the temperature range 90K to 500K. The Mössbauer spectrum for $x = 0.0$ sample remains a quadrupole doublet at all temperatures as expected. No magnetic phase transition in this sample is seen. Upon lowering the temperature, the samples with composition $x = 0.25$ undergoes a magnetic phase transition from the paramagnetic to ferromagnetic state around 175K. In an earlier Mössbauer study of $La_{0.75}Ca_{0.25}Mn_{0.98}Fe_{0.02}O_3$, it was found that the paramagnetic and ferromagnetic phases co-exist over a wide temperature range. In contrast, in the present case the two phases co-exist over much narrower range of temperatures. This gradual transition from para- to ferro-magnetic transition may at least partly be attributed to some compositional in-homogeneity in the specimen. On the contrary, in the specimen with $x = 0.25$, both of these parameters exhibit a marked deviation from the Debye behavior in a temperature interval which correlates with the metal–insulator transition temperature in the system. Decrease in both SOD-shift and recoilless fraction in this temperature interval indicate additional contributions to the rms velocity as well as rms displacement of the Mössbauer atom. These observations provide direct evidence that at least a part of the Jahn–Teller distortions are dynamic in nature.

Electric resistivity and magnetic susceptibility were measured for single crystal of $La_{1-x}Sr_{1+x}MnO_4$ ($0.0 \leq x \leq 0.7$), by Y. Moritoma et al [9]. The single crystals were grown by the floating zone method. They varied the nominal holes concentration with hole doping. The nominally hole undoped compound $LaSrMnO_4$ (x=0.0) is known to be an antiferromagnet. Mn valence from 3^+ (x=0.0) to 4^+ (x=1.0) can be controlled in a solid solution without changing the two dimensional Mn-O-Mn network. Confinement of the Mn-O-Mn network in two dimensions should reduce the critical temperature. Due to the competition between the generic antiferromagnetic superexchange interaction and the ferromagnetic double exchange interaction the antiferromagnetic phase transition decreases and eventually a spin glass phase appears for $x \geq 0.2$. At x=1/2 real space ordering of the doped holes occurs at 220k accompanying a steep increase of resistivity as well as a suppression of susceptibility.

A. Rao et al [10] reported the effect of Mn doping on upper critical field and specific heat of $Mg_{1-x}Mn_xB_2$ system. Among the various substitutions, there are only three successful reports on Mn doping, two on single crystals and the other on bulk sample. The most remarkable feature of Mn substitution is that it exhibits the most rapid decrease in transition temperature. This decrease in T_c can be due to spin-flip scattering and (or) pair-breaking effect. Due to rapid decrease in transition temperature they have used low concentrations of Mn. On the other hand, the magnetic element Fe shows much slower variation in T_c in comparison with Mn. The XRD patterns indicate that all the samples were single phased. There is an increase in a parameter with increase in Mn content. They have used the semi-adiabatic heat pulse method to measure low temperature specific heat at constant pressure C_p, of Mn-doped samples. This method gives the absolute values of heat capacity with an accuracy of about 1%. The results of specific heat do not show a sharp discontinuity around the transition temperature. Instead C_p increases gradually as the specimen undergoes the transition from normal to superconducting state. For comparison, they have also done specific heat measurements on one sample of Fe-doped (1%) compounds. The rate of decrease of ΔC_P for Mn-doped samples is about one third of that for Fe doped sample.

The detailed synthesis condition of Mn doped $La_{1.85}Sr_{0.15}Cu_4$ superconductors and the effects of the synthesis condition on the onset critical transition temperature were discussed by C. J. Zhang et al [11]. They substitute Mn in $La_{1.85}Sr_{0.15}CuO_4$ superconductor. Actually at first they met some problems in the preparing of Mn doped samples. They found that it was difficult to get single phase Mn doped $La_{1.85}Sr_{0.15}CuO_4$ samples by following the traditional solid-state reaction method which was inflected by some impurity peaks. Mn ions are generally existed at valence state between 3^+ and 4^+ in perovskite-type oxides, such as $La_{1-x}Sr_xMnO_3$, $La_{1-x}Sr_{1+x}MnO_4$ and $La_{2-x}Sr_{1+x}Mn_2O_7$. The strong decrease of carrier concentration induced by Mn doping can be compensated by the simultaneous change of Sr^{2+} and Mn concentration. The minor impurities are very harmful to the superconductivity and thus decrease T_c. This behavior is quite peculiar and puzzling. They only guess the possible reason which explains this behavior. If the mixture of La_2O_3, $SrCO_3$, CuO, and MnO_2 powder is preheated under temperature of 900°C, 950°C, or 1000°C, the mixture may react and form K_2NiF_4 type phase. Whereas, the optimal reacting temperature for forming K_2NiF_4 type structure is about 1150°C and the solid-state reaction is less complete when the reaction temperature is lower. If the solid-state reaction is not complete, the contents after preheating would be mixture of K_2NiF_4 type $La_{2-x}Sr_xCu_{1-y}Mn_yO_4$, and the un-reacted La_2O_3, $SrCO_3$, CuO, and MnO_2 powder. To make things worse, it is well known that other perovskite manganites ($La_{1-x}Sr_xMnO_3$ and $La_{2-x}Sr_{1+x}Mn_2O_7$) can be formed at such temperatures. Once they are formed, these manganites are very stable and difficult to decompose even at high temperature (for example $La_{1-x}Sr_xMnO_3$ is stable and does not decompose at over 1400°C). Thus assuming that small amount of impurities are formed during preheating (for example at 1000 °C), they would be stable and can not be eliminated in the following preheats and the final sinter. In order to avoid these impurities, they improved the procedure in the solid-state reaction. The mixture of the starting materials is weighed and grounded thoroughly and directly preheated at high temperature of 1150°C without low temperature preheating. The preheating was performed twice at the same temperature and the pressed pellets were sintered at the same temperature. Using this special improvement, they were able to get single phase samples without any impurities.

J. Zhang et al [12] studied the substitution of 3d transition metal Mn at Cu-site. Mn-doped $Bi_{1.6}Pb_{0.4}Sr_{1.6+2x}La_{0.4-2x}Cu_{1-2x}Mn_xO_2$ ($0 \le x \le 0.2$) and $Bi_{1.6}Pb_{0.4}Sr_{1.6}La_{0.4}Cu_{1-x}Mn_xO_2$ ($0 \le x \le 0.4$) polycrystalline samples were investigated systematically, by means of X-ray diffraction (XRD), Raman scattering and infrared (IR) spectroscopy. The experimental results revealed that the microstructure of Bi2201 phase was affected strongly by Mn doping in CuO_2 plane. With the increase of Mn doping content, irregular changes in the lattice parameters have been found in $Bi_{1.6}Pb_{0.4}Sr_{1.6}La_{0.4}Cu_{1-x}Mn_xO_2$ ($0 \le x \le 0.4$) system. The irregular microstructure changes were largely attributed to the strong Jahn–Teller distortion of MnO_6 octahedron induced by Mn^{3+} ions and charge-transfer effects induced by the aliovalent substitution of Mn^{3+} /Mn^{4+} ions for Cu^{2+}.

S.T. Ruggieroa et al [13] discussed the superconducting and electron-transport properties of Mn-doped ferromagnetic materials by sputter deposition. In the ferromagnetic doped materials, such as Fe and Ni, their T_c does not produce a rapid suppression. The rate of T_c suppression with Mn doping is lower than typically observed with Abrikosov–Gor'kov pair breaking with magnetic dopants. According to the Kaiser theory in the context of the Friedel–Anderson model, the suppression of T_c in Al–Mn alloys is result of pair scattering from resonant magnetic impurity sites. They have synthesized the films with specific Mn concentrations by phase spread in which the substrate was held fixed between pure Al and Al–Mn sputter targets. The sharpness of transitions is a key parameter for tunneling electron spectroscopy (TES) applications, which is quantified by $\alpha=\partial(\ln R)/\partial(\ln T)$ where larger values represent sharper transitions.

V. F. Masterov et al [14] reported on the study of doped manganese by the electron spin resonance spectroscopy (ESR) method. The BSCCO (2212) samples were prepared with composition $Bi_2Sr_2CaCu_{2-x}Mn_xO_y$ with x=0 and 0.8 by the spontaneous crystallization method. Measurements of the microwave absorption were performed on a Bruker ER 220 D spectrometer in the temperature interval 3.7–100K and the ESR spectra was recorded at T=50K. The ESR spectrum of the Cu^{2+} ions will be weaker if structure of superconductors is perfect. In a high T_c superconductor crystal the 3*d* states of copper form an energy band and the *d* function delocalize due to which the spin-lattice relaxation rate increases sharply. The introduction of high-spin (S=5/2) manganese for copper ions (S=1/2) increases the internal magnetic field and as a result increases the effective *g* factor up to 2.34. This provides a confirmation that manganese displaces copper atoms in the CuO_2 planes of the lattice. The intensity of the spectrum of Cu^{2+} ions in the manganese-doped crystal decreases to the lower oxygen deficit in the crystal. As a result a large number of identical internal Josephson junctions and zero-field oscillations of the Q of the microwave resonator appears. The spectrum due to Mn^{2+} ions is not present because 3*d* states of this ion fall into the 3*d* band of the BSCCO (2212) crystal.

H. Huang et al [15] discusses the effects of Mn doping on the superconductivity in $La_{2-x}Sr_xCuO_4$ superconductor. The polycrystalline sample $La_{1.85-1.5x}Sr_{0.15+1.5x}Cu_{1-x}Mn_xO_4$ ($x \leq 0.1$) were prepared by means of a conventional solid state reaction method using high-purity powders of La_2O_3, $SrCO_3$, CuO, and MnO_2. The mixed powders were pressed into pellets and then reacted at 1150°C for 48 hours under oxygen pressure. The lattice parameters were determined from the d-value of XRD peaks by a standard least-squares refinement method. The diffraction peaks were found to be tetragonal. With increasing x, the (004), (006) and (105) peaks shift to higher angle and the (110) and (200) peaks shift to lower angle which means that the length of a-axis increases while the length of c axis decreases with increasing x. The quantitative analysis of elements indicates that the composition is compatible with the $La_{1.85-1.5x}Sr_{0.15+1.5x}Cu_{1-x}Mn_xO_4$. All samples prepared were homogeneous, single tetragonal phase and the additional Sr sits only in the La site, and Mn only exists in the Cu site. The T_c onset value is about 37K for all superconducting samples. At room temperature, the resistivity increases uniformly with increasing Mn doping content. For the $x \leq 0.06$ samples, the resistivity exhibits metallic behavior from room temperature to T_c. While for $x \geq 0.08$ samples, it exhibits metallic behavior at high temperature and semiconducting-like behavior at low temperature. Magnetic pair-breaking effects can not explain the influence of Mn impurity in $La_{2-x}Sr_xCuO_4$ superconductor. From the magnetic susceptibility results it is clear that the Meissner volume decreases with increasing Mn doping. The introduction of Mn impurity in the CuO_2 plane results in the decrease of superconducting fraction. The introduction of Mn in the CuO_2 plane leads to the localization of charge carriers around the Mn impurities. The superconductivity is destroyed due to the localization around the Mn impurities. However, in the regions where the charge carriers are not influenced by the impurities, the superconductivity remains intact and the T_c value remains unchanged.

A series of Co and Mn doped MgB_2 polycrystalline samples have been synthesized and studied by x-ray diffraction and Raman spectrum by L. Shi et al [16]. The polycrystalline Co and Mn-doped MgB_2 samples with nominal compositions of $Mg_{1-x}M_xB_2$ (M = Co, Mn) ($x = 0, 0.01, 0.02, 0.03, 0.04$) were synthesized by solid state reaction method. The XRD data revealed that the crystal structures of Co and Mn-doped MgB_2 are an AlB_2-type structure with hexagonal space group *P6/mmm*. For Co-doping the *a*-axis of the lattice remains unchanged, while the *c*-axis shows a small increase. In contrast, for Mn-doping as the Mn content increases, the *c*-axis shows an evident decrease, whereas the *a*-axis shows a small decrease. Due to the ionic radii difference of Mn^{2+} and Co^{2+}, the doping of Mn can induce more evident disorder effects than that in the Co doped samples. The large broadening (75 cm^{-1} for $x = 0.03$) of Raman linewidth can not be explained by the substitution-induced disorder effect with different ionic radii. Mn doping may induce a strong localized magnetic moment at the Mg site. Additional structural disorder may be induced by the strong localized magnetic moment due to the exchange interaction between the conduction-electron spin and the magnetic impurity moment. On the other hand, Co impurities in MgB_2 are nearly non-magnetic. Thus, the Raman linewidth is broadened obviously by Mn doping, while Co doping bring in little influence on the Raman linewidth. The additional structural disorder will give a further effect on T_c, and result in further suppression of critical temperature.

G. Xu et al [17] synthesized $Bi_{1.6}Pb_{0.4}Sr_{1.6}La_{0.4}Cu_{1-x}Mn_xO_y$ ($0 \le x \le 0.4$) and $La_{1.85-x}Sr_{0.15+x}Cu_{1-x}Mn_xO_y$ ($0 \le x \le 0.5$) polycrystalline samples by the solid state reaction method. In $La_{2-x}Sr_xCuO_4$ the introduced extra holes reside near the O site and form O^- as reported during spectroscopic analysis. Due to the extra hole located at O of CuO_6 (MnO_6) octahedron, the symmetry of CuO_6 (MnO_6) octahedron reduces. This distortion changes the spin orientation of Cu^{2+} or Mn^{3+} and influences Mn–O–Cu antiferromagnetic super-exchange interaction. The Mn^{3+} spins tend to localize. The electrical conduction in $La_{1.85-x}Sr_{0.15+x}Cu_{1-x}Mn_xO_y$ system for $0.1 \le x \le 0.3$ displays the behavior of thermal activation undergoing Kondo scattering. As $x \ge 0.3$, a new Mn–O–Mn double exchange correlation is formed and its conduction mechanism is variable-range hopping. While for Mn doped $Bi_{1.6}Pb_{0.4}Sr_{1.6}La_{0.4}Cu_{1-x}Mn_xO_y$ ($0 \le x \le 0.4$) system the Bi_2O_2 layers are charge carrier reservoir and the hole does not reside at the O site. The CuO_2 plane is under compression, which favors to nearly remain a constant length of in-plane Cu–O bond upon the doping. Hence, effective Mn–O–Cu can form anti-ferromagnetic (AF) super-exchange interaction. The spin dynamics of La_2CuO_4 by Cu^{2+} ESR measurements failed, because of the strongly Cu–O–Cu spin correlation. The Mn doped system $Bi_{1.6}Pb_{0.4}Sr_{1.6}La_{0.4}Cu_{1-x}Mn_xO_y$ may be similar to that case, but the Mn–O–Cu spin correlation is weaker than Cu–O–Cu spin correlation. So at high Mn doping level a weak ESR signal can be observed. The microstructure of CuO_6 in $La_{1.85-x}Sr_{0.15+x}Cu_{1-x}Mn_xO_y$ system and in $Bi_{1.6}Pb_{0.4}Sr_{1.6}La_{0.4}Cu_{1-x}Mn_xO_y$ is different, and the doped Mn shows variable spin correlation characteristics in the two systems. Mn spins in $La_{1.85-x}Sr_{0.15+x}Cu_{1-x}Mn_xO_y$ are more localized than that in $Bi_{1.6}Pb_{0.4}Sr_{1.6}La_{0.4}Cu_{1-x}Mn_xO_y$ system.

A. Baranauskas et al [18] studied the effects of Mn doping at the Cu-sites, on the structural and superconducting properties of $YBa_2Cu_4O_8$ (Y-124) system. Multi-metallic oxide powders $YBa_2(Cu_{1-x}Mn_x)_4O_8$ (x=0.00, 0.01, 0.02, 0.03, 0.04 and 0.05) have been prepared by a simple aqueous sol-gel method at an oxygen pressure of 1 atm starting from an aqueous mixture of the metal acetates. Homogeneous gels were achieved by complexing copper ions by tartaric acid before the gelation process. Thermal decomposition of the gels was studied by thermo-gravimetric analysis. Effects of manganese substitutions on the properties of compounds were studied by X-ray powder diffraction, TG analysis, IR spectroscopy and resistivity measurements. The critical temperature of superconductivity decreases dramatically from 79K for the non-substituted sample, $YBa_2Cu_4O_8$, to 41K for the sample with 2% of manganese substitution in $YBa_2(Cu_{0.98}Mn_{0.02})_4O_8$. The decrease of the transition temperature, as a result of the Mn substitution, cannot be explained directly by magnetic pair breaking or destruction of the antiferromagnetic correlation of the Cu atoms in the planes. According to the XRD analysis and stability measurements under controlled oxygen atmospheres, impurity phases, such as Y-123 and Y- 247, have formed in the samples with a 1 and 2% of manganese substitution level under the usual preparation conditions. On further increasing the manganese substitution level, the peaks due to the Y-124 phase disappeared in the diffraction scans. They draw the conclusion that these structural changes are mostly caused by the considerable difference in the ionic radius of copper and manganese.

I. G. Deac et al [19] presents a detailed study of the polycrystalline perovskite manganites $La_{0.67}Ca_{0.33}Al_xMn_{1-x}O_3$ ($x = 0, 0.1, 0.15, 0.5$) at low temperatures and high magnetic fields, including electrical resistance, magnetization and ac susceptibility measurements. Polycrystalline samples with nominal composition $La_{0.67}Ca_{0.33}Al_xMn_{1-x}O_3$ ($x = 0, 0.1, 0.15, 0.5$) were prepared by standard ceramic reaction method. The compounds were sintered in air at 14000°C for 24h. The X-ray diffraction patterns of $La_{0.67}Ca_{0.33}Al_xMn_{1-x}O_3$ showed that the compounds are mainly clean single phase, within the limit of experimental errors. The space group P*nma* was used for the structural refinement in all the samples. The unit-cell volume, continuously decreases from $V = 231.99Å^3$ for the sample with $x = 0$ to $V = 221.62Å^3$ for the samples with $x = 0.5$, and this decrease is consistent with the lower size of Al^{3+}. For lower temperatures region the curve $\chi_{dc}^{-1}(T)$ has a positive curvature, suggesting that ferromagnetic cluster began to create. The high value of the Curie constant just above T_c (C = 6 emu K/mol) for samples with $x < 0.1$ means that the effective moment is larger than that expected for free manganese ions in $La_{0.7}Ca_{0.3}MnO_3$ (C = 2.629 emu K/mol). This can be explained by the presence of magnetic clusters. For the sample with $x = 0.5$ the Curie constant is C =1.43 emu K/mol, and $\chi_{dc}^{-1}(T)$ is linear in the range 120-300K. The low Al doping can create a large distribution of FM domains below T_c and thick barrier between grains. At high Al content the small FM domains can fill better the sample creating many percolation paths, decreasing the residual resistivity. The behavior of the most doped samples (i.e. lower resistivity) seems to be an effect of the presence of very small FM clusters for $T < T_c$. For high Al content the Jahn-Teller distortion of Mn^{3+} ions is weakened and this can make the structure more symmetric with a sharp M-I transition and a lower residual resistivity. For higher temperatures $T > T_c$, in the absence of FM metallic domains Al acts as a potential scattering center and it cuts off the magnetic interaction between the Mn ions. This makes the resistivity higher and the sample more paramagnetic (with smaller FM clusters) with increasing Al content, for this temperature region.

J. Zhang et al [20] studied the low temperature transport behavior and its dependence on applied magnetic field for dilute Mn-doped $Na\gamma Co_{1-x}Mn_xO_2$ with ($0.70<\gamma<0.75$) x=0, 0.03, 0.07, 0.1. A minimum resistivity was discovered for all the doped samples at low temperatures and was weakly dependent on the external magnetic field. From the susceptibility measurements, the results prove the coexistence of Kondo scattering and possibly enhanced electron-electron interaction induced by dilute Mn doping. The electrical and magnetic properties at low temperatures are very sensitive to Mn doping while the doping effects are not so obvious at higher temperatures.

Some new members of a Rutheno-cuprate (2212) series have been synthesized by Mn substitution for Ru in $Gd_{1.4}Ce_{0.6}Sr_2RuCu_2O_{10}$ [21]. On substitution a significant change in lattice parameter for a very low substitution level (1 mole% of Ru) was observed. The pristine compound shows coexistence of superconductivity and magnetism. The magnetic and superconducting properties observed in Ru (1222) system are a result of interactions in the Ru-O and Cu-O planes. The interaction between the planes has a key role to play in determining the properties of the system. X-ray absorption and NMR studies indicate mixed valence of Ru namely 95% Ru^{5+} and 5% Ru^{4+}. Due to this mixed valence a double exchange mechanism inside the RuO_2 sheets was proposed, mediated by the small canting or leaning of the Ru octahedral as an explanation for the weak ferromagnetism. From transport and spectroscopic studies one can believe that due to mixed valence states RuO_2 planes should be conducting. Mn enters either as 4^+ or 5^+ or as a mixture of 4^+ and 5^+ in the system because Mn doping has been carried out in oxygen atmosphere and a drastic decrease in *c*-parameter is observed. Mn will not assume 2^+ and 3^+ as they will have higher ionic radii and would not be consistent with the observed large decrease in c-parameter. If Mn enters as a mixture of 4^+ and 5^+ and occupies Ru, it would lead to a change in local coordination from octahedral to tetrahedral as Mn^{5+} generally adopts a tetrahedral coordination. This would also lead to a depletion of oxygen in the system reducing a part of Cu^{2+} to Cu^{1+}. This reduction in charge carrier concentration in CuO_2 plane destroys superconductivity even at 1% substitution and also drives the system to an insulating state. The large fall in holes concentration with smaller percentage of Mn substitution which stabilizes later with higher Mn concentration is also observed. The decrease in resistivity on further substitution of Mn can be understood as Mn^{5+} corresponds to d2 configuration and Ru^{5+} in d3 configuration, this will bring about a hopping conductivity. The lowering of the magnetic transition temperature may be because of the disorder caused in the Ru spin arrangement due to the presence of Mn^{5+} with d2 configuration at random Ru sites. This can explain the smearing of T_{M1} and it may also distort the canting of the Ru moments at lower temperatures thereby reducing the second magnetic transition temperature (T_{M2}).

The influence of the stoichiometric replacement of Bi and/or Pb by Mn on the electric and magnetic properties of the Bi-based superconductors has been studied by D. Sy´korova et al [22]. Bi-2212 and Bi-2223 superconducting phases with nominal composition $Bi_aPb_bMn_cSr_4Ca_5Cu_7O_x$ ($a+b+c=4$) are formed. The partial replacement of Bi by Mn in the Bi-Sr-Ca-Cu-O system without Pb did not promote the formation of Bi-2223, and only the Bi-2212 phase was detected. The probable cause of this behavior is lack of Pb, which is known to support the development of 2223 phase. It follows that Mn itself does not promote the growth of 2223 phase. The partial substitution of Pb by Mn in the Bi (Pb)-Sr-Ca-Cu-O system led to two-phase samples when a large amount of Mn replaced Pb. However, a replacement of Bi by Mn for a fixed content of Pb gives superconductors with a high content of the 2223 phase with critical temperatures T_{cJ} and T_c around or >100K. Longer times of thermal treatment led to samples with a small content of 2212 phase in contrast to the samples sintered for a shorter time, in which presence of 2223 phase only is observed.

G. O`Neil et al [23] produced Al-Mn alloy thin films on electronic-grade silicon wafers using co-sputtering from two adjustable-rate sources. One containing a 99.9995 at.% purity Al target and the other an Al target doped with 3000 ppm Mn, with a stated 99.99 at.% Al purity excluding Mn. They compared all the conductance data with the AG theory. This is the model where fully magnetic Mn impurities suppress the energy gap. AG theory cannot account for their results, as the gap structure is completely washed out. This analysis taken together implies that there is strong scattering from Mn impurities that lack a promising magnetic character, due to strong mixing with the Al conduction electrons. This is consistent with spin-fluctuation measurements and strong resonant-state broadening in Al-Mn alloys was observed. They have demonstrated the BCS-like density of states predicted by the Kaiser theory for energy-gap suppression with nonmagnetic Anderson impurities. Their work implies that the Mn impurities have no measurable magnetic character and act exclusively as strong resonant scattering sites without producing time-reverse symmetry breaking of Cooper pairs.

Mn and Sb-doped $PbZrTiO_3$ (PMSZT) thin-film pyro-electric infrared (IR) detectors have been fabricated by N. J. Wu et al [24] on *c*-axis oriented $YB_2Cu_3O_{7-x}$ (YBCO) thin films. The thin-film hetero-structure detectors were prepared by pulsed laser deposition on $LaAlO_3$ (100) substrates. The YBCO layer in the PMSZT/YBO hetero-structure was used as an atomic template for the epitaxial growth of the PMSZT thin films, as well as a non-superconducting electrode and IR reflector in the detector. Mn and Sb doping was used to tune the $Pb(Zr,Ti)O_3$ transition temperature to a lower values and hence, to modify the pyro-electric and dielectric properties of the pyro-electric material. This also resulted in polarization orientation in the "as-grown" PMSZT film, which was normal to the hetero-structure surface. The high infrared reflectivity and low thermal conductivity of the YBCO electrode layer further enhanced the detector's performance. The PMSZT IR detectors were examined as to their photo-voltage and photocurrent in response to IR source temperature, detector temperature, and chopper frequency. The experimental results show that the detector has relatively high IR sensitivity with a detectivity D^* of 4×10^8 cmHz$^{1/2}$/W, and is capable of operating from room temperature to ~170 °C.

C. P. Sun et al [25] synthesized $Li(Ti_{1-x}V_x)_2O_4$ and $Li(Ti_{1-y}Mn_y)_2O_4$ samples by conventional solid-state reaction method. For the concentration below 0.05 the X-ray diffraction patterns showed single phase. The substitution of V shows only slight increase of resistivity in contrast to a rapid rise in Mn doping. The effective ionic radius of V^{3+} (0.64A°), V^{4+} (0.58A°), Mn^{3+} (0.65A°), or Mn^{4+} (0.53A°) are closed to the Ti^{3+} (0.67A°) or Ti^{4+} (0.61A°) the structure change is not the key factor to cause much influence on transport properties. The resistivity increases 103 times from y = 0 to y = 0.04 in Mn doping shows the extreme sensitivity of transport properties to the electronic effect of 3d transition metals. Magnetization of all samples were performed by zero field cooled (ZFC) mode. The diamagnetic signal is gradually decreased with the high doping concentrations in both cases. The Mn doped samples keep the T_c at about 10K and show an upturn in magnetization at low temperatures. The doping of Mn may go to interstitial sites or reside in grain boundary acting as magnetic impurity scattering centers. It is difficult to imagine the low solid solution in $Li(Ti_{1-y}Mn_y)_2O_4$ since the end members are iso-structural. It happens at such a low concentration, the little change of lattice parameters determined by XRD patterns is unable to verify this conjecture.

Undoped and 2 mol% Mn doped $Ba_{0.6}Sr_{0.4}TiMn_{0.02}O_3$ (BST), i.e. thin films were grown by X. H. Zhu et al [26] on $La_{0.67}Sr_{0.33}MnO_3$ (LSMO) coated $LaAlO_3$ (LAO) substrates by pulsed laser deposition. The growth processes were monitored by high-pressure reflective high energy electron diffraction (RHEED). The structural and dielectric properties of the thin films are also investigated systematically. The improvement in the dielectric properties of BST thin films could be caused because effective potential barriers are formed at grain boundaries with the addition of Mn dopants and the reduction in oxygen vacancies and electron concentration by substituting Mn^{2+} for Ti^{4+}. Part of Mn^{2+} ions are successfully substituted for Ti^{4+} as "B" site acceptor dopants in ABO_3 perovskite BST lattice. The XRD and RHEED analyses confirm that better crystallinity is obtained in the Mn-doped BST film. The dielectric properties of the BST thin films are greatly improved by Mn doping and more homogeneous local microwave dielectric properties are obtained. At room temperature, the (figure of merit) FOM-factor value increases from 11 (undoped) to 40 (Mn doped) at 100 kHz by applying an electric field of 200 kV/cm, and the leakage current density of the BST thin films at a negative bias field of 200 kV/cm decreases from 2.5×10^{-4} A/cm^2 to 1.1×10^{-6} A/ cm^2.

A. Rao et al [27] studied measurements of the linear thermal expansion α for Mn substituted $YBa_2(Cu_{1-x}Mn_x)_3O_y$ ($0\le x\le 2\%$) using a high resolution dilatometer over the temperature range 10-300K. The coefficient of linear thermal expansion $\Delta\alpha$ was found to decrease with increasing Mn content across the superconducting transition temperature. For the pure sample, they observed a negative jump. While a threefold decrease in $\Delta\alpha$ was observed for $x = 0.5\%$. Slight changes in the oxygen content and transition temperature were found, as a function of the Mn concentration. From the experiments performed it is suggested that the substituent Mn is being incorporated into the superconductor as a whole and not in the form of a local cluster. From the Ehrenfest relations, the pressure dependence of T_c, (dT_c/dP) and the discontinuity in the compressibility ΔK are expected to decrease with the Mn concentration.

Mn and Sb doped-PZT (PMSZT)/$YBa_2Cu_3O_{7-y}$ (YBCO) heterostructures have been integrated with YSZ/Si substrates for fabrication of infrared (IR) detector arrays [28]. PMSZT films with good epitaxy on c-oriented YBCO conducting oxide electrodes have been successfully grown by a pulsed laser ablation deposition. The ferroelectric properties of the PMSZT films show good hystersis loops with a coercive field E_c, of 70kV/cm and a remnant polarization P_r, of 15μC/cm^2. I-V curves show that the PMSZT films have high electrical field breakdown strength with values exceeding 400kV/cm. Doping Mn and Sb into PZT has been shown to not only decrease the Curie temperature T_c from 350°C for PZT to l75°C for PMSZT, but also to enhance the IR response of the pyroelectric thin films. PMSZT thin films show excellent dielectric and ferroelectric properties for IR detector applications. The PMSZT thin films offer a significantly higher IR response than the PZT thin films, higher pyroelectric coefficient, and higher figures of merit even without poling treatments. PMSZT detectors have a pyroelectric coefficient of 45 nC/cm^2K at 25°C and 148 nC/cm^2K at 88°C, and pyroelectric figures of merit, F_v of 15.5×10^{-11} C.cm/J and F_d of 9.5×10^{-9} C.cm/J at 25°C. The measured normalized detectivity D* in the 2.5μm – I9.5μm wavelength range varies from 2.5×10^8 cm.Hz ^{½} W to 6.0×10^8 cm Hz $^{1/2}$W.

C. J. Zhang et al [29] for the first time reported on a series of $La_{1.85}Sr_{0.15}Cu_{1-y}Mn_yO_4$ ($0\leq y\leq 0.05$) single crystal samples by the travelling-solvent floating-zone method. Instead of preheating the feed rod materials at intermediate temperatures, they directly preheat the starting materials at 1150°C. After that they grow Mn doped samples at 0.33 mm/h, which is much slower than the widely adopted 1 mm/h rate used in the single crystal growth of $La_{2-x}Sr_xCuO_4$. The XRD patterns show that all the samples are single phase, which can be indexed as having K_2NiF_4-type tetragonal symmetry. The lattice parameter *a* increases monotonically with increasing Mn doping, while the c-axis parameter does not exhibit a predictable change, which means that Mn doping alters the in-plane Cu(Mn)–O bond length effectively, but does not affect the out-of-plane bond length. They performed back-reflection Laue diffraction measurements on all the samples. The crystallographic plane perpendicular to the incident X-ray is identified to be *a* - *b* plane. Then, they cut the single crystals parallel to this plane into pieces about 1 mm in thickness for other polarization experiments, which also confirm that the polarization of the single crystals is good. The superconducting transition temperature of the single crystal samples was checked using a SQUID magnetometer with an external applied magnetic field of 2 Oe. The T_c onset value of the y = 0.015 single crystal is 36.5K. The T_c onset values confirm that Mn doping in $La_{1.85}Sr_{0.15}CuO_4$ does not lead to a rapid decrease in the superconducting transition temperature, unlike in the case of doping with other elements.

Y. G. Shi et al [30] has successfully synthesized $Na_{0.5}Co_{1-x}M_xO_2$ and $Na_{0.3}Co_{1-x}M_xO_2.1.3H_2O$ ($0\leq x \leq 0.1$, M = Mn, Ti) materials. Their structure and low-temperature physical properties have been investigated and analyzed with the increase of doping level. A slight substitution of Mn for Co atoms affects the superconducting property. The superconductivity is found to be destroyed in $Na_{0.3}Co_{1-x}M_xO_2 \cdot 1.3H_2O$ materials with $x > 0.02$ for Mn doping. Both lattice parameters and cell volume show certain irregular change in comparison with the parent $Na_{0.75}Co_{1-x}M_xO_2$ material. This phenomenon arises probably from certain in-homogeneity of the intercalated H_2O and/or Na content. Structural examination of samples prepared under slightly different conditions indicated that the lattice parameters of $Na_{0.3}Co_{1-x}Mn_xO_2 \cdot 1.3H_2O$ ($x \leq 0.1$) generally vary in the range from 2.816A° to 2.826A° within the *a–b* plane and from 19.633A° to 19.788A° for *c*-lattice parameters. The most striking feature is the presence of a common transformation of the low temperature states with Mn/Ti doping. Mn doping in the $Na_{0.5}CoO_2$ material has visibly stronger influence than Ti doping on both charge ordering and low-temperature magnetic properties. This difference is possibly attributable to the stronger influences of Mn ions on local magnetic order within the CoO_2 sheets in addition to the structural changes.

F. Perez et al [31] reported on the ferromagnetic $La_{2/3}Ca_{1/3}MnO_3$ films with thickness between 22 and 35 unit cells, were deposited on single crystal $SrTiO_3$ substrates with crystal plane orientation (001) and covered with ~10 unit cells of superconducting $YBa_2Cu_3O_{7-\delta}$ in order to study their microstructure and physical properties. X-ray diffraction and atomic force microscopy studies showed no dramatic change of the structural and morphological quality of the superconducting top layers with increasing of the thickness of the ferromagnetic layer. Electrical transport and magnetic measurements revealed a strong dependence of both the superconducting transition temperature and the Curie temperature for the onset of ferromagnetic ordering on the thickness of the ferromagnetic layer. A strong dependence of the transition superconducting temperature T_c on the thickness of the LCMO layers suggests some mutual influence of SC and FM. The interaction between the FM and SC layers would take place via proximity effect or the polarization of the conducting holes in the superconductor by a magnetic exchange field. Extrinsic factors like interfacial diffusion between YBCO and LCMO or spin injection of LCMO into YBCO and the transient layer (due to diffusion) may also suppress the superconductivity. Magnetic properties like Curie temperature and saturation magnetization of single LCMO layers also depend on the number of unit cells.

C. H. Renner et al [32] studied microscopic characterization of the phase transitions associated with colossal magnetoresistance (CMR) in manganese perovskite oxides. They investigate $Bi_{1-x}Ca_xMnO_3$ (BCMO) with x =0.76. At this composition, BCMO develops an insulating charge-ordered phase upon cooling, whose study as a function of temperature will allow identifying atomic scale characteristics of the metal-insulator phase transition (MIT). They observe distinct atomic scale phases at temperatures above and below the MIT, with very different electronic and structural characteristics. The charge ordering correlates both with the local conduction state (metallic or insulating) and the local structural order as observed during combining STM micrographs and current voltage tunneling characteristics. Coexistence of distinct phases with different atomic and electronic structures is also observed, but point towards an extrinsic stabilization of domains rather than intrinsic phase separation. Tunneling spectra serve to test microscopic pictures of the different phases, provide valuable input for attempts to model macroscopic properties as a function of temperature and doping.

The origin of the charge-ordered stripe with the orbital ordering is observed experimentally in some manganese oxides [33]. It is emphasized that the long-range Coulomb interaction plays an essential role. They study a Hubbard model with doubly degenerate orbital, and treat the on-site Coulomb interaction and the nearest-neighbor one with the Hartree-Fock approximation. The charge orbital stripe (COS) structure observed in $La_xCa_{1-x}MnO_3$ for x=1/2 and 2/3 originates from the Coulomb interaction. The doubly degenerate e' orbital and the nearest-neighbor Coulomb interaction are important to realize the COS structure. According to the present scenario, the COS structure is realized by the long-range Coulomb interaction, and then the JT distortion occurs so that the COS structure is further stabilized. The JT distortion is the consequence of the COS structure but not the origin of it.

References:

1. H. M. Zhou, Y. Yang, G. Li, C. H. Cheng, M. H. Pu, Y. Zhao Physica C 463–465 (2007) 170–173
2. H. Wu, S. Tan, Y. Zhang Solid State Communications 134 (2005) 725–728
3. C. Zhang and Y. Zhang Physical Review B 68, 054512 (2003)
4. A. Chainai, M. Mathew and D. D Sarma, Physical Review B 47, number 23 (15 June 1993)
5. D. Bérardan, L. Pinsard-Gaudart, N. Dragoe Journal of Alloys and Compounds 481 (2009) 470–472
6. A. Rao, T. Chakraborty, B. Gahtori, C. Sarkar, S.K. Agarwal, A. Soni, G. S. Okram Journal of Physics: Conference Series 234 (2010) 012033
7. A. K. Shikov, V. I. Pantsyrny, A. E. Vorobieva, S. V. Sudyev, N. A. Beliakov, V. V. Sergeev, N. I. Kozlenkova, and M. V. Polikarpova IEEE Transactions on Applied Superconductivity, Vol. 19, No. 3 (June 2009)
8. P. Shah, A. Gupta, D. D. Sarma and K. Kawaguchi Hyperfine Interactions 139/140, (2002), 623–629
9. Y.Moritomo, Y.Tomioka, A.Asamitsu, Y.Tokura, Y.Matsui Physical Review B Volume 51,number 5 (Feb. 1995)
10. A. Rao, B. Gahtori, S. K. Agarwal, T. Chakraborty, C. k. Sarkar, A. Das Physica C 469 (2009) 64–69
11. C. J. Zhang, H. Oyanagi Physica C 468 (2008) 1155–1158
12. J. Zhang, W. Wang, C. Zhang, E. Jang, Jin-Ho Choy, Y. Zhang Physica C 419 (2005) 85–93
13. S. T. Ruggiero, A. Williams, W. H. Rippard, A. M. Clark, S. W. Deiker B. A. Young, L. R. Vale, J. N. Ullom Nuclear Instruments and Methods In Physics Research A 520 (2004) 274–276
14. V. F. Masterov, N. M. Shibanova, and K. F. Shtel'makh Zh. Tekh. Fiz. 67, (October 1997) 137–138
15. H. Huang, M. Tan, C. Zhang, Y. Zhang Physica C 421 (2005) 56– 60
16. L. Shi, S. Zhanga, H. Zhang Solid State Communications 147 (2008) 27–30

17. G. Xu, Q. Pu, B. Liu, J. Zhang, C. Zhang, Z. Ding, Y. Zhang Physica C 390 (2003) 75–79
18. A. Baranauskas, D. Jasaitis, A. Kareiva, R. Haberkorn, H. P. Beck Journal of the European Ceramic Society 21 (2001) 399-408
19. I. G. Deac, L. Giurgiu, A. Darabont, R. V. Tetean, M. Miron, E. Burzo Strongly Correlated Electrons (Cond-mat/0505586) Cornell University Library
20. J. Zhang, Z. Zhang, Y. Xu, C. Jing, S. Cao and Y. Zhao Applied Physics Letters 88, (2006), 122102
21. S.Kalavathi, J.Janaki, T.N.Sairam, Awadhesh mani, R.Rawat and V.Sankara Sastry Superconductivity (Cond-mat/0509633) (2006) Cornell University Library
22. D. Sy´korova, O. Smrc˘kova, and P. Vas˘ek journal of superconductivity: Incorporating Novel Magnetism, Vol. 13, No. 6, (2000)
23. G. O'Neil, D. Schmidt, N. A. Miller, J. N. Ullom, A. Williams, G. B. Arnold, and S. T. Ruggiero Physical Review Letters PRL 100, 056804 (2008)
24. N. J. Wu, Y. S. Chen, J. Y. Fan, and A. Ignatiev Journal of Applied Physics Volume 83, Number 9 (1998)
25. C. P. Sun, Y. F. Huang, S. T. Tsai, C. L. Huang, H. D. Yang Physica B 378–380 (2006) 395–397
26. X. H. Zhu, D. N. Zheng, W. Peng, J. Li, Y. F. Chen Materials Letters 60 (2006)1224–1228
27. A. Rao, S. Radheshyam, R. Kumar, S. Gupta, C. Meingast, B. Gahtori, S. K. Agarwal, K. M. Sivakumar, Y. K. Kuo Journal of Physics Condens. Matter 19 (2007) 056208
28. Y. Q. Xu, N. J. Wu, D. Liu and A. Ignatiev Materials Research Society Symp. Proc. Vol. 493 (1998)
29. C. J. Zhang, H. Oyanagi, C. H. Lee Physica C 468 (2008) 898–902
30. Y. G. Shi, H. X. Yang, X. Liu, W. J. Ma, C. J. Nie, W. W. Huang, J. Q. Li Physica C 432 (2005) 299–305
31. F. Perez, K. Gross, E. Baca, W. Saldarriaga, P. Prieto, M.E. Gomez, O. Mora´n, R. Hott, K. Grube, D. Fuchs, R. Schneider Physica C 432 (2005) 275– 280

32. Ch. Renner, G. Aeppli, H. M. Ronnow Materials Science and Engineering C 25 (2005) 775 – 778
33. T. Mutou, H. Kontani Physical B 281&282 (2000) 531-533

EXPERIMENTAL TECHNIQUES

3.1 Introduction:

In this section, the description of the experimental setups used for the characterization of samples will be discussed.

3.1.1 Sample Preparation:

The $Cu_{0.5}Tl_{0.5}Ba_2(Ca_{2-y}Mn_y)Cu_3O_{12-\delta}$ (y=0, 0.15, 0.25, 0.35, 0.5, 0.75, 1.0, 1.25) samples were prepared by the solid state reaction method accomplished in two stages. At the first stage $Cu_{0.5}Ba_2(Ca_{2-y}Mn_y)Cu_3O_{10-\delta}$ (y=0, 0.15, 0.25, 0.35, 0.5, 0.75 1.0, 1.25) precursor material was prepared, by thoroughly mixing $Ba(NO_3)_2$, $Ca(NO_3)_2$, MnO_2 and Cu(CN) in a quartz mortar and pestle in appropriate ratios. The mixed material was fired twice at 860°C in a quartz boat for 24 hours and furnace cooled to room temperature. At the second stage, the precursor material was ground for about an hour and mixed with Tl_2O_3 to give $Cu_{0.5}Tl_{0.5}Ba_2(Ca_{2-y}Mn_y)Cu_3O_{10-\delta}$ (y=0, 0.15, 0.25, 0.35, 0.5, 0.75, 1.0, 1.25) as final reactants composition. Thallium mixed material was palletized under 3.8 tons/cm^2 and the pellets were enclosed in a gold capsule. Gold capsule containing pellets were annealed for about 7 minutes at 860°C followed by quenching to room temperature. The post-annealing of the samples in flowing oxygen atmosphere was carried out in a Tubular Furnace at 500°C for Six hours

Characterization:

The samples were characterized by the following techniques:

A). X-ray diffraction

B). DC-electrical resistivity measurements

C). Fourier Transform Infrared (FTIR) Spectroscopy

D). AC-susceptibility measurements

A) X- Ray Diffraction:

XRD (X-ray diffraction) analysis gives us the information about the crystal structure of the material. This technique is used to know whether the sample has the desired crystalline structure or not and also to know the lattice cell parameters. The most important aspect in materials science is the study of crystal structure of material. In the beginning of the field of materials sciences, it was assumed that the solid is made of atoms, which are periodically arranged, but there was no experimental evidence of this theory. The discovery of x-rays made it possible to probe the material for their structure determination. The wavelength of x-rays (0.5Å-2.5Å) is comparable to the spacing between the atomic planes in solids. The x-rays, which originate from the K shell transitions, are used for the diffraction analysis because these are shorter wavelength as compared to the one coming from L or M shell transition [1,2]. The commonly used target materials in x-ray tubes are Cu and Mo. These two target material produce x-rays with wavelengths 1.54Å and 0.8Å respectively [3]. An incident x-ray beam on a material penetrates into it and the intensity in the direction of the reflected beam is determined by the periodicity of the atomic planes in the crystalline solid. The consideration of such an x-ray beam of wavelength 'λ' incident on a crystalline material, at an angle 'θ' and diffracted also at the same angle is shown in equation 3.1. The inter-planer spacing of the material is equal to d [4,5]. These rays will interfere constructively when the path difference between the rays is an integral multiple of the wavelength used. The path difference is

$$AB + BC = n\lambda$$

$$AB = d\sin\theta \text{ and } BC = d\sin\theta$$

$$2d\sin\theta = n\lambda, \quad n=0,\ 1,\ 2\ldots \quad (3.1)$$

Where n is the order of diffraction. The above diffraction rule was given by W. L. Bragg and is known as *Bragg's law.* Only the X-rays that satisfied this law will give the diffraction pattern. A schematic diagram is given below

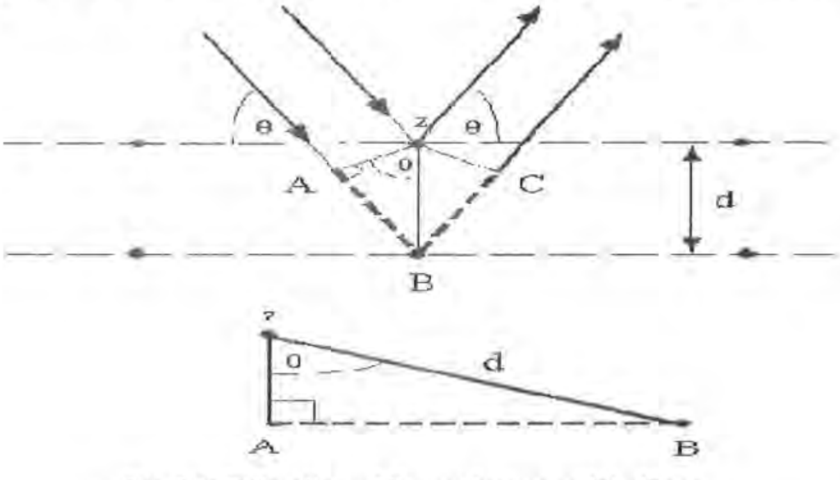

Fig. 3.1: Diffraction of X-rays from crystal planes.

The x-ray diffraction technique is also used to identify whether a material is a crystalline or amorphous. In crystalline solids, many sharp crystalline peaks are observed due to periodic arrangement of atoms, but in the amorphous material there is no periodic structure and only one or two broad diffraction bands are observed. Through this technique, we can also determine the size of the unit cell i.e. lattice parameters, atomic position and phase purity of the material. X-ray diffraction studies of the crystal structure with different orientations of the planes takes place by adopting one of the following methods.

Laue's Method:

In the Laue's Technique a single crystal is held stationary and a beam of radiation is incident on it at a fixed angle θ, i.e. θ is fixed while wavelength λ is varied. These different wavelengths select the appropriate reflecting planes out of the numerous present in the crystal such that the Bragg's condition is satisfied.

Rotating Crystal Method:

In rotating crystal method a single crystal is held in the path of the monochromatic radiations and is rotated about an axis, λ is fixed while θ is varied. Different sets of parallel atomic planes are exposed to incident radiation for different values of θ and reflection takes place for those planes for which d and θ satisfied the Bragg's law.

Powdered Diffraction Method:

In powder method, a sample in the powdered form is placed in the path of monochromatic x-rays, i.e. λ is fixed while both θ and d vary. Thus a number of small crystallites with different orientations are exposed to x-rays. The reflections take place for those values of d, θ and λ which satisfies the Bragg's law. Superconducting sample is polycrystalline and the tiny crystals are randomly oriented so powder diffraction method is usually employed. A powder pattern is therefore, a reasonably complete display of the diffraction effects from a compound. The procedure to analyze the powder pattern of an unknown compound consist of measuring the diffraction angles, calculating the spacing of the reflecting planes and then deducing the dimensions of the unit cell. The schematic diagram of an x-ray diffractometer is shown in Figure. 3.2. Once the scattered peaks data is obtain then the data is analyzed for the determination of the crystal structure. The process proceeds in stages. The first step is to compare the location of the peaks/rings with those produced by the various known crystal structures and effort is made to identify the crystal structure. Next step is refinement procedure; varying locations of atoms and intensities of the species best fitting data is obtained. In our work we used computer software "Check cell" which when provided with peak data, identifies the crystal structure and also provides lattice parameters.

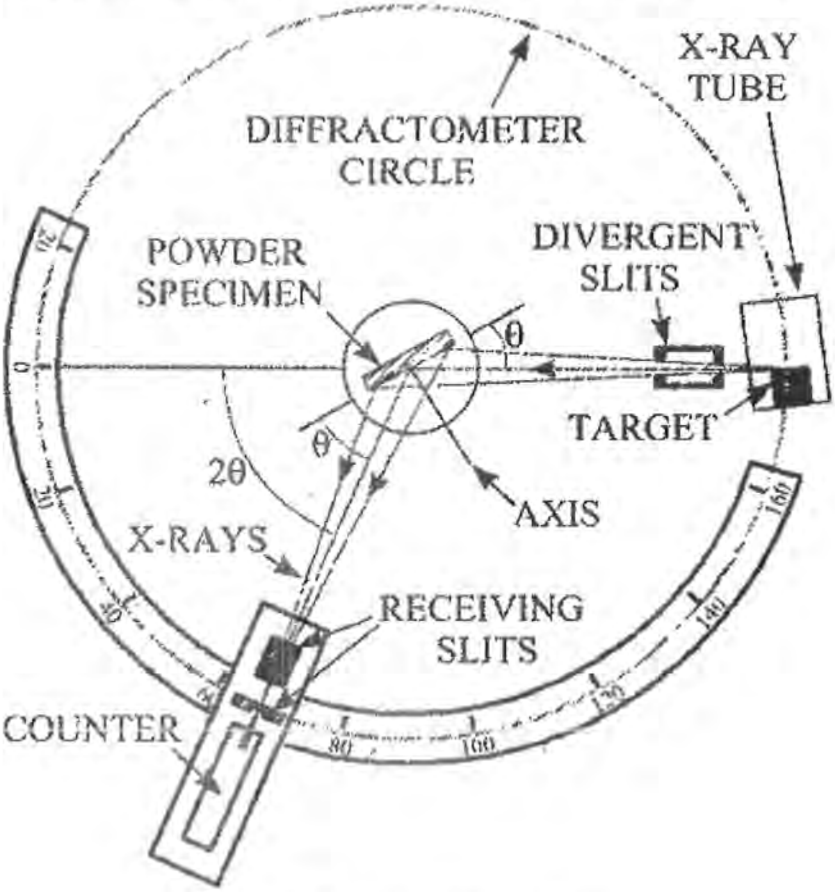

Fig. 3.2: Diffractometer

B) Four Probe Method For Resistivity:

Ohm-meter measurements are normally made with just a two-point measurement method (one probe on each of the two resistor leads). However, when measuring very small resistances, in the milli- or micro-ohm range, the two-point method is not satisfactory because test contact resistance becomes a significant factor. The lead resistance, due to long lead length, will affect the measurement results. The four-point resistance measurement method eliminates lead resistance or contact resistances [6].

One of the most striking features about the cuprate superconductors is the behavior of the resistivity of the normal state that is found above the transition temperature of the optimally doped materials. Before we look at the resistivity of the high T_c compounds, it will be instructive to first review the properties of the resistance of normal metals. In normal metals, the resistance takes on the form

$$\rho = \rho_{res} + AT^2 + \rho_{ph} \qquad (3.2)$$

ρ_{res} is a temperature independent resistivity due to impurity scattering. The T^2 term arises due to electron-electron scattering. At a temperatures T, the density of final states will include scattering off of the empty quasi-particle states found within K_bT of the Fermi surface [7]. This leads to the T^2 dependence, which we expect to see in systems with strong electron-electron scattering. The last term is the phonon contribution.

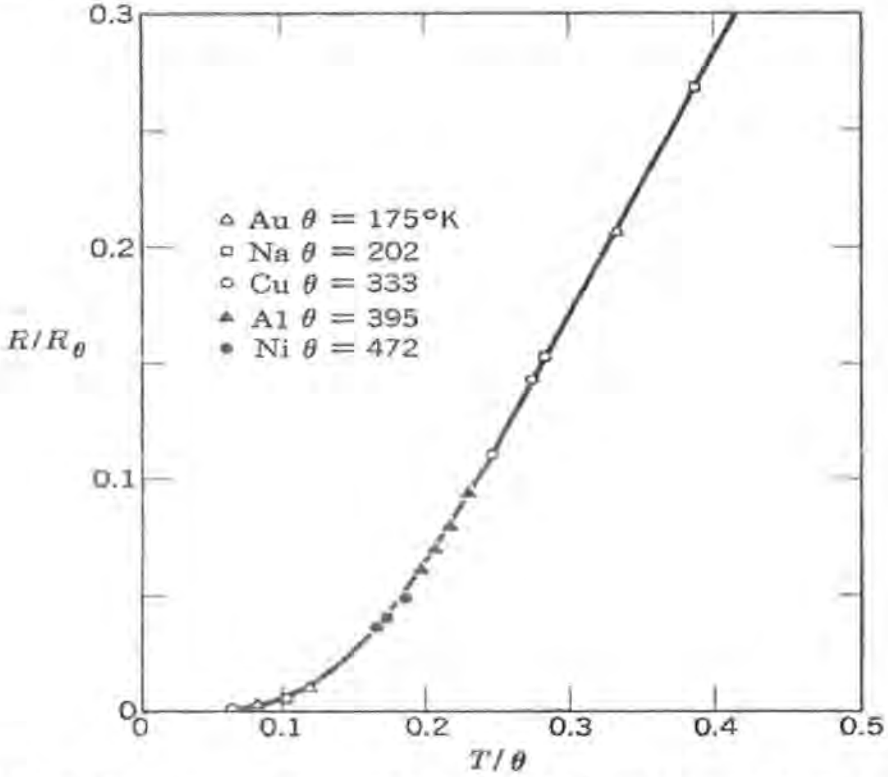

Fig. 3.3: The phonon contribution to the resistivity in normal metals. µ is the Debye temperature.

The temperature dependence of the phonon contribution is shown is Fig. 3.3. For $T < \mu_D$, there is a contribution ρ_{ph} œ T^5. The strong suppression at low temperatures is due to the low thermal occupation of the phonon modes and the fact that at low temperatures, phonon scattering is strongly peaked in the forward direction due to the presence of the Fermi surface. For temperature $T > \mu_D$, the contribution is ρ_{ph} œ T, since the thermal occupation of the phonon modes is linear in T at high temperatures. Generally, it is found that non linear behavior begins around T œ 0.3 μ_D, and becomes sub linear [8].

The resistance of any substance can be measured by using Ohm's law. The Ohm law states that potential across a conductor is directly proportional to the current flowing through the conductor provided the temperature remains the same. So we can measure the resistance of a conductor if we can measure the current through it and potential across it, by using $R = V/I$

Where V is the applied voltage and 'I' is the current flowing through the circuit and R is the resistance offered by the conductor to the moving electrons that constitute the current. Experiments have shown that the resistance of the conductor also depends upon the geometry of the conductor along with the temperature. If 'L' is the length of a certain conductor and 'A' is the area of cross section of it, then we can write that

$$R \; \alpha \; \frac{L}{A}$$

$$\Rightarrow \quad R = \rho \frac{L}{A}$$

The resistivity of a material depends upon the temperature as discussed earlier. So the temperature dependent resistivity in terms of Ohm's law can be written as

$$\rho(T) = \frac{A}{L} R$$

$$\rho(T) = \frac{A}{L} \frac{V}{I} \qquad (3.3)$$

The SI unit of the resistivity is Ω-cm. Resistivity of the superconducting materials is measured using the four-probe method.

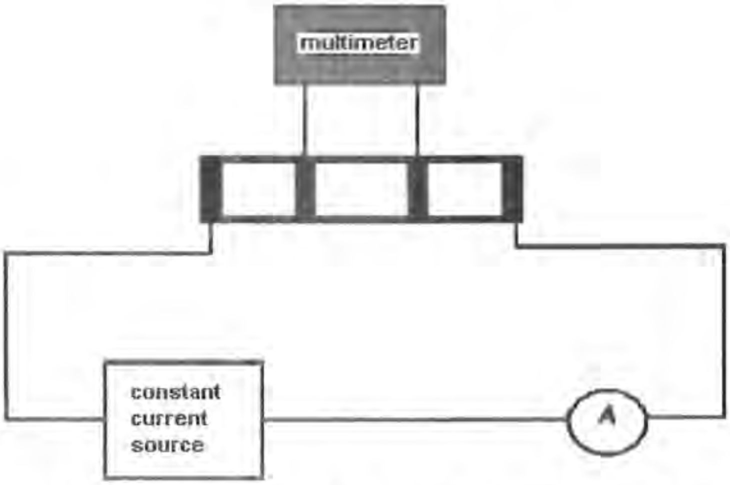

Fig. 3.4: Arrangement for resistivity measurements.

This method is used for measurements of resistivity in metals, semiconductors and superconductors around the world. Fig. 3.4 shows the experimental arrangement for four-probe method. The wire contacts with samples were made by silver paste on the surface. The outer leads were used to supply current and the resulting voltage drop was measured across the middle contacts. A home made cryostat is used for cooling the samples down to 77 K. The temperature of the samples is measured by a thermocouple. These measurements were done using high resolution multimetres.

C) Infrared Spectroscopy:

Infrared (IR) spectroscopy is one of the most common spectroscopic techniques used by organic and inorganic chemists. Simply, it is the absorption measurement of different IR frequencies by a sample positioned in the path of an IR beam. Infrared radiation spans a section of the electromagnetic spectrum having wave numbers from roughly 13,000 to 10 cm^{-1}, or wavelengths from 0.78 to 1000 μm. It is bound by the red end of the visible region at high frequencies and the microwave region at low frequencies. IR absorption positions are generally presented as either wave numbers (cm^{-1}) or wavelengths (λ). Wave number defines the number of waves per unit length. Thus, wave numbers are directly proportional to frequency, as well as the energy of the IR absorption. The wave number unit (cm^{-1}, reciprocal centimeter) is more commonly used in modern IR instruments that are linear in the cm^{-1} scale. In the contrast, wavelengths are inversely proportional to frequencies and their associated energy. At present, the recommended unit of wavelength is μm (micrometers). Wave numbers and wavelengths can be interconverted using the following equation:

$$u\ (cm^{-1}) = [1 / \lambda(\text{in } \mu m)] * 10^4 \qquad (3.4)$$

IR absorption information is generally presented in the form of a spectrum with wavelength or wave number on the x-axis and absorption intensity or percent transmittance on the y-axis. Transmittance "T" is the ratio of radiant power transmitted by the sample (I) to the radiant power incident on the sample (I_0). Absorbance (A) is the logarithm to the base 10 of the reciprocal of the transmittance (T).

$$A = \log_{10}(1/T) = -\log_{10}T = -\log_{10}(I/I_0) \quad (3.5)$$

The transmittance spectra provide better contrast between intensities of strong and weak bands because transmittance ranges from 0 to 100% T whereas absorbance ranges from infinity to zero.

Theory Of Infrared Absorption:

At temperatures above absolute zero, all the atoms in molecules are in continuous vibration with respect to each other. When the frequency of a specific vibration is equal to the frequency of the IR radiation directed on the molecule, the molecule absorbs the radiation. Each atom has three degrees of freedom, corresponding to motions along any of the three Cartesian coordinate axes (x, y, z). A polyatomic molecule of n atoms has $3n$ total degrees of freedom. However, 3 degrees of freedom are required to describe translation, the motion of the entire molecule through space. Additionally, 3 degrees of freedom correspond to rotation of the entire molecule. Therefore, the remaining $3n - 6$ degrees of freedom are true, fundamental vibrations for nonlinear molecules. Linear molecules possess 3n–5 fundamental vibrational modes because only 2 degrees of freedom are sufficient to describe rotation. Among the 3n–6 or 3n–5 fundamental vibrations (also known as normal modes of vibration), those that produce a net change in the dipole moment may result in an IR activity and those that give polarizability changes may give rise to Raman activity. Naturally, some vibrations can be both IR- and Raman-active.

The total number of observed absorption bands is generally different from the total number of fundamental vibrations. It is reduced because some modes are not IR active and a single frequency can cause more than one mode of motion to occur. Conversely, additional bands are generated by the appearance of overtones (integral multiples of the fundamental absorption frequencies), combinations of fundamental frequencies, and differences of fundamental frequencies, coupling interactions of two fundamental absorption frequencies, and coupling interactions between fundamental vibrations and overtones or combination bands. The intensities of overtone, combination, and difference bands are less than those of the fundamental bands. The combination and blending of all the factors thus create a unique IR spectrum for each compound.

The major types of molecular vibrations are stretching and bending. Infrared radiation is absorbed and the associated energy is converted into these types of motions. The absorption involves discrete, quantized energy levels. However, the individual vibrational motion is usually accompanied by other rotational motions. These combinations lead to the absorption bands, not the discrete lines, commonly observed in the mid IR region.

Spectrometer Components:

There are three basic spectrometer components in an FTIR system: radiation source, interferometer, and detector. A simplified optical layout of a typical FTIR spectrometer is illustrated in Figure. 3.5

The most commonly used interferometer is a Michelson interferometer. It consists of three active components: a moving mirror, a fixed mirror, and a beam-splitter (Figure. 3.5). The two mirrors are perpendicular to each other. The beam-splitter is a semi-reflecting device and is often made by depositing a thin film of germanium onto a flat KBr substrate. Radiation from the broadband IR source is collimated and directed into the interferometer, and impinges on the beam-splitter. At the beam-splitter, half the IR beam is transmitted to the fixed mirror and the remaining half is reflected to the moving mirror. After the divided beams are reflected from the two mirrors, they are recombined at the beam-splitter. Due to changes in the relative position of the moving mirror to the fixed mirror, an interference pattern is generated. The resulting beam then passes through the sample and is eventually focused on the detector.

For an easier explanation, the detector response for a single-frequency component from the IR source is first considered. This simulates an idealized situation where the source is monochromatic, such as a laser source. As previously described, differences in the optical paths between the two split beams are created by varying the relative position of moving mirror to the fixed mirror. If the two arms of the interferometer are of equal length, the two split beams travel through the exact same path length. The two beams are totally in phase with each other thus, they interfere constructively and lead to a maximum in the detector response. This position of the moving mirror is called the point of zero path difference (ZPD). When the moving mirror travels in either direction by the distance $\lambda/4$, the optical path (beam splitter–mirror–beam splitter) is changed by 2 ($\lambda/4$), or $\lambda/2$. The two beams are 180° out of phase with each other, and thus interfere destructively. As the moving mirror travels another $\lambda/4$, the optical path difference is now 2 ($\lambda/2$), or λ. The two beams are again in phase with each other and result in another constructive interference [9]. The sample absorbs this frequency; the amplitude of the sinusoidal wave is reduced by an amount proportional to the amount of sample in the beam.

The interferogram contains information over the entire IR region to which the detector responds. Figure.3.5 shows a simplified optical layout of a typical FTIR spectrometer. A mathematical operation known as Fourier transformation converts the interferogram (a time domain spectrum displaying intensity versus time within the mirror scan) to the final IR spectrum, which is the familiar frequency domain spectrum showing intensity versus frequency. This also explains how the term Fourier transform infrared spectrometry is created. The greatest amplitude occurs at the point of zero path difference (ZPD).

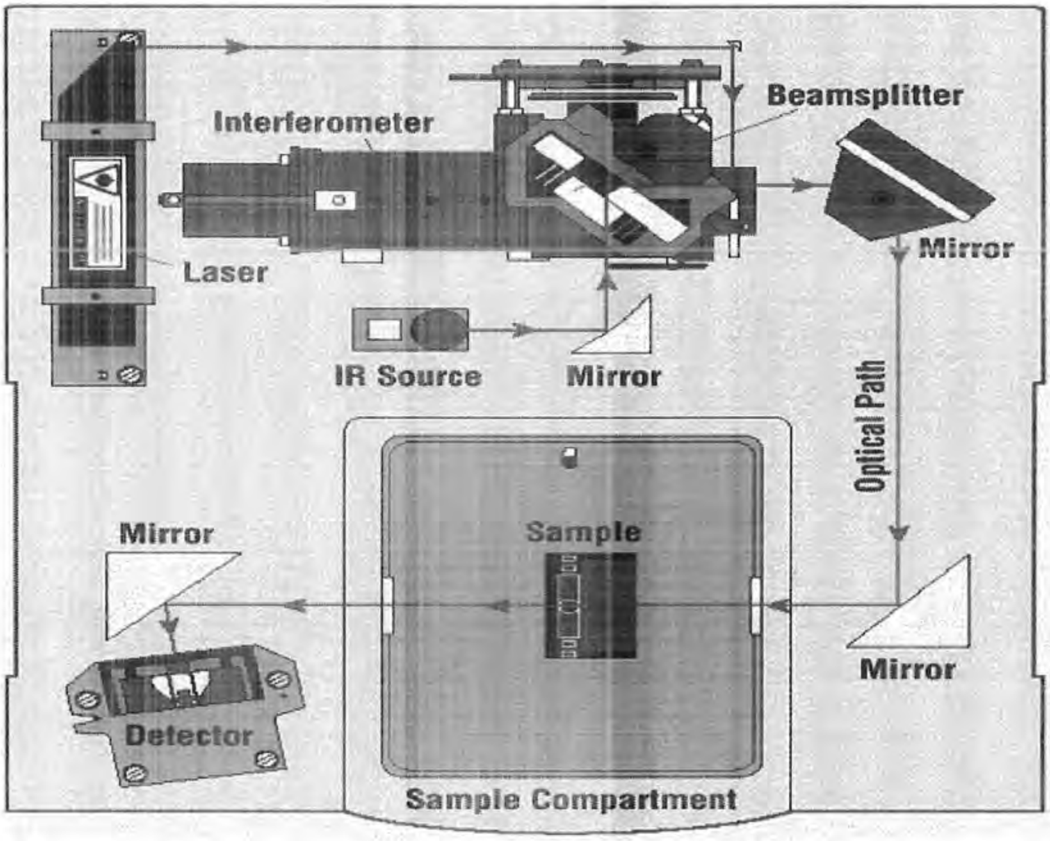

Fig. 3.5: Simplified optical layout of a typical FTIR spectrometer.

When the mirror is moved at a constant velocity, the intensity of radiation reaching the detector varies in a sinusoidal manner to produce the interferogram output. The interferogram is the record of the interference signal. It is actually a time domain spectrum and records the detector response changes versus time within the mirror scan.

Procedure:

A typical operating procedure is described as follows:

1. A background spectrum is first obtained by collecting an interferogram (raw data), followed by processing the data by Fourier transform conversion. This is a response curve of the spectrometer and takes account of the combined performance of source, interferometer, and detector. The background spectrum also includes the contribution from any ambient water (two irregular groups of lines at about 3600cm^{-1} and about 1600cm^{-1}) and carbon dioxide (doublet at 2360cm^{-1} and sharp spike at 667cm^{-1}) present in the optical bench.

2. Next, a single-beam sample spectrum is collected. It contains absorption bands from the sample and the background (air or solvent).

3. The ratio of the single-beam sample spectrum against the single beam background spectrum results in a “double-beam” spectrum of the sample.

Almost any solid, liquid or gas sample can be analyzed. Many sampling accessories are available. 10 µg solid grounded with transparent matrix (such as KBr) is the minimum for qualitative determinations. Little or no preparation is required; may have to grind solid into KBr. Estimated time to obtain spectrum from a routine sample varies from 1 to 10 min depending on the type of instrument and the resolution required. Most samples can be prepared for infrared (IR) analysis in 1 to 5 minutes approximately [10].

To reduce the strong background absorption from water and carbon dioxide in the atmosphere, the optical bench is usually purged with an inert gas or with dry, carbon dioxide–scrubbed air (from a commercial purge gas generator). Spectrometer alignment, which includes optimization of the beam splitter angle, is recommended as part of a periodic maintenance or when a sample is changed.

Copper oxide superconductors exhibit the highest critical temperature found so far. Since their discovery in 1986, the microscopic mechanism at the origin of their superconductivity is still unexplained [11]. While it is well established that in conventional superconductors the coupling between electrons and phonons (collective vibrations) leads to charge carrier pairing, and therefore superconductivity, the role of this coupling in copper-oxide superconducting compounds is still the subject of intense research efforts. There is a strong coupling between the lattice vibrations and the charge carriers as the conduction in the copper oxide superconductors takes place by charge hopping along the Cu-O bond in the CuO_2 planes. Within this framework, the optical phonon anomaly is expected to be ubiquitous and therefore should also be observed in electron-doped copper oxide superconductors [12].

D) AC Magnetic Susceptibility:

AC magnetic susceptibility has been one of the subjects of interest in the investigation of the new ceramic superconductivity. During the past, many efforts have been devoted to the study of various properties and the phase structure of these cuprate superconductors. It was believed that the magnetic susceptibility of the ceramic superconductors is a measure of the characteristics of the coupling status of the materials. These characteristics refer to how the weak-links, Josephson junctions and grain boundaries affect the magnetic properties of the bulk materials. When a high-T_c ceramic superconductor is placed under an external field, a certain configuration of superconducting loops will be established inside the superconductor. Owing to the granular structure of the ceramic material, the situation of the configuration of the superconducting loops inside the granular structured superconductor is in general very complicated. The superconducting loops are formed as an assembly with a certain distribution in inductance, critical current and orientation $\cos\theta$, where θ is the angle between the normal to the loop and the direction of the applied field [13].

Susceptometer:

The sample magnetization is studied using a conventional AC magnetic susceptometer. The susceptometer probe illustrated in Fig. 3.6 includes a primary (excitation) solenoid coil which produces a near-uniform AC magnetic field when driven by an AC source [14]. Inside the primary coil is the secondary coil consisting of two pickup coils which are wound in opposite directions and electrically connected in series. The pickup coils occupy opposite halves of the primary coil volume. The sample is placed in one of the pickup coils (the sample coil) while the other pickup coil (the reference coil) is left empty. The AC voltage V across the secondary coil is due to Faraday induction.

$$V = d\Phi / dt \qquad (3.6)$$

Where dΦ is the net flux through the entire secondary (both the sample and reference coil) and includes contributions from both the applied field and the field due to the sample magnetization. The self-induced flux from the secondary can be neglected because the secondary is connected only to high impedance (10 MΩ) voltage metering equipment (oscilloscope, lock-in) and thus carries negligible current. Because the two pickup coils are wound in opposite directions and connected in series, the net secondary flux due to the applied field will be small. It is not exactly zero because of imperfections in probe construction, and thus there is some small mismatch in the flux for the sample and reference coils.

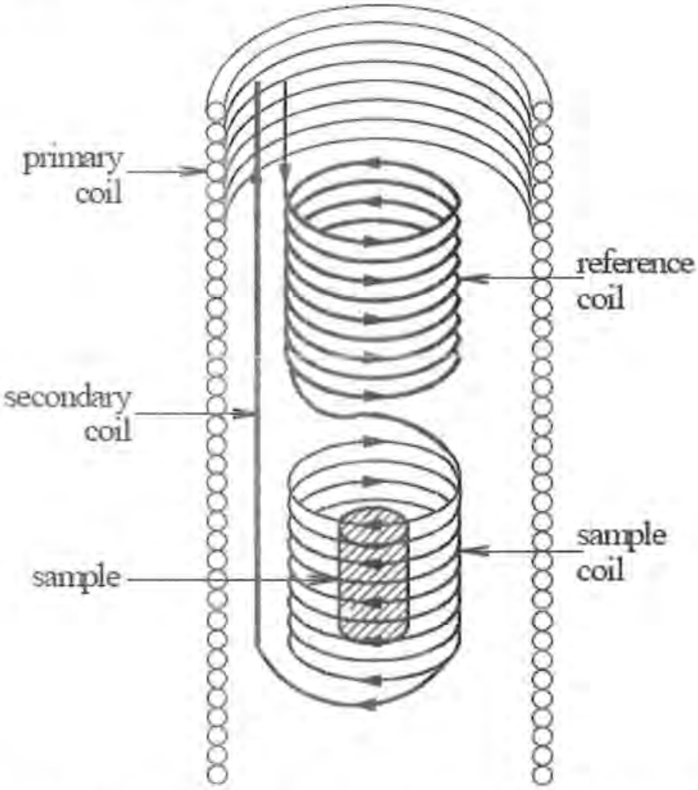

Fig.3.6: Arrangement of the primary coil (cut away), the secondary coil, and the sample in the susceptometer.

If a sample is present (in the sample coil), the magnetic field $\mu_0 M$ associated with the induced magnetization will unbalance the fluxes in the sample and reference coils and there will be a large net flux Φm in the secondary [15].

References:

1. B. D. Cullity, Elements of X-ray Diffraction, second edition, (Addison - Wesley Publishing company, Inc. London, 1977).
2. C. Giacovazzo, Fundamentals of Crystallography, second edition, (Oxford science publications, 2002).
3. Allen M. Hermann, Thallium-Based High-Temperature Superconductors, Marcel Dekker, Inc. (1994) p 41.
4. B. E. Warren, X-ray Diffraction, (General publishing company, 1969).
5. P. Harold, X-ray diffraction procedures for polycrystalline and Amorphous materials, second edition (Jhon-Wiley, 1977).
6. Harald Ibach, and Hans Luth, Solid State Physics: An Introduction to Theory and Experiment (Springer-Verleg, 1991).
7. E. Ruckenstein and C. T. Cheung, J. Mater. Res. 4 (1989) 1116
8. E. Ruckenstein and S. Narain Mater. Lett. 8 (1989) 421
9. N. P. Ong, R. J. Cava Science 305 (2004) 52
10. B. D. Cullity, Element of X-ray Diffraction, second edition, (Addision-Wesely Publishing company, Inc. London (1977).
11. M. Ali Omer Elementary Solid State Physics, First Edition, Wesely Publishing Company (1974)
12. N. Ashcroft, N. Mermin (1976) Solid State Physics (Orlando, FL: Saunders) 31 pp346
13. H. Guo Physica C 247 (1995) 115-124
14. Q. Li, M. Suenaga, T. Kaneko, K. Sato, and Ch. Simmon Appl. Phys. Lett. 71 (1997) 1561.
15. AC Susceptibility Measurements in High-Tc Superconductors Experiment ACS University of Florida Department of Physics PHY4803L Advanced Physics Laboratory

RESULTS AND DISCUSSION

4.1 Introduction:

The $Cu_{0.5}Tl_{0.5}Ba_2Ca_2Cu_3O_{10-\delta}$ has shown lowest an-isotropy in Tl-based families of high temperature superconductors [1,2]. The an-isotropy given by a dimensionless parameter $\gamma=(\xi_{ab}/\xi_c)$ in the oxides superconductor is related to underlying mechanism of superconductivity and a decrease in the value of it improves the superconducting properties of the final compound. A decreases in γ in previous studies has been found to increase the zero resistivity critical temperature [$T_c(R=0)$], the magnitude of diamagnetism and critical current density J_c (H) [3]. The isotropic superconductors are simpler because a symmetric wave function (s-wave type) assigned to the carriers bring superconductivity in the final compound. It is therefore advisable to have a superconductor with low an-isotropy because the shape of the Fermi surface in such superconductors would be less intricate [4,5]. In an-isotropic superconductors, during the transport of the carriers under Lorentz force the wave function of the carriers had distinct values in various directions of unit cell which can initiates an-harmonic conductivity process marginalizing the superconducting properties of the final compound [6]. The tetragonal crystal chemistry of $Cu_{1-x}Tl_xBa_2Ca_2Cu_3O_{10-\delta}$ superconductor tells that the compound has $Cu_{1-x}Tl_xBa_2O_{4-\delta}$ charge reservoir layer and three asymmetric CuO_2 planes which are separated by Ca atom [7]. Two out of three CuO_2 planes (i.e. outer-planes) OP are identical and are connected with $Cu_{1-x}Tl_xBa_2O_{4-\delta}$ charge reservoir layer via apical oxygen atoms whereas the third inner CuO_2 plane(i.e. IP) is dissimilar from former two due to its different neighbouring atmosphere. The OP-planes due to their immediate connectivity with the charge reservoir layer are over-doped with carriers whereas the IP-plane has under-doped carrier concentration [8]. The under-doped CuO_2 plane had Cu atoms with anti-ferromagnetic alignment of the spins. The existence of a CuO_2 plane (IP) with anti-ferromagnetic aligned Cu atoms lowers the density of carriers which marginalize the overall superconducting properties of $Cu_{1-x}Tl_xBa_2Ca_2Cu_3O_{10-\delta}$. Calcium atoms separating the OP and IP have predominantly a fixed oxidation (+2) and therefore cannot modify the spin state of the neighbouring Cu atoms of the CuO_2 planes. It is suggested (and also verified experimentally) that in a superconductor an-isotropy decreases with increased number of CuO_2 planes [9]. In these superconductors, the charge reservoir layers supply carriers to superconducting CuO_2 planes and these free carriers (electrons/holes) bring about superconductivity [10]. To decrease superconductor an-isotropy we need to decrease the c-axis length [11]. The decreased c-axis length somehow enhances coherence length of carriers along the c-axis and the Fermi velocity [9]. One way of decreasing the c-axis length is to substitute Ca with smaller size atoms. The smaller sized atoms, somehow, develop a better inter-plane coordination and superconducting properties are expected to be enhanced. Mg atom had successfully substituted Ca atom and the critical current density was enhanced by two orders of magnitude [12]. In the present studies we have substituted Mn at the Ca site, the ionic radius of Mn is even smaller then Mg atoms.

The transition metal such as Mn may exist in multiple oxidation states (+2, +3, +4, +5, +6 etc) and if doped at the Ca sites would modify the immediate neighbouring atmosphere of it [13,14,15]. The main objective of this substitution is to enhance the chemical pressure and increase the inter-plane coupling. In previous studies we have enhanced the inter-plane coupling by substituting smaller sized Be [16] and Mg [12] atoms at the Ca sites, these atoms have a fixed oxidation state (i.e. +2). It is most likely that doped Mn atoms would modify the charge state of neighbouring Cu atoms in the CuO_2 planes and hence their spin state as well.

4.2 As-prepared $Cu_{0.5}Tl_{0.5}Ba_2(Ca_{2-y}Mn_y)Cu_3O_{10-\delta}$ (y=0, 0.15, 0.25, 0.35, 0.5, 0.75, 1.0) samples:

The resistivity measurements of $Cu_{0.5}Tl_{0.5}Ba_2(Ca_{2-y}Mn_y)Cu_3O_{10-\delta}$ (y=0, 0.15, 0.25, 0.35, 0.5, 0.75, 1.0) samples are shown in Fig. 4.1(a,b). A metallic variation of resistivity from room temperature down to onset of superconductivity is a salient feature of all these samples. The room temperature resistivity in these samples varies from 0.075 to 0.155Ω-cm. The transition onset and zero resistivity critical temperature as a function of Mn-doping concentration are plotted in Fig. 4.2(a,b). The onset temperature of superconductivity T_c(onset) and zero resistivity critical temperature [T_c(R=0)] systematically are suppressed with increased Mn doping. $Cu_{0.5}Tl_{0.5}Ba_2(Ca_{2-y}Mn_y)Cu_3O_{10-\delta}$ samples with Mn doping of y=(0, 0.15, 0.25, 0.35, 0.5, 0.75 1.0) have shown T_c(R=0) around 98, 98, 95.5, 92.4, 96.5, 91.3, 91.3K, respectively.

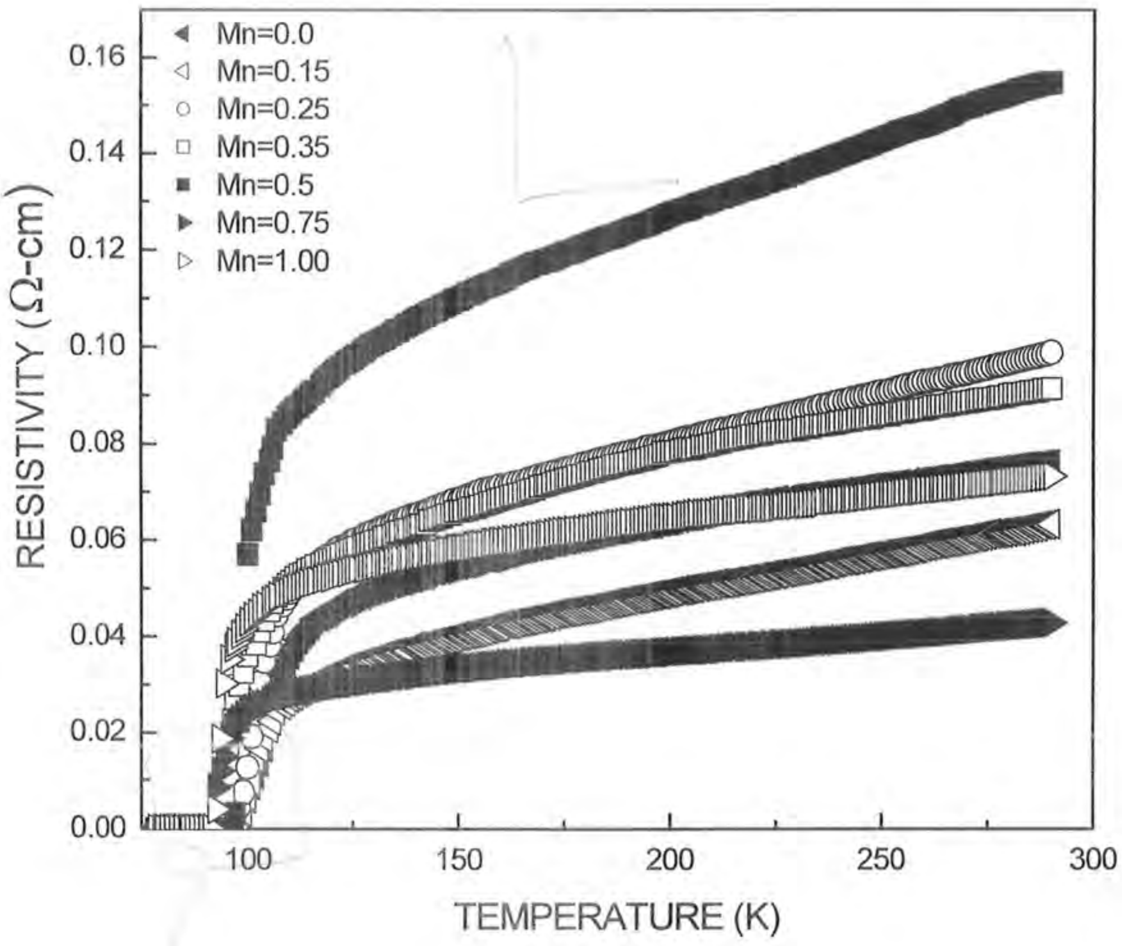

Fig. 4.1a: Resistivity curves of air annealed $(Cu_{0.5}Tl_{0.5})Ba_2(Ca_{2-y}Mn_y)Cu_3O_{10-\delta}$ (y=0.00, 0.15, 0.25, 0.35, 0.50, 0.75, 1.00) superconductors.

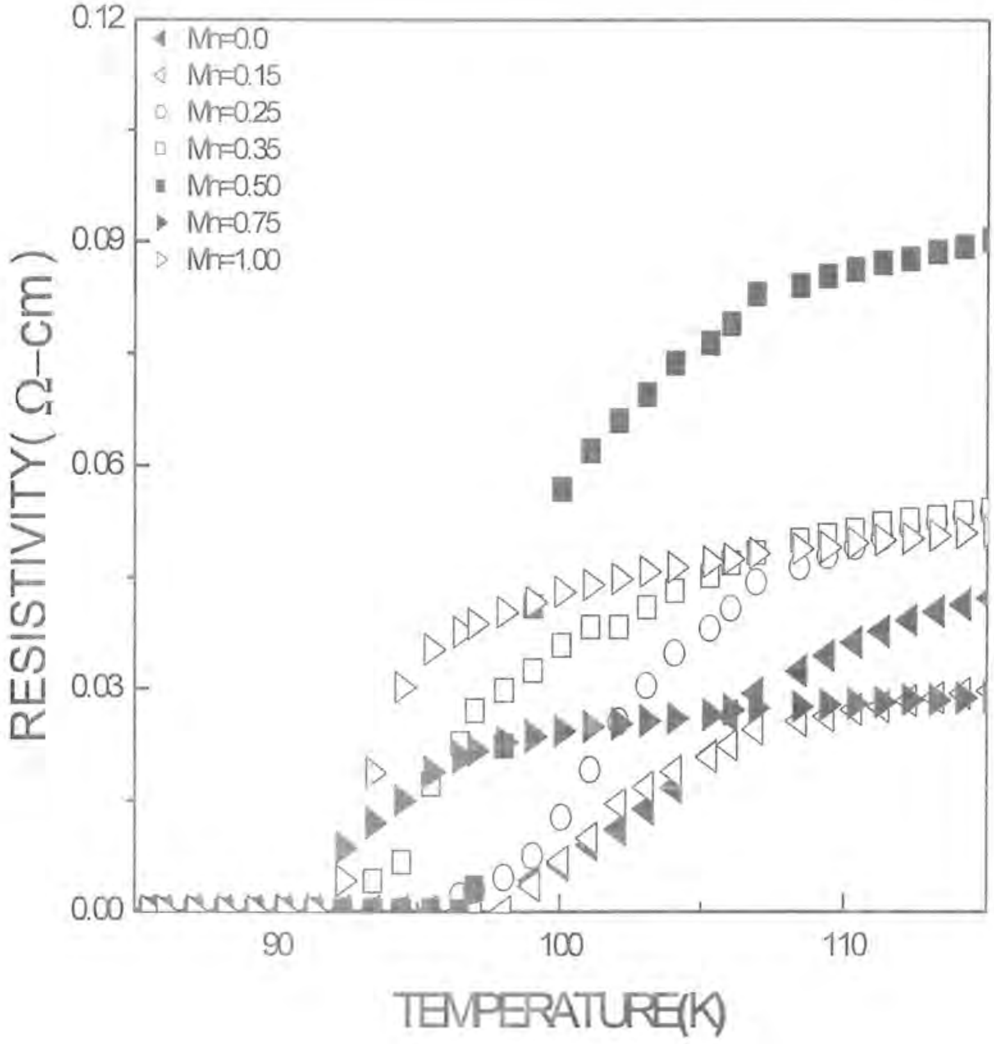

Fig. 4.1b: Transition region of resistivity of air annealed $(Cu_{0.5}Tl_{0.5})Ba_2(Ca_{2-y}Mn_y)Cu_3O_{10-\delta}$ (y=0.00, 0.15, 0.25, 0.35, 0.50, 0.75, 1.00) superconductors.

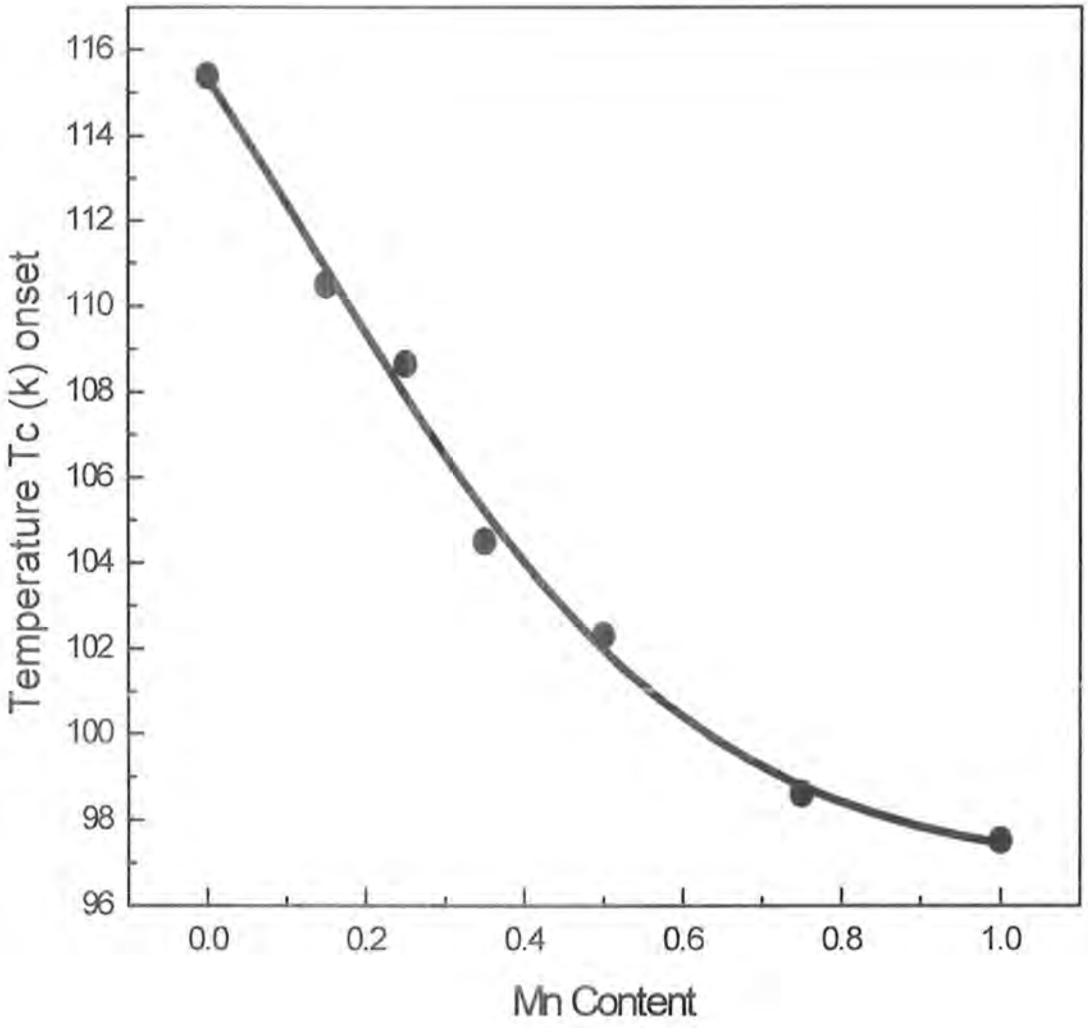

Fig. 4.2a: The transition onset temperature as a function of Mn-doping concentration for air annealed $(Cu_{0.5}Tl_{0.5})Ba_2(Ca_{2-y}Mn_y)Cu_3O_{10-\delta}$ (y=0.00, 0.15, 0.25, 0.35, 0.50, 0.75, 1.00) superconductors.

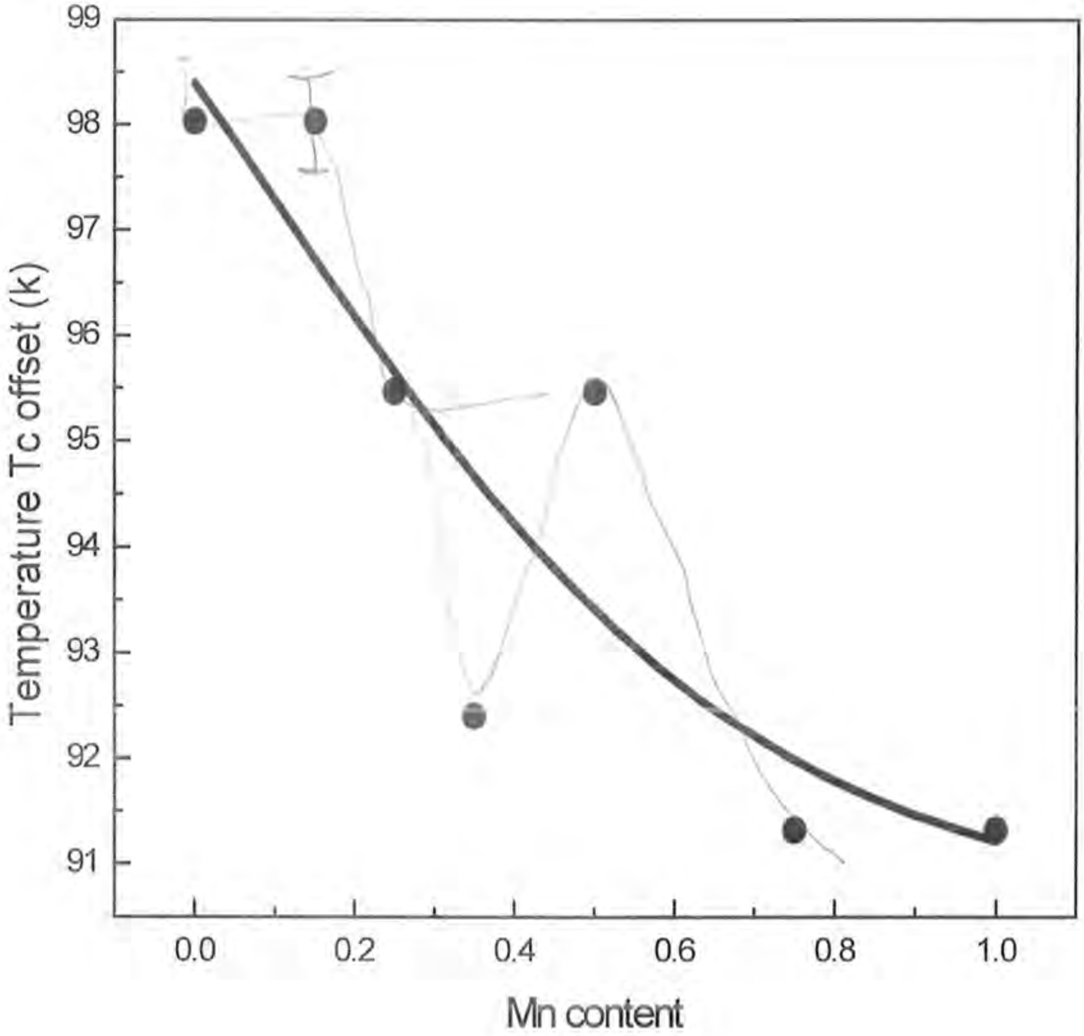

Fig. 4.2b: The zero resistivity critical temperature as a function of Mn doping for air-annealed $(Cu_{0.5}Tl_{0.5})Ba_2(Ca_{2-y}Mn_y)Cu_3O_{10-\delta}$ (y=0.00, 0.15, 0.25,0.35, 0.50, 0.75, 1.00) superconductors.

The AC-susceptibility measurements of $Cu_{0.5}Tl_{0.5}Ba_2(Ca_{2-y}Mn_y)Cu_3O_{10-\delta}$ (y=0, 0.15, 0.25, 0.35, 0.5, 0.75, 1.0) samples are shown in Fig. 4.3(a,b). The magnitude of diamagnetism as a function of increased Mn-doping is shown in Fig. 4.4. It can be seen from this figure that the magnitude of diamagnetism initially increases for Mn-doping of y=0.15, 0.25 and then systematically decreases with increased incorporation of Mn in the final compound. A small increase in the magnitude of diamagnetism for Mn-doping of y=0.15, 0.25 is most likely associated with decreased anti-ferromagnetism triggered by uniform distribution of the carriers in the conducting CuO_2 planes which is most likely promoted by Mn-doping.

The FTIR absorption measurements of $Cu_{0.5}Tl_{0.5}Ba_2(Ca_{2-y}Mn_y)Cu_3O_{10-\delta}$ (y=0, 0.15, 0.25, 0.35, 0.5, 0.75 1.0) samples are shown in Fig. 4.5. In $(Cu_{0.5}Tl_{0.5})Ba_2Ca_2Cu_3O_{10-\delta}$ oxide superconductors, the vibration related to apical oxygen atoms are observed around 400-540cm^{-1}, due to CuO_2 planar oxygen atoms around 540-600cm^{-1} and the vibrations of O_δ atoms of $Cu_{0.5}Tl_{0.5}Ba_2O_{4-\delta}$ charge reservoir layer around 660-700cm^{-1} [17]. In Mn free $(Cu_{0.5}Tl_{0.5})Ba_2Ca_2Cu_3O_{10-\delta}$ samples the apical oxygen mode of the type Cu(1)-O_A-Cu(2) and Tl-O_A-Cu(2) are observed around 540cm^{-1} and 491cm^{-1}. The CuO_2 planar oxygen mode is observed around 572cm^{-1} and O_δ mode of oxygen atoms of $Cu_{1-x}Tl_xBa_2O_{4-\delta}$ charge reservoir layer around 694cm^{-1}. The intensity of apical oxygen mode of type Cu(1)-O_A-Cu(2) observed around 540cm^{-1} and O_δ mode of the charge reservoir layer decreases whereas that of CuO_2 planar mode of oxygen atoms observed around 572-580cm^{-1} which increases with the Mn-doping in (y=0, 0.15, 0.25, 0.35, 0.5, 0.75, 1.0) superconductors. The decrease in the intensity of O_δ mode of oxygen atoms of $Cu_{0.5}Tl_{0.5}Ba_2O_{4-\delta}$ charge reservoir layer around 690cm^{-1} showed that oxygen contents are decreased with increased doping of Mn in the final compound. The CuO_2 planar oxygen mode is systematically hardened with increased Mn-doping and are observed around 573.5, 575, 575, 577, 577 and 580cm^{-1} for the Mn doping of y=0.15, 0.25, 0.35, 0.5, 0.75, 1.0. The two apical oxygen modes of types Cu(1)-O_A-Cu(2) and Tl-O_A-Cu(2) behave differently i.e. the Cu(1)-O_A-Cu(2) mode is softened and Tl-O_A-Cu(2) mode is hardened with increased Mn-doping. The Cu(1)-O_A-Cu(2) mode is observed around 540, 539, 534.5, 534.5, 532, 530, 527.5cm^{-1} whereas Tl-O_A-Cu(2) mode is observed around 491, 491, 493, 493, 494, 502, 505.7cm^{-1} for the Mn-doping of y=0, 0.15, 0.25, 0.35, 0.5, 0.75, 1.0 in $Cu_{0.5}Tl_{0.5}Ba_2(Ca_{2-y}Mn_y)Cu_3O_{10-\delta}$. The softening and hardening of above mentioned modes is microscopic evidence of Mn incorporation in the final compound. The hardening of Tl-O_A-Cu(2) apical oxygen mode (with trivalent thallium atoms in the charge reservoir layer) indicates that the charge state of the Mn is different from +2 and is most likely more than +2. This is because any charge state of Mn more than +2 would enhance the attraction of Tl^{+3} atoms toward itself and hence promote a decrease in the bond length of apical oxygen atoms of Tl-O_A-Cu(2) making it hardened and vibrate at higher frequency. Since Mn can exist in multiple oxidation states (i.e. +2, +3, +4, +5, +6 etc) and therefore can localize the free carriers present in the neighbouring CuO_2 plane and suppress their density. The decrease concentration of the free carriers in conducting CuO_2 plane may promote increase in the anti-ferromagnetic alignments of copper spins. The increased population of anti-ferromagnetic aligned spins suppress the magnitude of superconductivity in final compound. Such effects have been observed in the form of decreased critical temperature and magnitude of diamagnetism in our Mn doped $Cu_{0.5}Tl_{0.5}Ba_2(Ca_{2-y}Mn_y)Cu_3O_{10-\delta}$ samples. In the samples with higher Mn-doping, the room temperature resistivity is significantly increased, the samples with Mn doping of $y \geq 1.25$ have been found to be totally insulating.

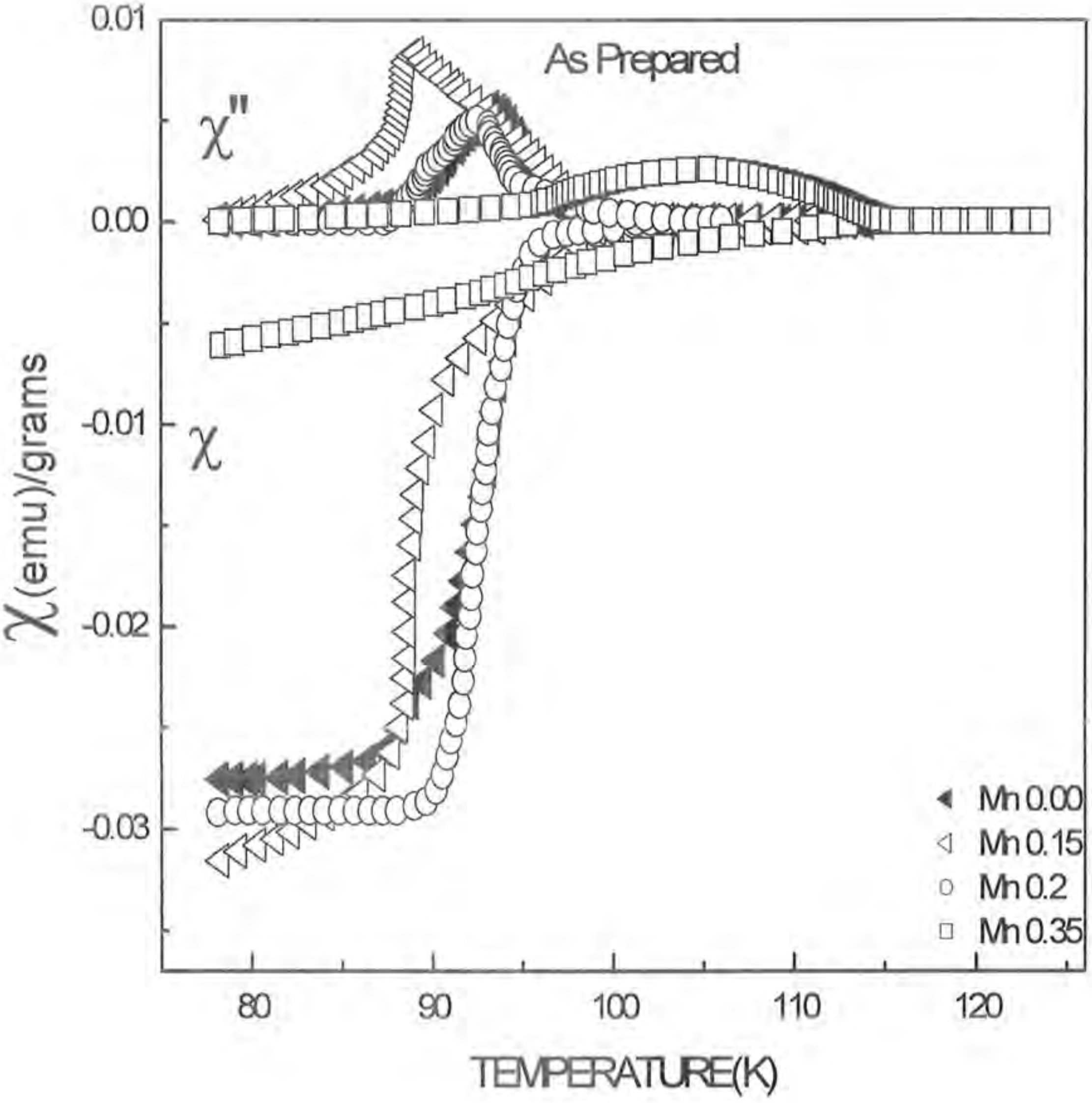

Fig. 4.3a: AC-susceptibility measurements of air annealed $(Cu_{0.5}Tl_{0.5})Ba_2(Ca_{2-y}Mn_y)Cu_3O_{10-\delta}$ (y=0.00, 0.15, 0.25, 0.35) superconductors.

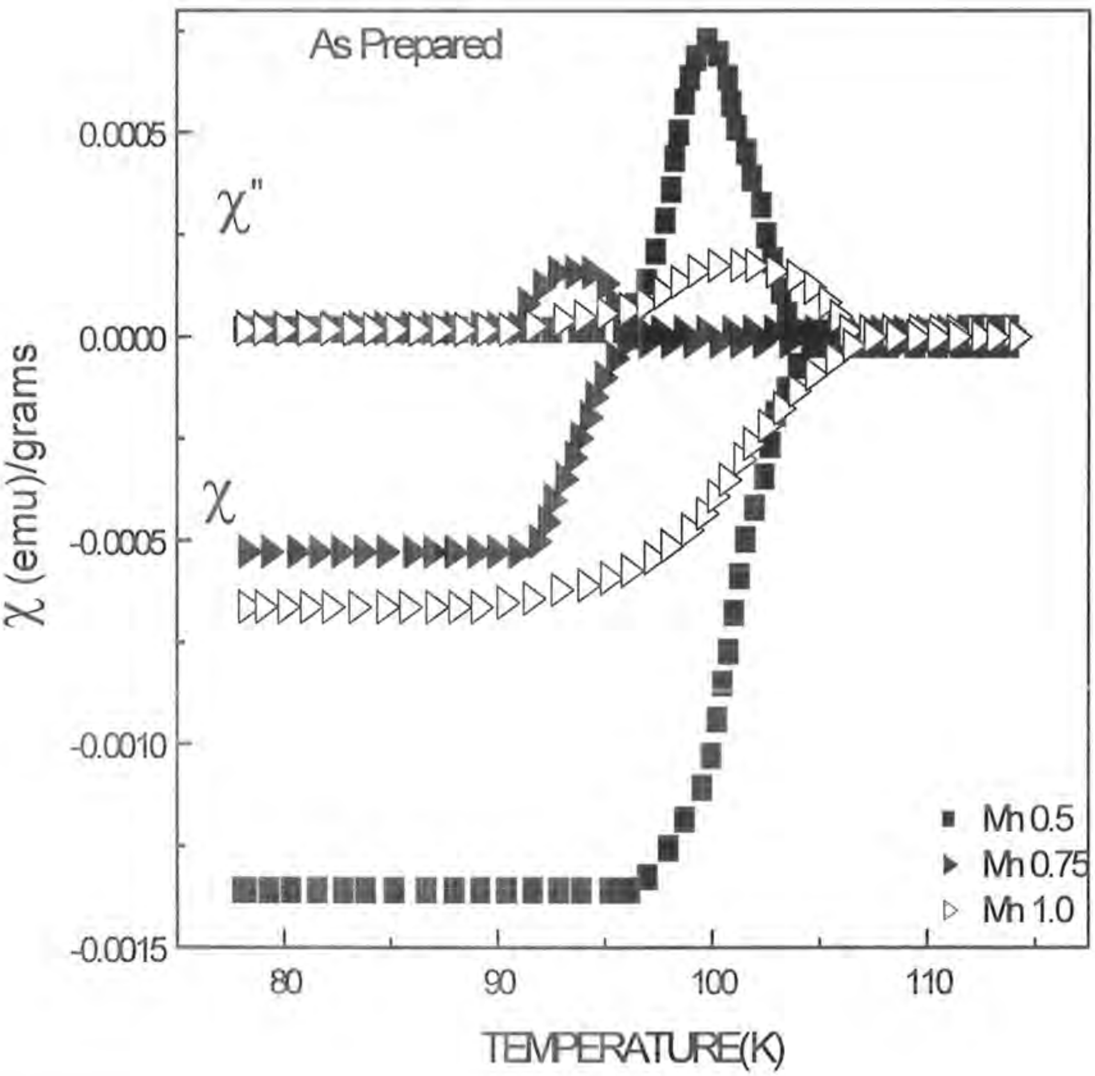

Fig. 4.3b: AC-susceptibility measurements of air annealed $(Cu_{0.5}Tl_{0.5})Ba_2(Ca_{2-y}Mn_y)Cu_3O_{10-\delta}$ (y= 0.50, 0.75, 1.00) superconductors.

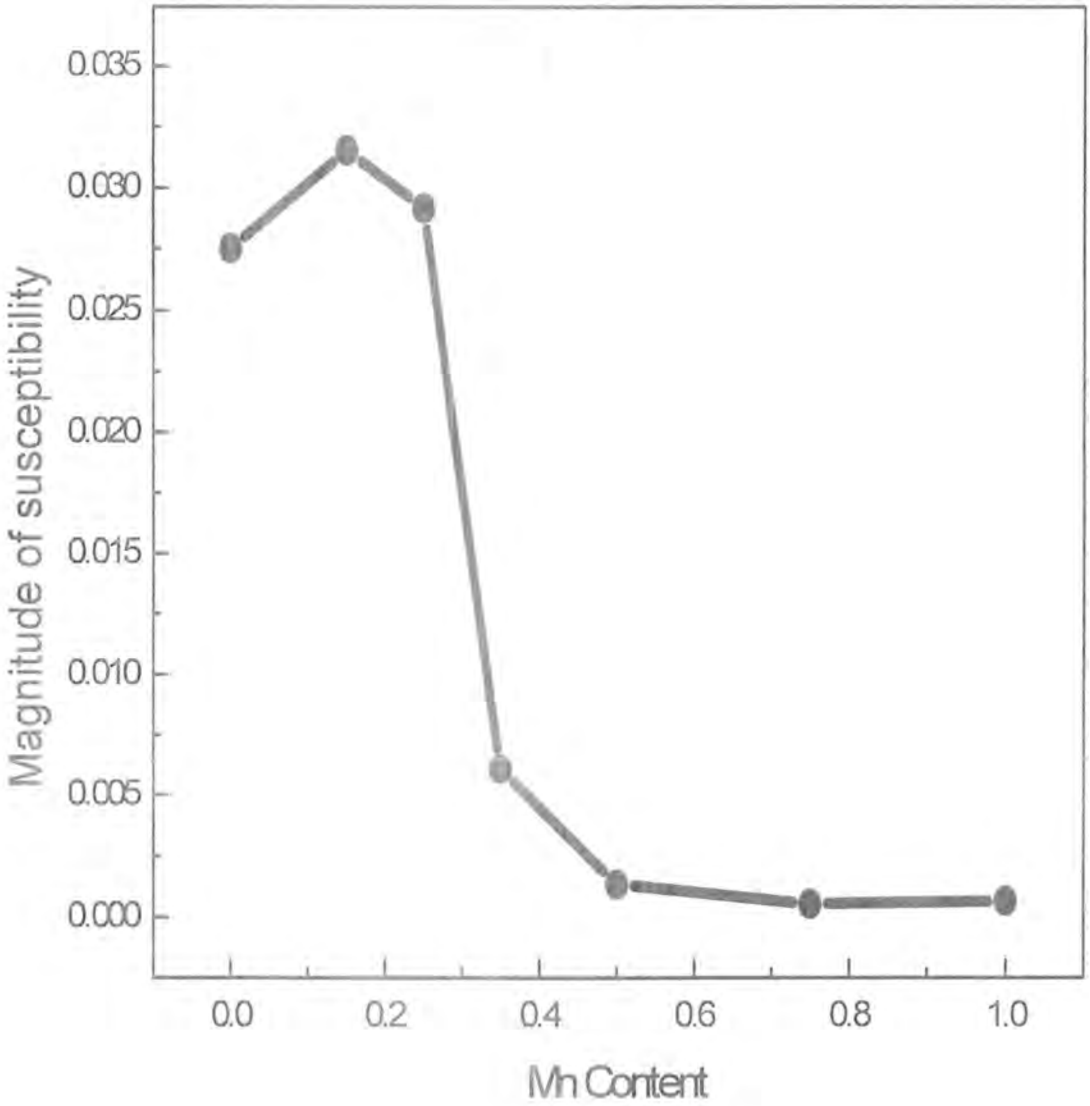

Fig. 4.4: The magnitude of diamagnetism as a function of Mn-doping concentration for $(Cu_{0.5}Tl_{0.5})Ba_2(Ca_{2-y}Mn_y)Cu_3O_{10-\delta}$ (y=0.00, 0.15, 0.25,0.35, 0.50, 0.75, 1.00) superconductors.

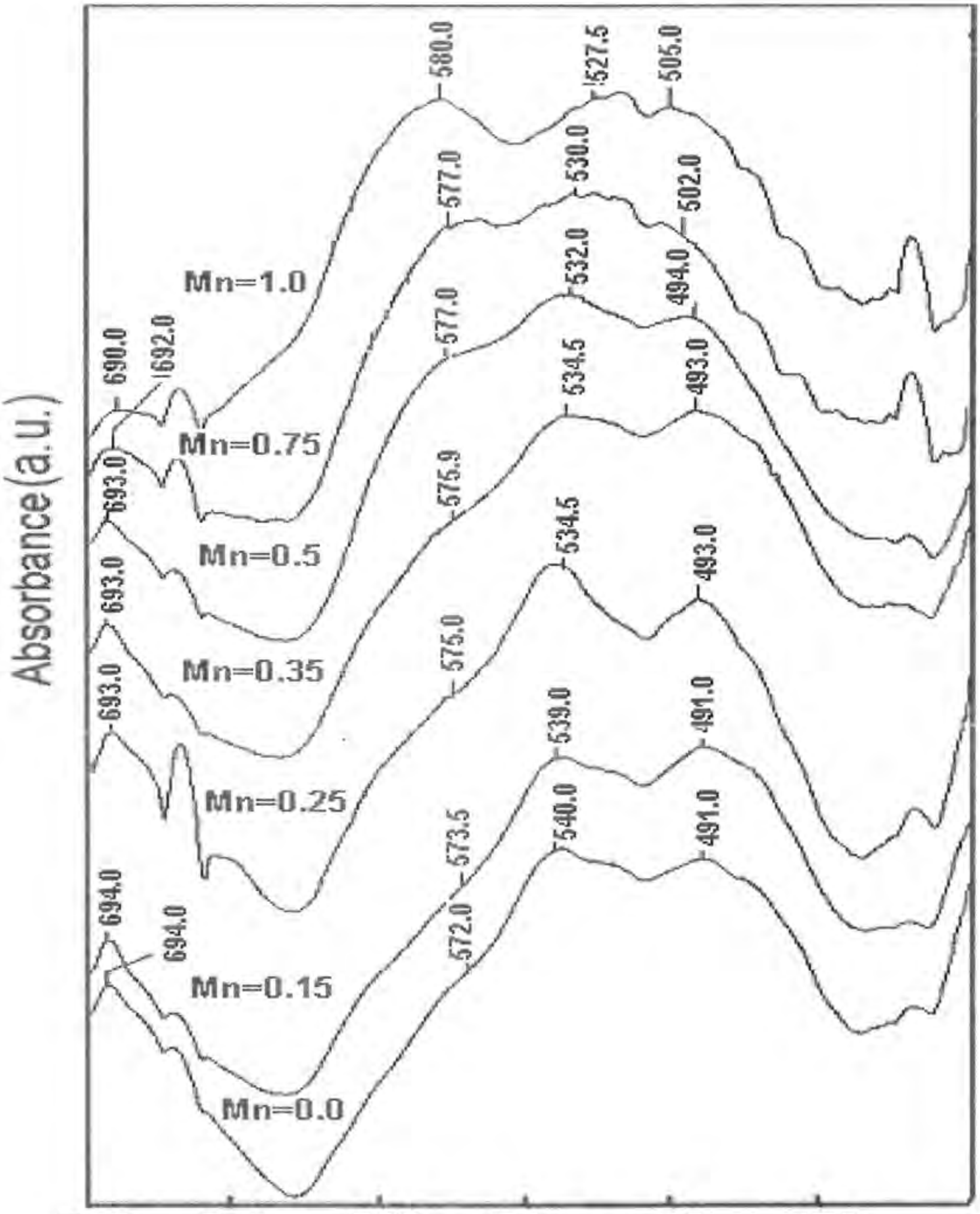

Fig. 4.5: Infrared absorption spectra of air annealed $(Cu_{0.5}Tl_{0.5})Ba_2(Ca_{2-y}Mn_y)Cu_3O_{10-\delta}$ (y= 0.00, 0.15, 0.25, 0.35, 0.50, 0.75, 1.00) superconductors.

The x-ray diffraction scans of $Cu_{0.5}Tl_{0.5}Ba_2(Ca_{2-y}Mn_y)Cu_3O_{10-\delta}$ (y= 0.25, 0.5, 0.75) samples are shown in Fig. 4.6. The planar reflections are fitted very well to the tetragonal structure following P4/mmm space group. The calculated cell parameters have shown a decrease in the length of cell parameters and volume of the unit cell with increased Mn-doping as shown in table 4.1 and in Fig. 4.7(a,b). The decrease in the cell parameters and volume of the unit cell is an evidence of incorporation of the Mn into the unit cell of the final compound. We can infer from these x-ray diffraction analyses that the charge state of Mn is more than +2 which exerts more chemical pressure than Ca atoms and suppress the volume of the unit cell.

Mn Content (y)	a (A°)	b (A°)	c (A°)	c/a	Volume (A^{o3})
0.25	3.989	3.989	14.781	3.705	235.197
0.50	3.982	3.982	14.760	3.707	234.040
0.75	3.979	3.979	14.755	3.708	233.607

TABLE. 4.1: Lattice parameters a, b, c, c/a and volume as a function of Mn doping $(Cu_{0.5}Tl_{0.5})Ba_2(Ca_{2-y}Mn_y)Cu_3O_{10-\delta}$ Superconductors.

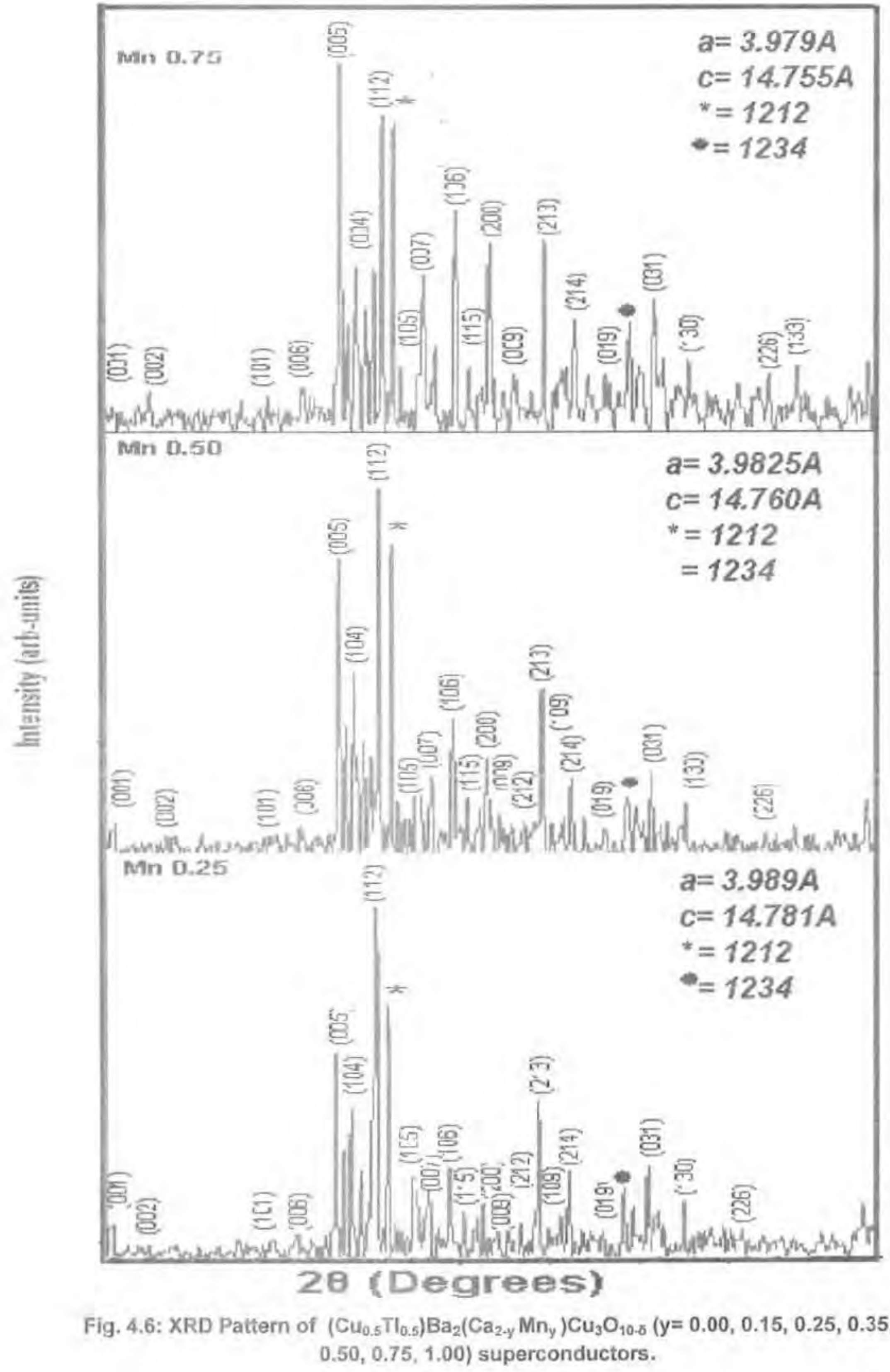

Fig. 4.6: XRD Pattern of $(Cu_{0.5}Tl_{0.5})Ba_2(Ca_{2-y}Mn_y)Cu_3O_{10-\delta}$ (y= 0.00, 0.15, 0.25, 0.35, 0.50, 0.75, 1.00) superconductors.

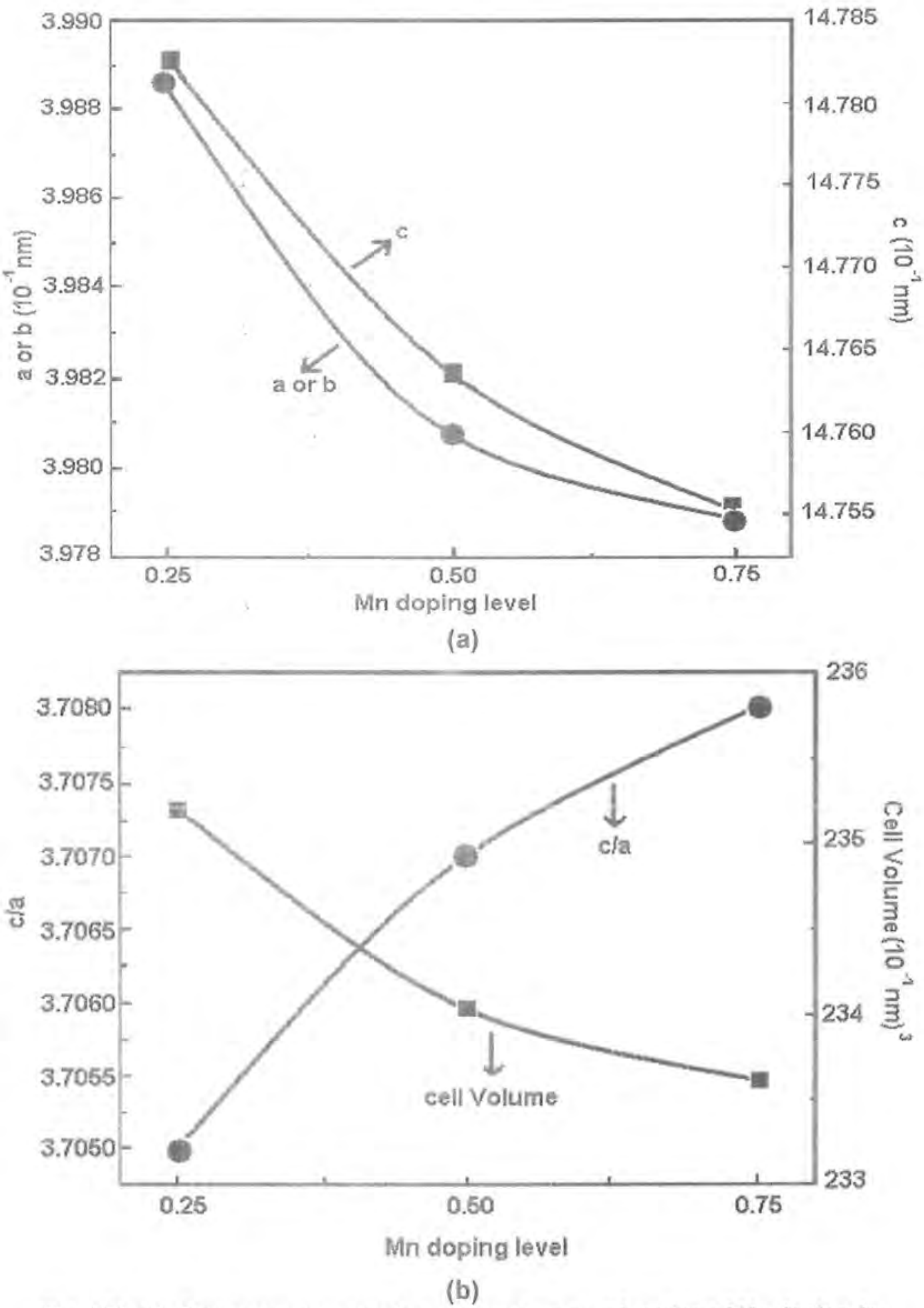

Fig. 4.7(a,b): Cell parameters a or b, c, c/a, volume as a function of Mn doping for $(Cu_{0.5}Tl_{0.5})Ba_2(Ca_{2-y}Mn_y)Cu_3O_{10-\delta}$ superconductors.

4.3 Oxygen Post-annealed $Cu_{0.5}Tl_{0.5}Ba_2(Ca_{2-y}Mn_y)Cu_3O_{10-\delta}$ (y=0, 0.15, 0.25, 0.35, 0.5, 0.75, 1.0) samples:

The resistivity measurements of oxygen post-annealed $Cu_{0.5}Tl_{0.5}Ba_2(Ca_{2-y}Mn_y)Cu_3O_{10-\delta}$ (y=0, 0.15, 0.25, 0.35, 0.5, 0.75 1.0) samples are shown in Fig. 4.8(a,b). These samples have shown metallic variation of resistivity from room temperature down to onset of superconductivity. The room temperature resistivity of these samples is not significantly influenced by the post-annealing in oxygen atmosphere and it varies from 0.04 to 0.15Ω-cm. The T_c(onset) and T_c(R=0) as a function of Mn-doping for the oxygen post-annealed samples are displayed in Fig. 4.9(a,b). Both the T_c(onset) and T_c(R=0) are suppressed after post-annealing in oxygen. Oxygen post-annealed $Cu_{0.5}Tl_{0.5}Ba_2(Ca_{2-y}Mn_y)Cu_3O_{10-\delta}$ samples have shown T_c(R=0) around 96.5, 95.5, 93.4, 94.4, 92.4, 92.4, 83.3K for Mn doping of y=0, 0.15, 0.25, 0.35, 0.5, 0.75, 1.0. The AC-susceptibility measurements of oxygen post annealed $Cu_{0.5}Tl_{0.5}Ba_2(Ca_{2-y}Mn_y)Cu_3O_{10-\delta}$ (y=0, 0.15, 0.25, 0.35, 0.5, 0.75, 1.0) samples are shown in Fig. 4.10(a,b). A small increase in the magnitude of diamagnetism is observed after optimization of the carriers accomplished via post-annealing in oxygen atmosphere. Mn-doping versus magnitude of diamagnetism at 77K is shown in Fig. 11. For Mn-doping of y=0.15, 025, 0.35, an increase in the magnitude of diamagnetism is observed which is most likely associated with increased carriers concentration in the conducting CuO_2 planes after the optimization of charge carriers which in turn decrease the density of anti-ferromagnetic aligned spins of Cu atoms in the conducting CuO_2 planes.

The phonon modes of $Cu_{0.5}Tl_{0.5}Ba_2(Ca_{2-y}Mn_y)Cu_3O_{10-\delta}$ (y=0, 0.15, 0.25, 0.35, 0.5, 0.75, 1.0) oxygen post-annealed samples observed by FTIR absorption measurements are shown in Fig. 4.12. The salient features of these absorption spectra are that Cu(1)-O_A-Cu(2) apical oxygen mode is soften (in comparison with as-prepared samples) with increased Mn doping. This mode after post-annealing in oxygen atmosphere is observed around 539, 537, 537, 536.5, 534.5, 533.5, 533cm^{-1}. The CuO_2 planar oxygen mode is also softened with increased Mn doping. For Mn doping of y=0, 0.15, 0.25, 0.35, 0.5, 0.75, 1.0 this mode is observed around 581, 579.5, 577.5, 576, 575, 575 and 573cm^{-1} respectively. The intensity of O_δ mode of oxygen atoms of $Cu_{0.5}Tl_{0.5}Ba_2O_{4-\delta}$ charge reservoir layer observed around 690cm^{-1} is increased after post-annealing in oxygen. The increased intensity of O_δ mode of oxygen atoms is manifestation of enhanced oxygen diffusion into the charge reservoir layers, which in turn optimizes the density of carries in the conducting planes and changes the dipole moment of O-Cu-O bonds. The planar oxygen modes which were hardening with increased Mn-doping in as-prepared samples, are observed to be softening with increased Mn doping in oxygen post-annealed samples. Such observations strengthen our belief that the charge state of the Mn is different from +2 and is most likely more than +2, which can localize the free carriers in conducting CuO_2 plane. Due to such possible localization of the carriers at the Mn sites anti-ferromagnetic alignment of copper spins is enhanced, which suppress the magnitude of superconductivity in the final compound. The softening of CuO_2 planar oxygen mode also tells that Mn is doped intrinsically in the final compound and influences strongly to the concentration of mobile carriers in the conducting CuO_2 planes.

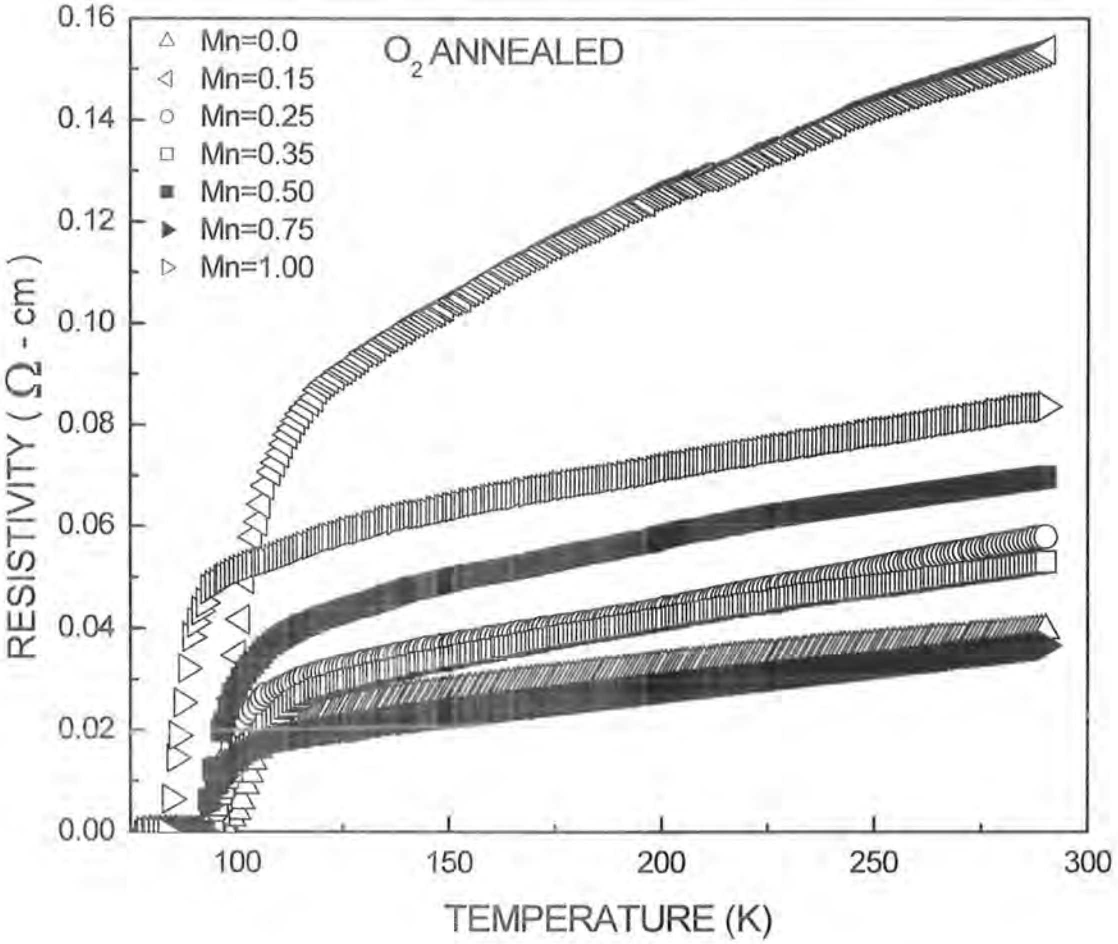

Fig. 4.8a: Resistivity curves of O_2 annealed $Cu_{0.5}Tl_{0.5})Ba_2(Ca_{2-y}Mn_y)Cu_3O_{10-\delta}$ (y=0.00, 0.15, 0.25, 0.35, 0.50, 0.75, 1.00) superconductors.

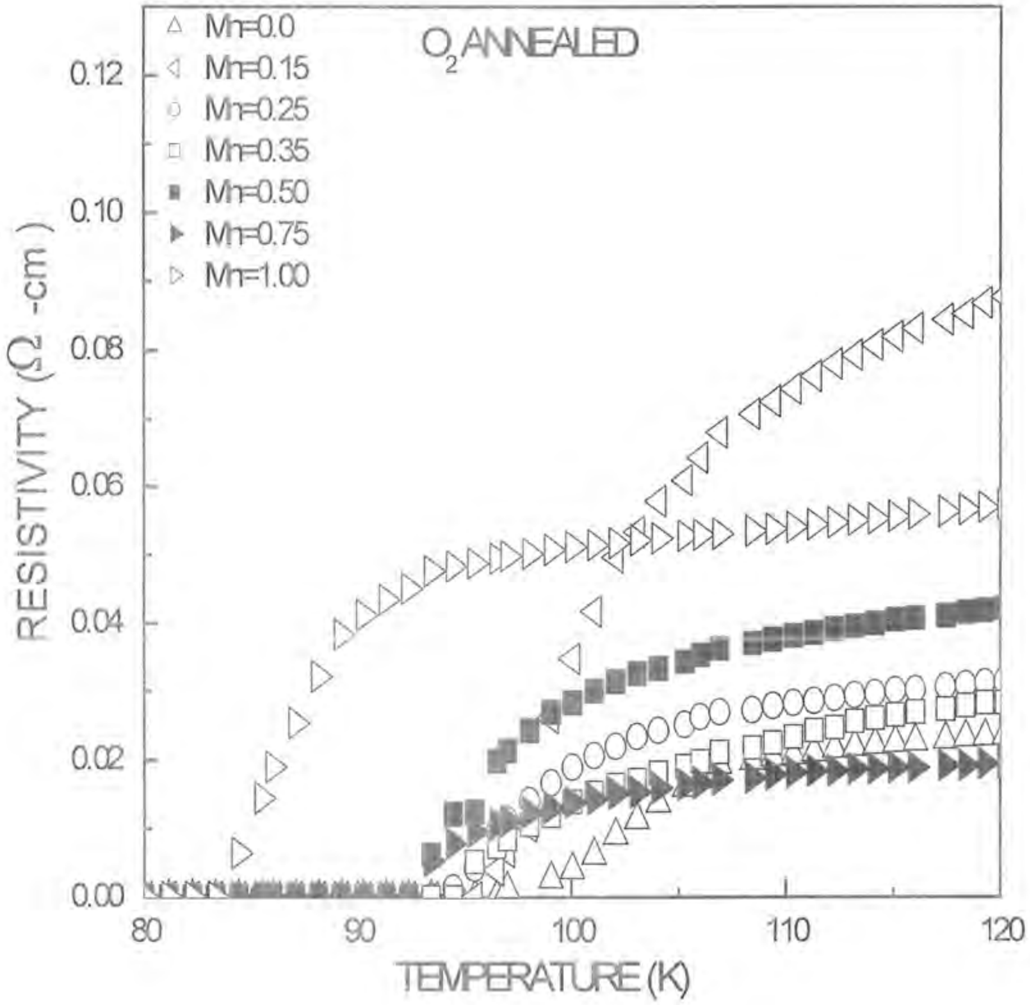

Fig. 4.8b: Transition region of resistivity of O_2 annealed $(Cu_{0.5}Tl_{0.5})Ba_2(Ca_{2-y}Mn_y)Cu_3O_{10-\delta}$ (y=0.00, 0.15, 0.25, 0.35, 0.50, 0.75, 1.00) superconductors.

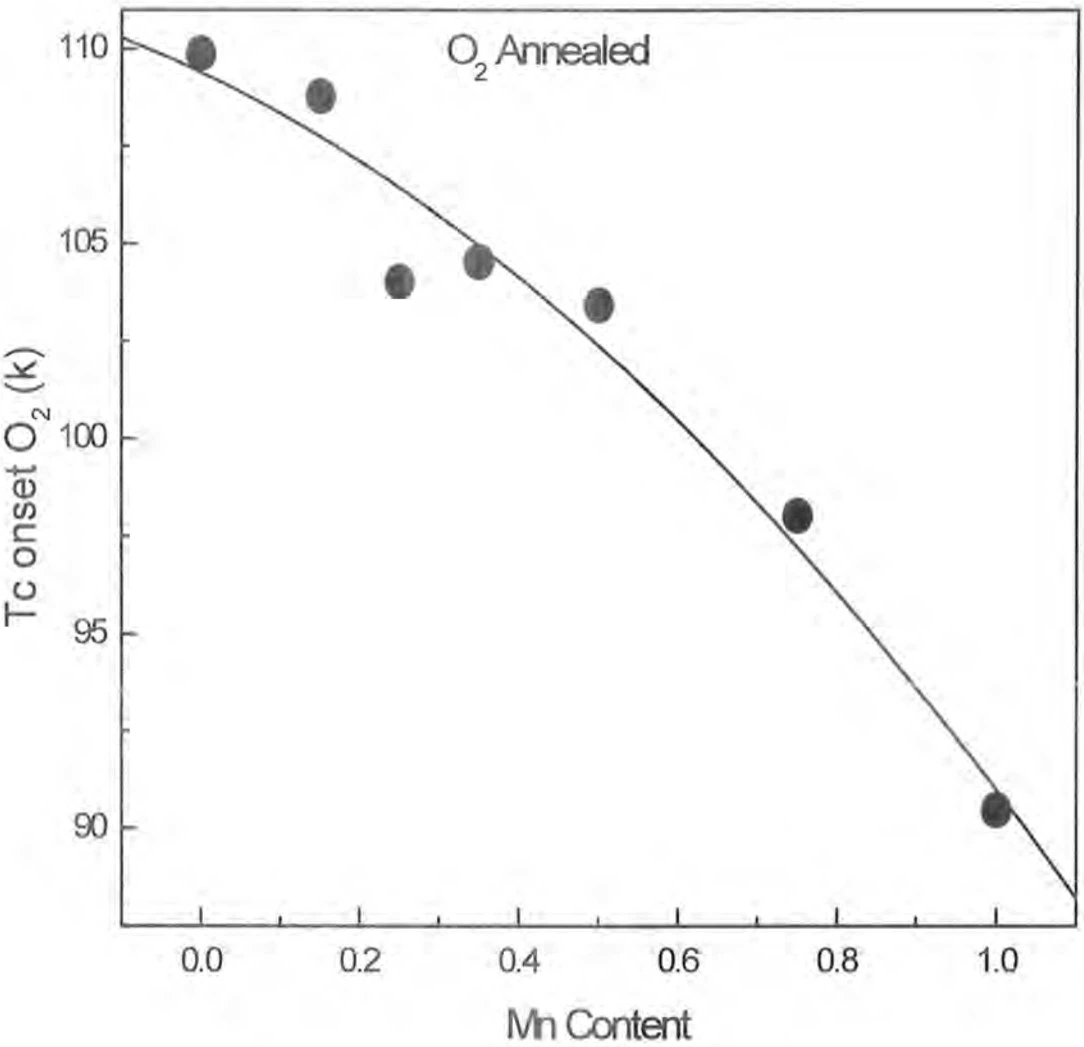

Fig. 4.9a: The transition onset temperature as a function of Mn-doping concentration for O_2 annealed $(Cu_{0.5}Tl_{0.5})Ba_2(Ca_{2-y}Mn_y)Cu_3O_{10-\delta}$ (y=0.00, 0.15, 0.25, 0.35, 0.50, 0.75, 1.00) superconductors.

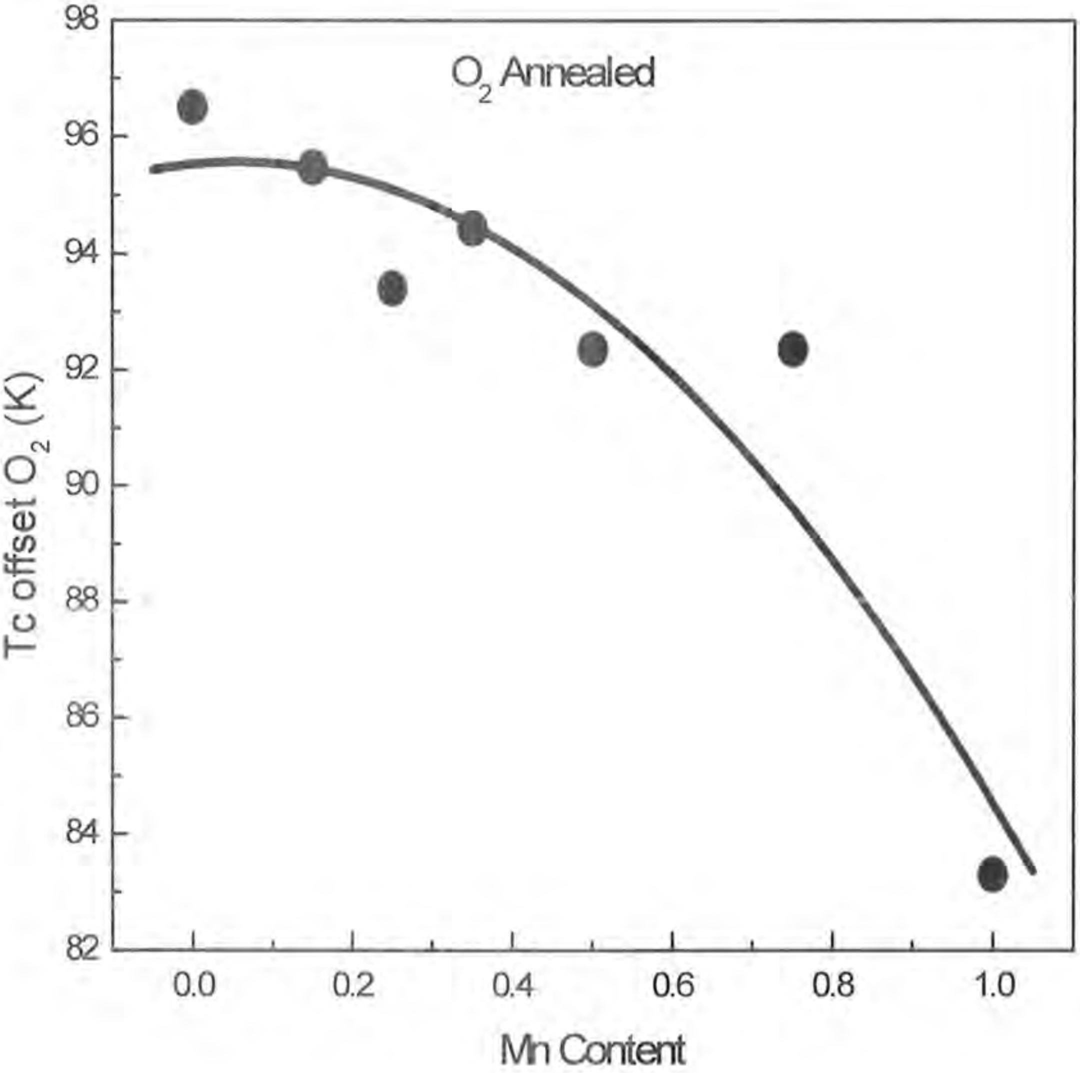

Fig. 4.9b: The zero resistivity critical temperature as a function of Mn doping concentration for O_2 annealed $(Cu_{0.5}Tl_{0.5})Ba_2(Ca_{2-y}Mn_y)Cu_3O_{10-\delta}$ y=0.00,0.15, 0.25,0.35, 0.50, 0.75, 1.00) Superconductors.

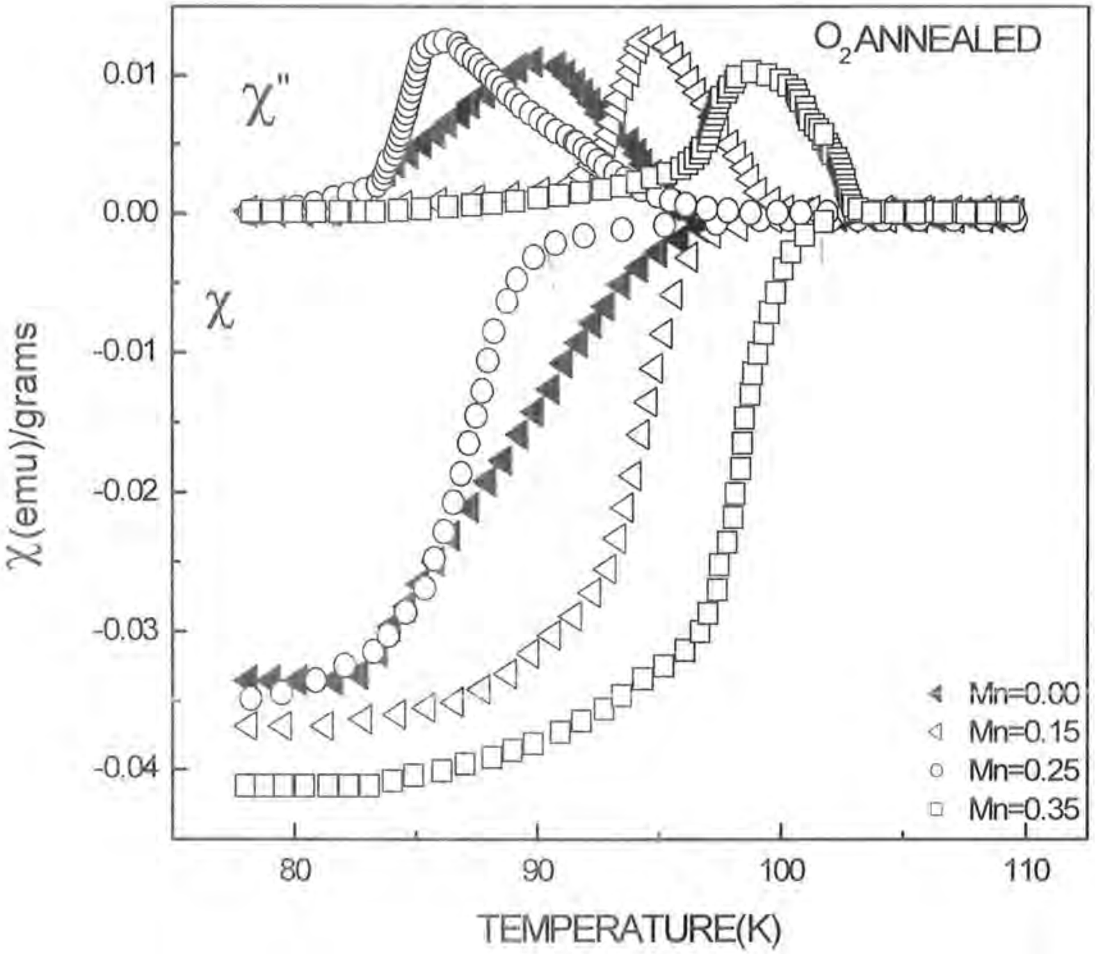

Fig. 4.10a: AC-susceptibility measurements of O_2 annealed $(Cu_{0.5}Tl_{0.5})Ba_2(Ca_{2-y}Mn_y)Cu_3O_{10-\delta}$ (y=0.00, 0.15, 0.25, 0.35) superconductors.

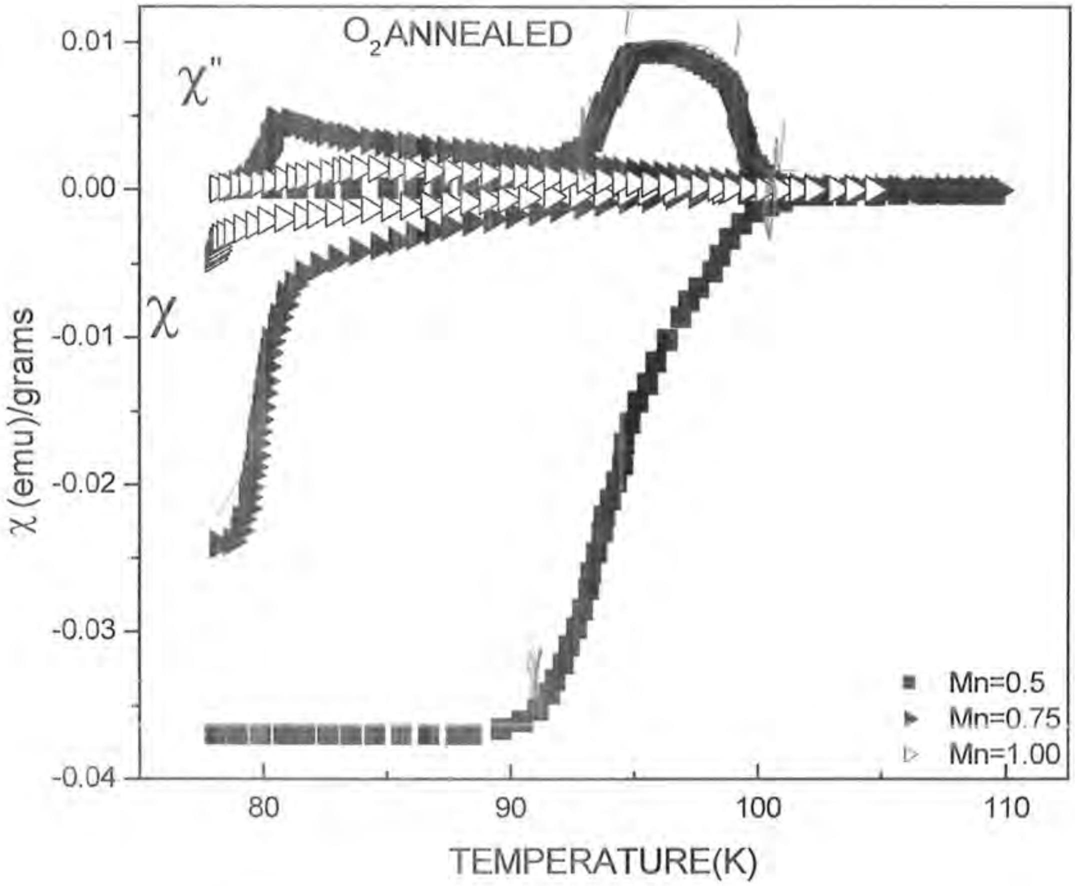

Fig. 4.10b: AC-susceptibility measurements of O_2 post annealed $(Cu_{0.5}Tl_{0.5})Ba_2(Ca_{2-y}Mn_y)Cu_3O_{10-\delta}$ (y= 0.50, 0.75, 1.00) superconductors.

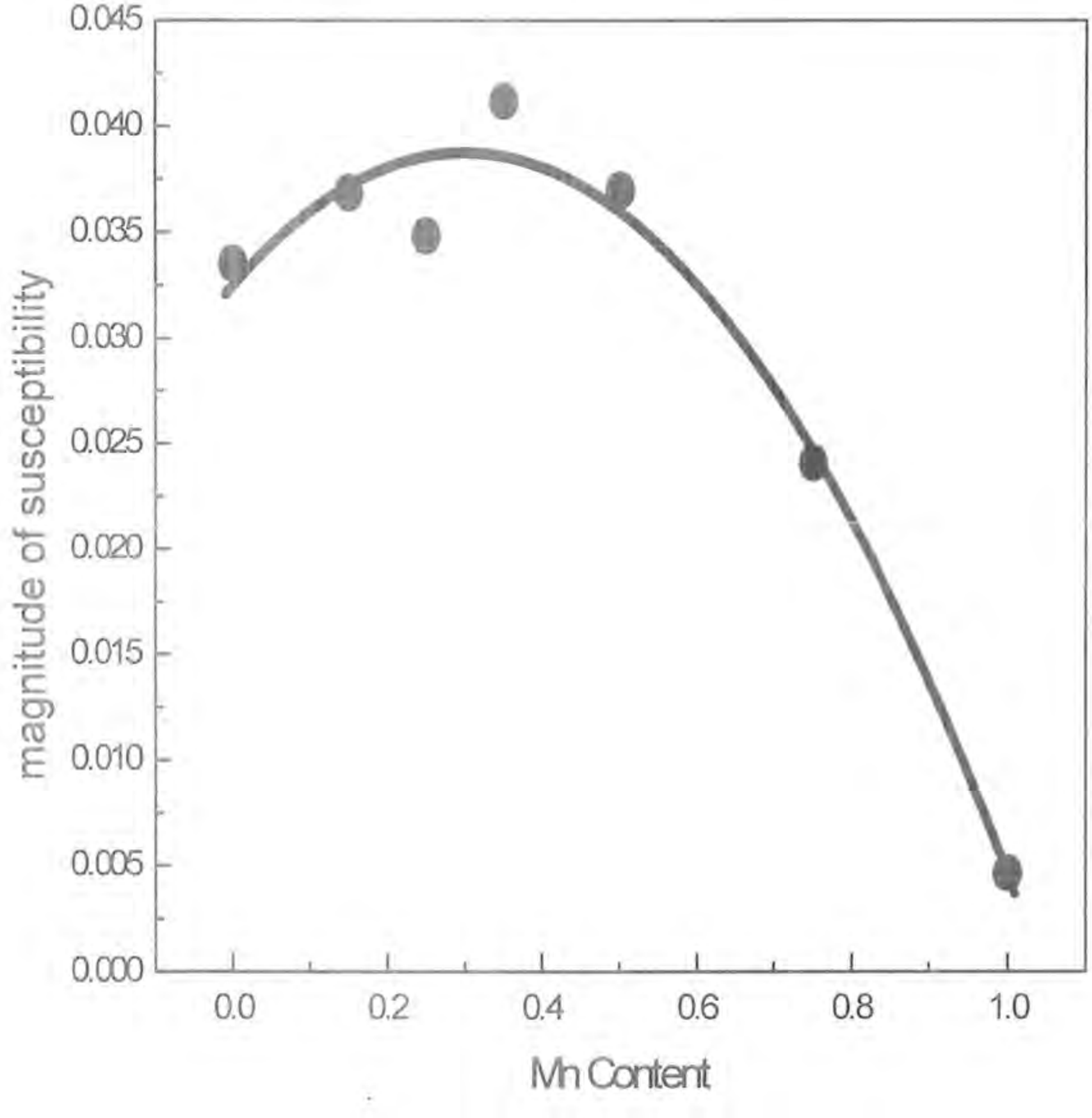

Fig. 4.11: Magnitude of susceptibility versus Mn doping concentration for $(Cu_{0.5}Tl_{0.5})Ba_2(Ca_{2-y}Mn_y)Cu_3O_{10-\delta}$ y=0.00, 0.15, 0.25,0.35, 0.50, 0.75, 1.00 superconductors.

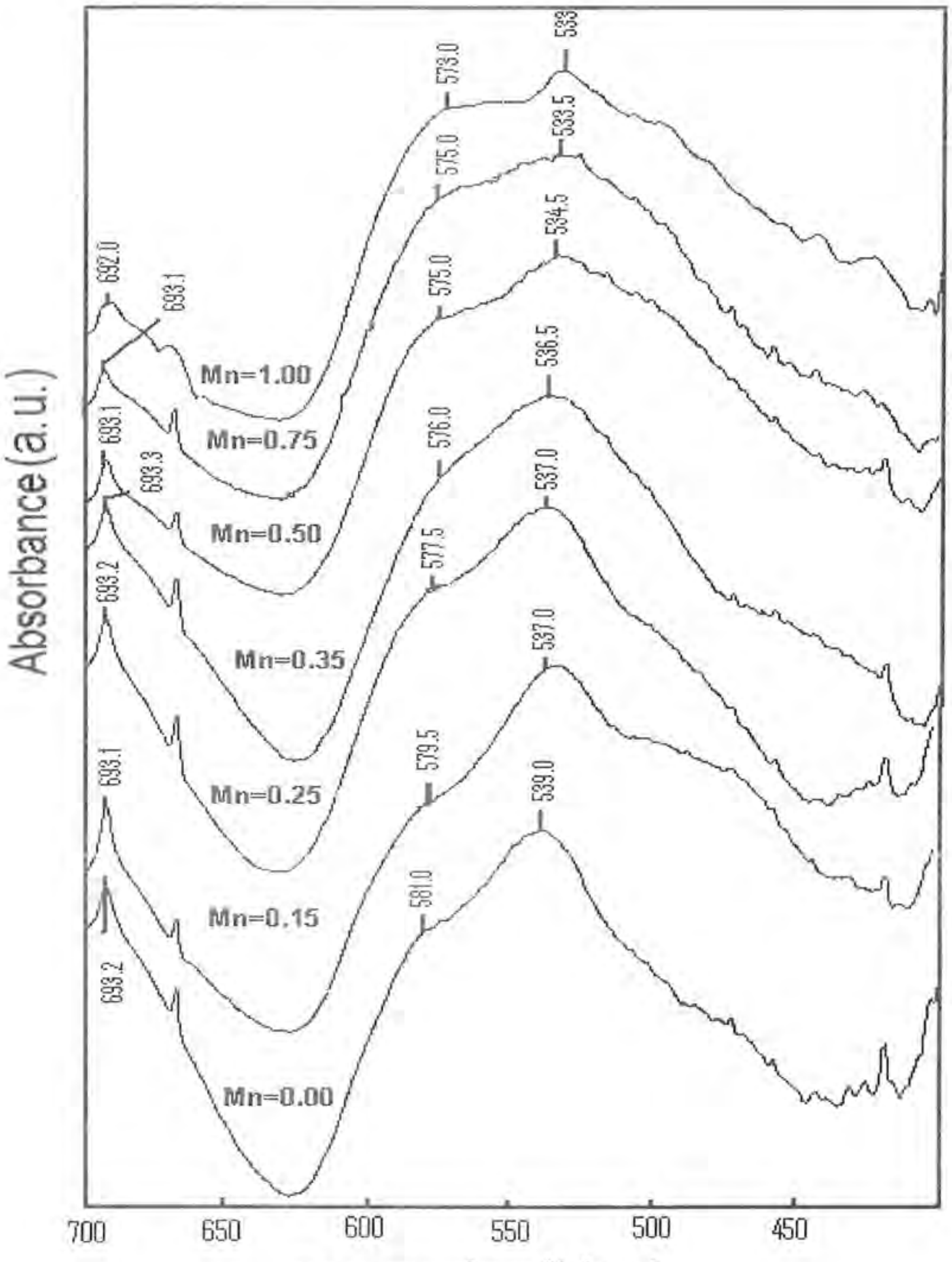

Fig. 4.12: Infrared absorption spectra of O_2 annealed $(Cu_{0.5}Tl_{0.5})Ba_2(Ca_{2-y}Mn_y)Cu_3O_{10-\delta}$ (y= 0.0, 0.15, 0.25, 0.35, 0.50, 0.75, 1.00) superconductors.

Conclusions

In conclusion we have successfully synthesized Mn-doped $Cu_{0.5}Tl_{0.5}Ba_2(Ca_{2-y}Mn_y)Cu_3O_{10-\delta}$ (y=0, 0.15, 0.25, 0.35, 0.5, 0.75 1.0) samples and studied their superconducting properties. The main object of substitution of Mn at the Ca site was to see the influence of multiple oxidation states (preferably >+2) on the density of mobile carriers and in turn their influence on the charge/spin state of neighbouring Cu atoms in the CuO_2 planes. These studies were important for understanding basic mechanism of high temperature superconductivity in the context of charge stripe model. According to this model interaction spin and charge density wave bring the superconductivity in these compounds. If the density of spins of Cu atoms is suppressed with the anti-ferromagnetic alignment of them, the interaction of spins density waves with the charge density of mobile carriers is suppressed resulting into decreased superconductivity. Our studies strongly support this thesis, as the volume fraction of the superconductivity is suppressed with increased Mn doping in the final compound. The $T_c(R=0)$ and magnitude of superconductivity are systematically suppressed with increased Mn-doping. It is most likely that the doping of Mn at the Ca site may promote a decrease in the density of mobile carriers due to possible localization of the carriers at the Mn sites due to its higher electro-negativity in comparison with Ca atoms. This possible decrease in the density of the mobile carriers in the CuO_2 plane would increase the anti-ferromagnetic alignment of the spins of Cu atoms which in turn suppresses the density of spin wave possibly interacting with the charge density waves and bringing about high temperature superconductivity. The hardening of CuO_2 planar oxygen mode and the softening of apical oxygen mode of Cu(2)-OA-Cu(1)with increased Mn-doping is an evidence of changed dipole moment there due to Mn-doping. The bonds associated with the higher carrier's concentration will be polarized more easily compare to the ones with lower carriers density. This conjecture becomes more evident in the case of post-annealed samples, because CuO_2 planar oxygen modes are softened with increased Mn-doping. The Cu(2)-OA-Cu(1)mode, however, shows softening behaviour after-post annealing in oxygen with increased Mn-doping, which convincingly confirm our belief that Mn alters the spin configuration of Cu atoms in the CuO_2 planes.

Reference:

1. H. Ihara, A. Iyo, K. Tanaka, K. Tokiwa, N. Terada, M. Tokumoto, K. Ishida and M. Umeda Advances in Superconductivity IX, Proceedings of the 9th international symposium on superconductivity, October 21-24, 1996, Sapporo, Tokyo, Japan (Springer-Verlag Tokyo 1997)
2. H. Ihara, A. Iyo, K. Tanaka, K. Ishida, N. Terada, M. Tokumoto, Y. Sekita, T. Tsukamoto, T. Watanabe and M. Umeda Physica C 282-287 (1997) 1973-1974
3. A. Iyo, K. Tokiwa, T. Kanehira, H. Ozawa, N. Kobayashi, N. Terada, M. Tokumoto, M. Hirabayashi, H. Ihara Advances in Superconductivity IX, Proceedings of the 9th international symposium on superconductivity (ISS'94), November 8-11, 1994, Kitakyushu (Springer-Verlag Tokyo 1995)
4. N. Hamada and H. Ihara Physica B 284-288, 1073 (2000)
5. N. Hamada and H. Ihara Physica C 357-360 (2001) 108-111
6. H. Ihara, A. Iyo, K. Tanaka, K. Tokiwa, N. Terada, M. Tokumoto and M. Umeda Advances in Superconductivity VIII, Proceedings of the 8th international symposium on superconductivity, October 30-November 2, 1995, Hamamatsu, Japan (Springer-Verlag Tokyo 1996)
7. M. Jergel, A. C. Gallardo, C. F. Guajardo and V. Strbik Institute of Electrical Engineering, Slovak Academy of sciences, 84239 Brastislava, Slovak republic supercond. Sci. Technol.9 (1996) 427-446
8. H. kotegawa, Y. Tokunaga, K. Ishida, G.-q. Zheng, Y. Kitaoka, K. Asayama, H. Kito, A. Iyo, H. Ihara, K. Tanaka, K. Tokiwa, T. Watanabe journal of physics and chemistry of solids 62 (2001) 171-175
9. H. Ihara, A. Iyo, K. Tanaka, K. Tokiwa, K. Ishida, N. Terada, M. Tokumoto,. Y. Sekita, T. Tsukamoto, T. Watanabe and M. Umeda Physica C 282-287 (1997) 1973-1974
10. H. Ihara, K. Tanaka, Y. Tanaka, A. Iyo, N. Terada, M. Tokumoto, F. Tateai, M. Kawamura, K. Ishida, S. Miyashita, T. Watanabe Physica B 284-288 (2000) 1085-1086
11. H. Ihara Advances in Superconductivity VII, Proceedings of the 7th international symposium on superconductivity (ISS'94), November 8-11, 1994, Kitakyushu, Japan (Springer-Verlag Tokyo 1995)